Centro de Investigación Científica y de Educación Superior de Ensenada, Baja California

Maestría en Ciencias
en Óptica con orientación en Optoelectrónica

Fiber core position evaluation by 2D mapping of light intensity distribution

Tesis
para cubrir parcialmente los requisitos necesarios para obtener el grado de
Maestro en Ciencias

Presenta:

Marino Alberto Lara Alva

Ensenada, Baja California, México
2021

Tesis defendida por

Marino Alberto Lara Alva

y aprobada por el siguiente Comité

Dr. Serguei Miridonov Elakov
Director de tesis

Miembros del comité

Dr. Douglas Butler

Dr. Francisco Antonio Domínguez Serna

Dr. Israel Marck Martínez Pérez

Dr. Mikhail Shlyagin

Dr. Serguei Stepanov

Dr. Israel Rocha Mendoza
Coordinador del Posgrado en Óptica

Dr. Pedro Negrete Regagnon
Director de Estudios de Posgrado

Resumen de la tesis que presenta **Marino Alberto Lara Alva** como requisito parcial para la obtención del grado de Maestro en Ciencias en nombre del posgrado con orientación en Optoelectrónica.

Evaluación de la posición del núcleo de la fibra mediante mapeo 2D de la distribución de intensidad de luz

Resumen aprobado por:

____

Dr. Serguei Miridonov Elakov

Director de tesis

En este trabajo se presenta una metodología, para la evaluación de la posición del núcleo de una fibra, la cual hace uso de un sistema de medición, y además se comprueba que este sistema posee una precisión de entre 50 y 100 nm. Esta metodología consiste en utilizar el sistema de medición para mapear la distribución de intensidad de luz que sale de la fibra a medir. El sistema está conformado por una fibra que es usada como sonda y que está colocada sobre un posicionador controlado por computadora con movilidad 2D. Después de realizar el mapeo de la distribución de intensidad de luz se calculan los parámetros para que una Gaussiana se ajuste sobre la distribución de intensidad de luz. Esto debe realizarse para dos posiciones diferentes para estimar la posición del núcleo de la fibra, ya que se utiliza una expresión matemática, que se desarrolla en este trabajo, que depende de los parámetros calculados. Posteriormente, se estudió de forma teórica y experimentalmente la influencia del ruido en los fotodetectores y las imperfecciones de los componentes mecánicos en los errores del sistema de medición. Los resultados experimentales mostraron concordancia con el análisis teórico y este estudio sirvió para optimizar la geometría de los escaneos para obtener la mejor precisión para la configuración que se utilizó.

Palabras clave: Sistema de medición por fibra óptica; Medición de la posición del núcleo de una fibra óptica; Distribución Gaussiana.

Abstract of the thesis presented **by Marino Alberto Lara Alva** as a partial requirement to obtain the Master of Science degree in Optics with orientation in Optoelectronics.

Fiber core position evaluation by 2D mapping of light intensity distribution

Abstract approved by:

____

Dr. Serguei Miridonov Elakov

Thesis Director

This work presents a methodology to evaluate the fiber core position by using a custom made measuring system; furthermore it is proved that the measuring system has accuracy between 50 and 100 nm. The methodology consists on using the measuring system to do a 2D mapping of the light intensity distribution from the light coming out of a sample fiber. The measuring system is composed of a probing fiber that is installed on a 2D translation stage that is controlled by a computer. This procedure is done in two different positions along the optical axis of the sample fiber. Then the light intensity distributions on both positions are approximated by a Gaussian function whose parameters are used to estimate the position of the fiber core. This is possible thanks to a mathematical expression that is derived in this work, which is a function of the Gaussian parameters of the two positions. The influence of the measurement errors from the photodetectors' noise and imperfections of the mechanical components were studied both theoretically and experimentally. The experimental results are in good agreement with the findings of the theoretical analysis. This study allowed to find the optimal scan geometry to obtain the best possible accuracy for current experimental configuration.

Keywords: Fiber-optics measurement systems; Fiber core position measurement; Gaussian distribution.

Dedication

A mi padre, a mi madre y a toda la gente que me acompañó durante mi estancia en Ensenada

Acknowledgements

Le agradezco al Centro de Investigación Científica y de Educación Superior de Ensenada (CICESE) por la gran oportunidad de permitirme realizar mis estudios de maestría en sus instalaciones; al Consejo Nacional de Ciencia y Tecnología (CONACYT) por brindarme un apoyo financiero mediante la beca 913225. Sin este apoyo no habría podido seguir adelante en mi desarrollo académico.

Me gustaría expresar especial gratitud a mi director de tesis Dr. Serguei Miridonov por su apoyo y paciencia durante el trayecto del proyecto de tesis, así como a mis sinodales de tesis Dr. Douglas Butler, Dr. Mikhail Shlyagin, Dr. Serguei Stepanov, Dr. Francisco Domínguez y al Dr. Israel Martínez, por apoyarme con sus consejos y comentarios durante los avances y la revisión de la tesis. Me gustaría agradecer en especial al Dr. Mikhail Shlyagin por dejarme utilizar su laboratorio y al Dr. Vassili Spirine por dejarme utilizar su SLED. También un agradecimiento al Dr. Eliseo Hernández por su apoyo durante mi estancia en el laboratorio.

Quiero expresar un profundo agradecimiento a mi familia que estuvieron siempre apoyándome y sin ellos no habría llegado hasta aquí. Muchas gracias a mi padre Marino Gerardo Lara Hernández y a mi madre Nora Helena Alva Argáez, pues ellos siempre estuvieron presentes todo el tiempo durante mis estudios de maestría. A mis abuelos, por siempre estar pendientes de mí a pesar de las grandes distancias. A mi hermano Arturo por esas veces que me marcaba para platicar.

Muchas gracias a toda la gente de CICESE, incluyendo a mis profesores y compañeros de clase. Gracias a los profesores aprendí muchas cosas y tuve un gran desarrollo en el área de la óptica. Gracias a mis compañeros pude disfrutar mis estudios de maestría pues con ellos la pasaba muy bien y nos apoyábamos entre todos. Especialmente a mis mejores compañeros German y Carolina, pues con ellos superé múltiples retos en las distintas materias que llevamos.

Me gustaría también agradecer a la gente de Corning y las personas de CICESE que participaron en la creación del acuerdo CICESE-Corning. Sobre todo, me gustaría agradecer a Kevin Sparks, Luis Zenteno, Costas Saravanos y mi sinodal Dr. Douglas.

Finalmente me gustaría agradecer a una familia Chanes que siempre me recibió con los brazos abiertos y por supuesto al tío Che por presentármelos. Especialmente me gustaría agradecer a Mónica Chanes y a Juan Antonio Fernández, por todas esas veces que me invitaron a comer a su casa y me ayudaron con múltiples problemas que tuve. Gracias a ellos sentí que mi familia estaba todavía cerca.

Table of content

Figure list

Chapter 1. Introduction

1.1 Introduction

Today fiber optics plays a significant role in communication, industry, civil engineering, and information technology (Idachaba et al., 2014; Culshaw, 2000). Started from rapidly evolving applications as fast telecommunication lines in the last century (Montgomery et al. 2002), optical fibers nowadays are also used as multipurpose embedded sensors in the aircraft industry (Qing, et al., 2019), building, and bridges construction for structural monitoring (Casas et al., 2003), among others. The low light losses, high multiplexing capabilities that enable to connect hundreds or thousands of sensors into the whole sensing network allow for designing and building flexible advanced monitoring systems that permit to essentially reduce the risk of failures in large engineering structures.

The creation of new devices that use photons is of great interest since photons can do many things better than electrons; for example, light beams have a vast bandwidth, low transmission losses (compared with copper cables), do not dissipate heat, are faster and are immune to cross-talk and electromagnetic interference (Suhir, 2000). Despite the advantages that photons give, there is still a long way to create fully photonic devices; this is why microelectronics is still needed. Optoelectronic devices are of great interest since they are the combination of light and electrons, which gives the possibility of creating devices that process information faster and more efficiently in energy consumption than with purely electronic devices (Suhir, 2000).

An increasing demand for higher bandwidth density, even in the range of optical frequencies leads to the necessity of using the multi-fiber communication cables and multicore fibers (Harsted et al., 2012). Besides the long-distance and intercontinental telecommunications, optical fibers are also an attractive solution for information exchange on a much smaller scale. In data processing centers and supercomputers, it is sought to send a vast amount of information that requires interconnections of many processor units at giga- and terabit speeds, which is why there is great interest in fiber-to-chip connections, multi-fiber connectors, multicore fibers, and how to couple light into them. The multi-fiber connectors and multicore fibers give the possibility to send more information. The combination of chips (optoelectronic or photonic chips) with multi-fiber connectors or multicore fibers allowed to transmit information at high speed. However, for these to work properly, it is necessary that light coupling is carried out efficiently.The future advanced technology may require direct connection of multi-fiber or multicore communication buses with data processing chips to reduce delay and make the information processing or computing even faster (He et al., 2019).

The development and production of high-density interconnection devices using optical fibers, in turn, requires special high-precision systems for quality control and failure detection. The reason for that is a significant light loss in the fiber-fiber or fiber-chip interconnections when even a small offset appears between the centers of the sending and receiving fiber cores or between the fiber core and the optoelectronic device. In other words, the light coupling between the fibers and/or on-chip optoelectronic devices strictly depends on the relative positions of fibers and the devices themselves. To maximize the light coupling between these optical components and reduce the light losses, the fiber-optic production systems need to implement measuring technology that permits to estimate fiber cores' position in the produced connectors. Statistical and quantitative analysis of the measuring system is needed to implement a system that measures the fiber core position. In addition to the core position, parameters such as noise limitation, system stability, error measure, and repeatability must be evaluated.

Systems capable of measuring the core position already exist. Even though they follow a different methodology, a common feature they share is the use of the light coming out of the fiber to do the measurement. Some of these systems will be described in Chapter 3.

In this work, a method to measure the fiber core position is developed. The method consists of a scan that follows a specific geometry. The scan is made along the optical axis of the fiber to measure the light intensity distribution that comes out of it and then a Gaussian function is fit with the obtained data to calculate the core position. Figure 1 represents this process with a scan using equidistant points within a square (mesh-like scan).

To obtain the position of the fiber core, the measurement is done in two different positions along the emitting fiber optical axis. Once this is made for both positions, it is possible to calculate the fiber core position with a mathematical expression for the fiber core position as a function of all the calculated parameters. This will be board in Chapter 4.

This work will focus on the position of the fiber core since it is an essential parameter that determines the efficient light coupling in the fiber-optic interconnections.

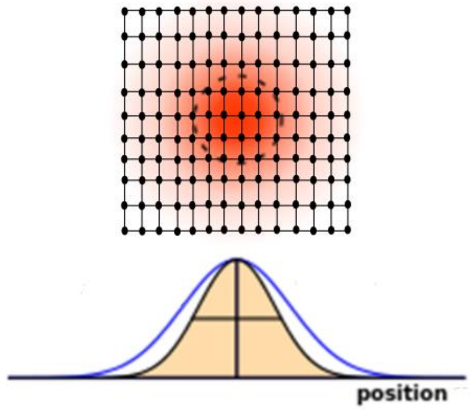

Figure 1. Representation of the scan with equidistant points within a square over Gaussian light distribution (FDominec, 2007).

1.2 Objectives

This work general objective is to implement a system that estimates the core position of 1550 nm single-mode fibers by making measurements of light intensity in the far-field with another single-mode fiber mounted on a computer-programmed XY stage. The arrangement will be presented in chapter 5.

As specific objectives, it is sought to develop software algorithms to control an XY translation stage and to acquire measurement data, assemble an experimental setup that will estimate the nucleus position of a single-mode fiber, with an accuracy below 100 nm, find the minimum amount of samples for the required accuracy and to provide a theoretical analysis for the accuracy of the system.

1.3 Structure of the thesis

The thesis is divided in seven chapters including the introduction. After the introduction the next part is Chapter 2, which includes the necessary background and theory to understand the work. Chapter 3 is about the state of the art, here it is exposed why a system capable of measuring the fiber core position is useful and then some available measuring methods are shown. Chapter 4 introduces the theoretical research that was realized, including the physical and mathematical models that were used to analyze the data from the light mapping. Chapter 5 presents the experimental setup that was used for the measurements and the method used to estimate the fiber core position. Chapter 6 is where the results are shown and discussed and finally in Chapter 7 the conclusions with some recommendations are given. At the end of this manuscript there is an Appendix for more details regarding the construction of the experimental setup.

Chapter 2. Background and theory

This chapter introduces some theoretical concepts, such as light propagation in step-index fibers, approximation of the intensity distribution by Gaussian function, and measurement and error theory. These concepts will be necessary to understand the theoretical basis of this work in chapter 4 and the results presented in chapter 6.

2.1 Light distribution from a step-index fiber

According to Saleh and Teich (Salehh and Teich, 1991) a step-index fiber is a cylindrical dielectric waveguide specified by its core and cladding refractive indices, n_1 and n_2 respectively. An important aspect of these types of fibers is that the refractive indices must differ slightly in order to have a fractional refractive-index change $\Delta \ll 1$ which is defined as

$$\Delta = \frac{n_1 - n_2}{n_1}, \tag{1}$$

where $n_1 > n_2$ so Δ is always positive. This condition is necessary to decrease the number of modes inside the fiber, decreasing the modal dispersion.

Another essential requirement, of why the core refractive index must be greater than the cladding refractive index, is to provide total internal reflection. Figure 2 shows the types of rays that can be found in multimode and single-mode step-index fibers.

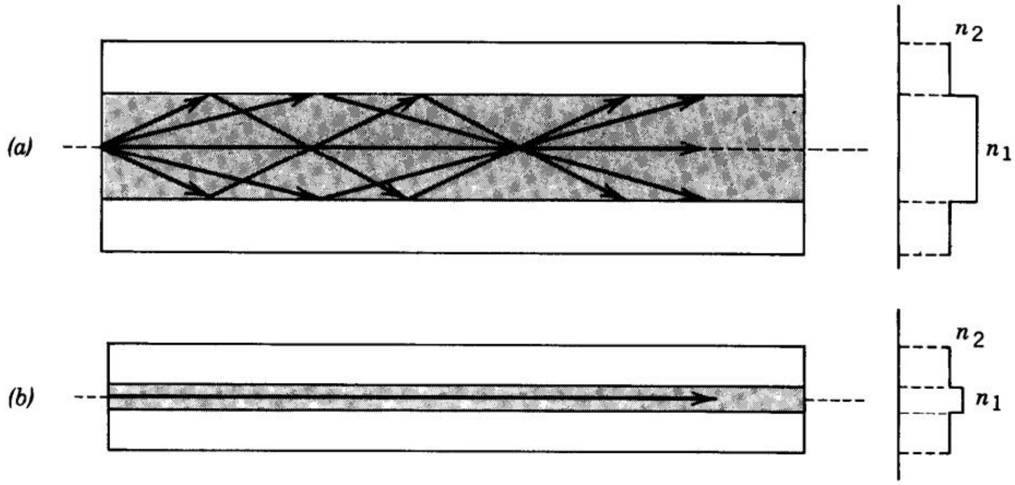

Figure 2. Typical rays in (a) multimode and (b) single-mode step-index fiber (Saleh and Teich, 1991).

Since the refractive index control is essential, many of the fibers used in optical communication systems are made of fused silica glass (SiO_2) of high chemical purity (Saleh and Teich, 1991). Changes in the refractive index are achieved by adding doping materials at low concentration, for example, titanium, germanium, or boron.

2.1.1 Exact equation for far-field intensity distribution

The development of the system for measurement of the fiber core position using the light emitted by the fiber requires an understanding of the mathematical expression that describes the emitted light spatial distribution. This is necessary to design an algorithm that will calculate the position of the light intensity distribution centroid.

To obtain an Equation for the emitted light in the far field, it is necessary, firstly, to have an expression of how light behaves inside the fiber. Two Helmholtz Equations in cylindrical coordinates must be solved to obtain the electric field of light inside a step-index fiber. One is used to describe the light inside the core (Saleh and Teich, 1991)

$$\frac{d^2u}{dr^2} + \frac{1}{r}\frac{du}{dr} + \left(k_T^2 - \frac{l^2}{r^2}\right)u = 0, \quad r < \alpha \tag{2}$$

where ***u(r)*** is the electric field of light, *r* is the radial coordinate, ***l*** is a constant related to harmonic waves, and α is the radius of the core, and k_T is defined as

$$k_T{}^2 = n_1{}^2 k_0{}^2 - \beta^2, \tag{3}$$

where n_1 is the core refractive index, k_o is the wavenumber in vacuum, and *β* is the propagation constant. Another Equation describes the light in the cladding (Saleh and Teich, 1991)

$$\frac{d^2u}{dr^2} + \frac{1}{r}\frac{du}{dr} + \left(\gamma^2 - \frac{l^2}{r^2}\right)u = 0, \quad r > \alpha \tag{4}$$

where γ is defined as

$$\gamma^2 = \beta^2 - n_2{}^2 k_0{}^2, \tag{5}$$

where n_2 is the refractive index of the cladding. The solutions for these differential Equations are proportional to Bessel functions and modified Bessel functions. Each Bessel function corresponds to a certain light mode.

$$u(r) \propto \begin{cases} J_l(k_T r), \ r < \alpha \\ K_l(\gamma r), \ r > \alpha \,. \end{cases} \tag{6}$$

In this work, single-mode fiber is considered; thus, only the fundamental mode expression will be used. The principal mode inside the core is defined as

$$\Psi_{core}(r) = J_0(k_T r), \tag{7}$$

where $r < a$. At the cladding is defined as

$$\Psi_{cladding}(r) = \frac{J_0(ak_T)}{K_0(a\gamma)} K_0(\gamma r), \tag{8}$$

where $r > a$.

Since the emitted light intensity profile measurements will be done in free space, far from the fiber tip, it is vital to consider the so-called far-field intensity distribution. The light that comes out of the fiber can be described by the Rayleigh-Sommerfield diffraction scalar Equation and the far-field approximation (Li and Guo, 2010)

$$\Psi(P) = \frac{1}{2\pi} \iint_{\Sigma} \Psi(P_o) \left(\frac{1}{L} - ik\right) \cos(\vec{n}, L) \frac{\exp(ikL)}{L} ds, \tag{9}$$

where $\Psi(P_o)$ is the initial field, P_o is the initial position where the electric field propagates, P is the position where the function is evaluated, L is the distance between P_o and P, k is the wavenumber, $\cos(\vec{n}, L)$ represents the cosine of the angle between an outward normal vector $\vec{n}$ and the line segment $\overline{P_o P}$ and the integral is made over a surface Σ.

By using the solution for (7) or (8) for the initial field in (9), it is possible to obtain the light distribution that comes out of a step-index fiber.

2.1.2 Gaussian approximation

Evaluation of the integral in Equation (9) with Bessel functions is computationally demanding; therefore, certain conditions must be taken into account to find good approximations, which can be calculated much faster. A more feasible path to achieve this goal is the use of a Gaussian function. Li and Guo (Li and Guo, 2010) showed that Equation (9) resembles a Gaussian field when a far-field approximation is considered; thus, it is possible to do calculations with a Gaussian function instead of Equation (9). Li and Guo obtained this result the following way: first, the fiber is assumed to be single-mode; this way, other modes contribution will not be considered. Then it is assumed that the distance z between the fiber and the detector fulfills the following condition

$$z^2 \gg 2\frac{r^2}{\lambda}, \tag{10}$$

where r is the radius of the fiber and λ is the wavelength of the light that comes out of the fiber. Using this approximation, Equation (9) can be expressed as

$$\Psi(P) = \frac{cos^2(\alpha)\exp(ikzsec(\alpha))}{i\lambda z}\int_0^{2\pi}\int_0^{\infty}\Psi(P_o)\exp(-ikrsin(\alpha)\cos(\varphi))rdrd\varphi. \quad (11)$$

Here α is the half-angle between the optical axis and the line segment that goes from the center of the fiber to the position in the plane where the function is being evaluated. When the Equation (11) is evaluated only for the LP_{01} mode, after the normalization, it can be seen, that the resulting field fits closely enough with a Gaussian function as shown in Figure 3.

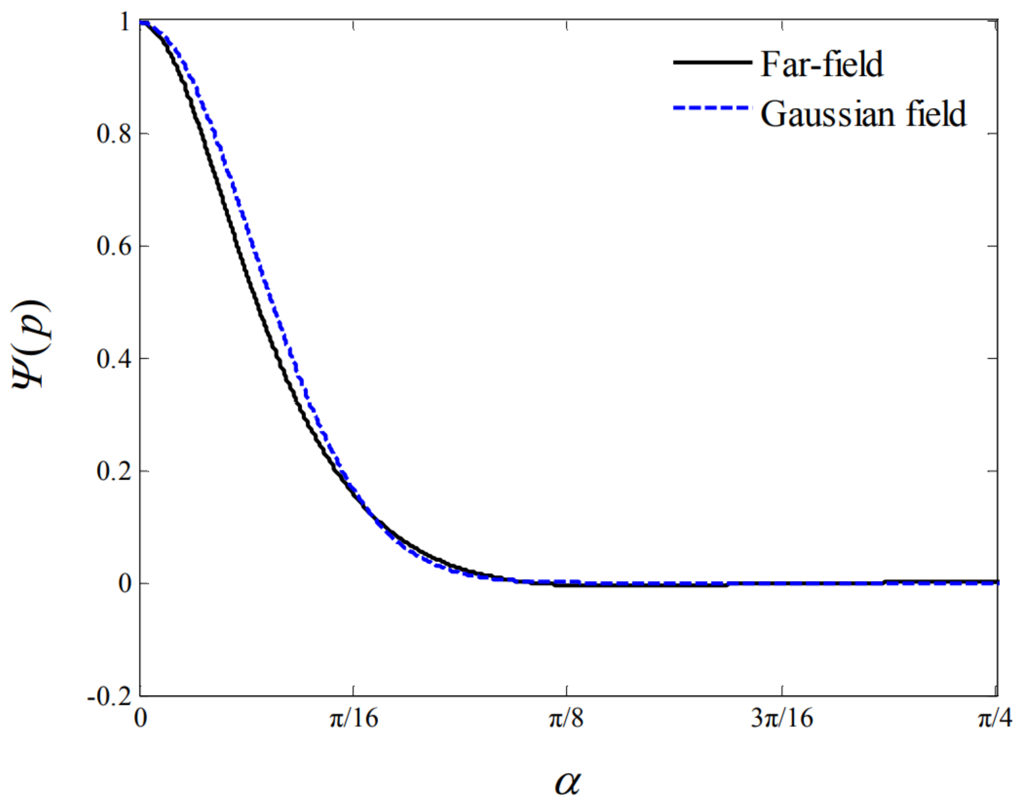

Figure 3. The normalized amplitude distribution of diffraction far-field (Li and Guo, 2010).

This result will be useful for this work since working with Gaussian function is less demanding than with Bessel functions.

2.1.3 Parameters of a Gaussian intensity distribution

Since the light coming out of a step-index fiber can be approximated with a Gaussian function, it is important to introduce the basics of light with Gaussian distribution.

A fundamental Gaussian light beam mode is a solution for the paraxial Helmholtz Equation and is commonly used to describe mathematically the light from a laser operating at the fundamental mode. The expression for the electric or magnetic field amplitude of the optical wave in the Gaussian beam is (Saleh and Teich, 1991)

$$U(x,y,z) = A_o \left[\frac{W_o}{W(z)}\right] \exp(-\frac{x^2+y^2}{W^2(z)}) \exp(-ikz - ik\frac{x^2+y^2}{2R(z)} + i\xi(z)), \tag{12}$$

where A_o is the amplitude, $W(z)$ is the cross-section radius given a position z, W_o is the waist radius, k is the wavenumber, $\xi(z)$ is a phase term, and $R(z)$ is the wave front curvature radius at a given z position. With this Equation, the intensity can be obtained

$$I(x,y,z) = I_o \left[\frac{W_o}{W(z)}\right]^2 \mathrm{e}^{-\frac{2(x^2+y^2)}{W^2(z)}}, \tag{13}$$

where $I_o = {A_o}^2$. As can be seen, the Gaussian beam main intensity distribution parameters are the amplitude I_o, which represents here the maximum intensity, and the beam radius W(z), which varies with the distance.

The Equation (13) is valid only when the Gaussian beam is centered and aligned along the z-axis. Since the fiber location that must be found from the intensity distribution measurements, in general, might be arbitrary, and the fiber axis might not be aligned along the z-axis, the latter Equation should be transformed into a more general form:

$$I(x,y,z) = I_o \left[\frac{W_o}{W(z)}\right]^2 \mathrm{e}^{-\frac{2\left[(x-x_0)^2+(y-y_0)^2\right]}{W^2(z)}}, \tag{14}$$

where x_0 and y_0 are the coordinates of the center of the light distribution. These coordinates become additional parameters of the Gaussian function that have to be defined from the intensity measurements together with the mentioned above amplitude, I_0 and the beam radius W.

This expression is of great importance for this work since it will be used to analyze the light coming out of the optical fiber.

2.2 Localization of the fiber core position

In this work, it is required to find the parameters of Gaussian light distribution from the experimentally measured distribution of the light intensity emitted by the fiber, and finally to find the position of the fiber core. As was mentioned above, the parameters, of the Gaussian function, are the center of the distribution, the amplitude, and its width. These parameters can be obtained by fitting a Gaussian function, using the least-squares method (LSM), to the experimentally obtained intensity data mapped over a 2D plane.

The following sections will explain how the intensity data mapping is made, how the least-squares method works, and there will be a brief explanation of how the 3D position of the fiber core will be obtained.

2.2.1 Mapping the intensity distribution

The mapping of the intensity consists of measuring the intensity at different positions in a plane. Figure 4 shows a diagram of how the mapping is done.

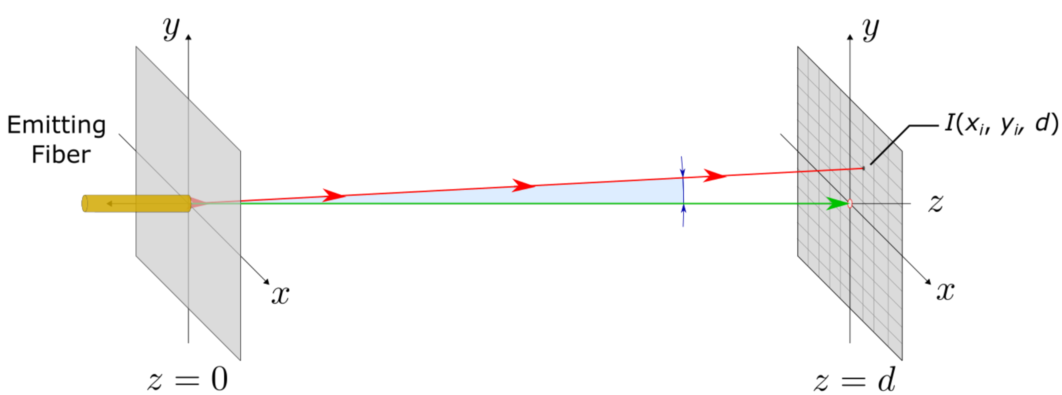

Figure 4. Mapping of light coming from a fiber.

The emitting fiber is fixed on the position *z* = 0. The light coming from the fiber can be captured at any distance *z;* thus, a *z* position must be selected before doing the mapping. Once a position *z* = *d* is chosen, the light intensity is mapped at different coordinate positions (x_i, y_i, $z = d$).

Once the intensity is measured at different positions, it is possible to fit a Gaussian function and estimate the parameters of the Gaussian function. To understand how the fit is made, it is important to understand the least-square method.

2.2.1 Least-squares method

The least-squares method (LSM) is a regression technique used to determine the parameters of the chosen theoretical model describing the experimentally obtained or observed data. It is commonly used to infer relations between two characteristics, for example, height and age. The method consists of minimizing the sum of the square error between the data and the associated Equation (Hansen et al., 2013).

In this work, the intensity of the light from the emitting fiber is measured by a photodetector through another fiber, scanning the intensity distribution profile at given distance from the emitting fiber. Instead of scanning, similar intensity distribution can be obtained by any image sensor like CCD or CMOS with adequate sensitivity within the required wavelength range. Mapping of the intensity data over 2D plane produces a dataset $I_i = I(x_i, y_i, z = d)$. Thus, the LSM will consist of fitting a Gaussian function (2.16) to the data by minimizing the sum (Hansen et al., 2013)

$$\min \sum_{i=1}^{N}[I_i - f(x_i, y_i; A_0, w, x_0, y_0)]^2, \tag{15}$$

by adjusting parameters A_0, w, x_0, y_0 of the function $f(x_i, y_i; A_0, w, x_0, y_0)$, which is a simplified version of the right-hand side of the Equation (2.16)

$$f(x_i, y_i; A_o, w, x_o, y_o) = A_o \mathrm{e}^{-\frac{\left[(x-x_i)^2+(y-y_i)^2\right]}{w^2}}, \tag{16}$$

and $w = W/\sqrt{2}$. Once this is accomplished, the position of the center of the Gaussian light intensity distribution, at the given distance from the emitting fiber, can be found.

2.2.3 Calculation of 3D position

Finding the 2D position of the centroid of the Gaussian light distribution at a known *z* position is enough to find the fiber core 3D spatial localization. To achieve this, it is necessary to estimate the light distribution parameters at two different *z* positions. After having the Gaussian function parameters for two *z* positions and considering that the light coming from the fiber draws a cone, the coordinates of the fiber core position can be obtained. This will be explained in more detail in chapter 4.

2.3 Error theory

When dealing with measurements, errors are always present. In this work, the errors are important since these will affect the results of the measurements. The possible errors are noise in the photodetectors and amplifiers, and incorrect light intensity mapping due to errors in the scanning system.

In the case of the photodetectors, the errors in signals appear due to fluctuations caused by thermal and shot noise, or by electromagnetic interference from external sources.

Also, there can be incorrect signal sampling during the light intensity mapping. For example, when using a scanning system with a probe fiber, the positional sensors of the translation stages may have their own errors meaning that measured light intensity is assigned to a wrong position. Moreover, the mechanics of the experimental setup can suffer from thermal expansion effects, hysteresis and other imperfections. Possible vibrations caused by movements during the scanning with a probe fiber could cause the probe to capture light from multiple positions, which could also affect the measurement.

The position and angle of the probe and the emitting fibers with respect to the reference z-axis are also important. As seen in Figure 3, the emitting fiber is set in a plane and the mapping is done on a parallel plane. Suppose the probe is too far from the light source, in that case, it will not capture the light. On the other hand, if the fibers are not centered and parallel to the Z-axis, the mapping will not be done correctly, and the resulting Gaussian function will be in a different position with respect to the correct Gaussian function; this is addressed in more detail in chapter 4.

Other errors might be present, which is why an analysis of the results is needed. It is important to introduce some basic error theory ideas to do error analysis and understand the role that the errors play in this work.

2.3.1 Lower bounds in parameters estimation

The presence of the errors in measurements that were mentioned above suggest their propagation to the intermediate results, such as estimated parameters of the Gaussian intensity distribution in the planes of scanning, and to the final results, the coordinates of the fiber core in 3D space.

The errors in the estimated parameters of the Gaussian intensity distribution are characterized by its variance, which describes their uncertainty or the variability of random fluctuations of the estimated parameter due to the random noise or errors in the initial data set. The statistics theory allows the evaluation of the lower bound, or, the minimum achievable variance of the estimated parameters depending on the level of the input noise and the amount of the information obtained during the measurements. This lower bound can be found from well-known Cramer-Rao inequality (Cramer, 1946).

Assuming that measured data is represented by a set of sampled values ξ_n that are random because of noise or other random measurement errors. As random ξ_n can be characterized by a probability distribution $p(\xi_n,\theta)$, where θ is the parameter that must be found from data set ξ_n. The Cramer-Rao bound for variance of θ estimate can be calculated as (Cramer, 1946):

$$\sigma_\theta{}^2 \geq \frac{1}{I(\theta)}, \tag{17}$$

where I(θ) is the Fisher information defined as

$$I(\theta) = \boldsymbol{E}\left[\sum_{n=1}^{N}\left\{\frac{\partial}{\partial\theta}\log\left(p(\xi_n,\theta)\right)\right\}^2\right] = \sum_{n=1}^{N}\frac{\left(\frac{\partial}{\partial\theta}f_n(\theta)\right)^2}{\sigma^2}. \tag{18}$$

Here, symbol **E** denotes the mathematical expectation. It is also assumed here, that the probability distribution of the sampled values ξ_n is normal

$$p(\xi_n, \theta) = \frac{1}{\sigma\sqrt{2\pi}} e^{-\frac{[\xi - f_n(\theta)]^2}{2\sigma^2}}, \tag{19}$$

and the function $f_n(\theta)$ describes the mathematical expectation value of the *n*-th sample depending on the parameter θ.

In the case of measurement of the 2D intensity map with the purpose to find the parameters of the Gaussian distribution, the sampled values ξ_n represent the intensity at *n*-th position in the plane of scanning, and the parameter θ becomes, in fact, a vector of the parameters of the Gaussian function, (A_o, w, x_o, y_o), that have to be estimated from the intensity measurements. The theoretical calculations of the Cramer-Rao lower bounds for the center coordinates x_o and y_o, and the width, w, using this approach will be presented in Chapter 4.

2.3.2 Error propagation

The final result, the 3D coordinates of the fiber core, can be calculated using the geometry laws from the estimated Gaussian function parameters after measuring the light intensity distribution within, at least, two scanning planes. Therefore, the errors in the estimated center coordinates x_o and y_o and the width w, will finally propagate to the calculated 3D coordinates of the fiber tip. The Equations for calculation of the coordinates, x_i, will include the estimated Gaussian function parameters θ_j, as multiple input variables:

$$x_i = X_i(\theta_1, \theta_2, \dots, \theta_M), \tag{20}$$

The errors in the calculated coordinates x_i can be characterized by the variance ${\sigma_i}^2$

$${\sigma_i}^2 = \sum_{j=1}^{M} \left(\frac{\partial X_i}{\partial \theta_j}\right)^2 {\sigma_j}^2, \tag{21}$$

where ${\sigma_i}^2$ is the variance of the estimated j-th parameter of the Gaussian intensity distribution.

2.4 Measurements: basic terms

It will be important for this work to introduce some measurement concepts to understand the theoretical models and the results. These concepts are commonly used when working with measurements of any type, which is why they are important. In this section, these concepts will be introduced, and simple examples will be given to understand their importance.

2.4.1 Accuracy

Accuracy is a term that designates how close a measured value is from the true value. This can be obtained by looking at how close is the average of all measurements to the real value. An excellent example can be made when shooting a target. Figure 5 shows four targets that represent separated cases.

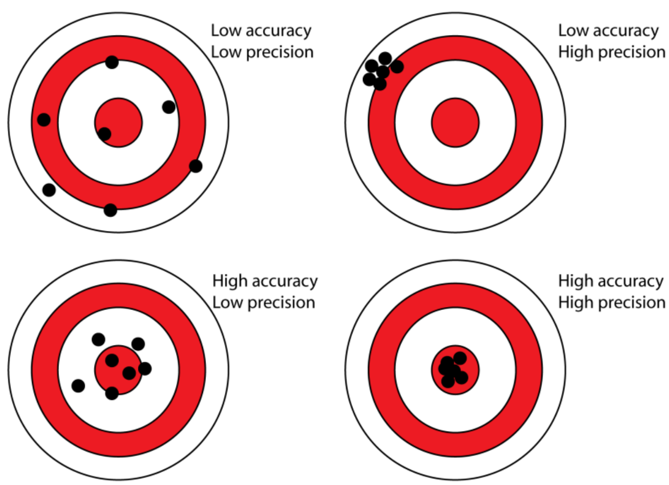

Figure 5. Shooting targets used to represent accuracy and precision (Betham, 2020)

This work main objective is to obtain the position of a fiber core; thus, accuracy plays a significant role. Since it is impossible to estimate the core position true value, due to the limits of the measuring system, it is important to obtain a value as close as possible to the real value. The necessary accuracy depends on the application. In this work it is desired that the measurement has an accuracy of 100 nm, which means that the obtained position should only have a difference of 100 nm meter with respect to the true value.

2.4.2 Resolution

Another essential concept, of the measurement theory, is the resolution. Resolution is defined as the smallest increment of the measured parameter that the system can display or measure. It is important to highlight that measuring small increments is not enough to have a good measurement since there could be high resolution with poor precision and accuracy. Although a high resolution does not imply high accuracy, it is necessary for high accuracy. For example, to obtain an accuracy of 100 nm, for the fiber core position, the measuring system should distinguish distances of at least 100 nm; otherwise, it would be impossible to distinguish between positions that are 100 nm away from a point. If positions that are 100 nm away are indistinguishable, then it cannot be said with complete certainty which position is the true position in the scale of 100 nm.

2.4.3 Uncertainty

The uncertainty is an expression of the variability of a measured quantity. This is commonly referred to as the standard deviation and gives information about the possible values obtained during a measurement. For example, the presence of vibrations in the measuring system will cause variabilities in estimating the core position. Knowing how variabilities behave is of great importance since it gives information that could minimize these variations or, if possible, eliminate them.

2.4.4 Stability

During a measurement, there can be changes with time. These variations may affect or not a specific measurement, which will depend on the accuracy needed. A system is said to be stable if the variations do not affect the measurement accuracy. The variations might change with time, and these could decrease; thus, a system could start being unstable and reach a steady state after some time has passed. In this work, stability plays an important role in estimating the Gaussian parameters since the resulting measurements show oscillations with a high frequency, but after some time, the oscillations frequency decreases significantly; thus the system becomes more stable. The previous example will be explained in more detail in the results section.

Chapter 3. State of the art in the core position measurement systems

As mentioned in the introduction, the quality control and the production of fiber-optic components must include the capability to measure the fiber core’s position. This capability is essential to guarantee minimal light losses in fiber-optic interconnections and fiber-chip connections. This is particularly important in multi-fiber and multicore configurations because having multiple cores with significant losses will cause the entire system to fail, whether it is a system used for telecommunications, computing or other field that uses this technology.

Measuring the core position is not an easy task because some degree of accuracy must be reached. Depending on the specific application, the required accuracy for core position measurements might be from 500 nm up to very accurate 100 nm. Some applications may require a better accuracy in their measurements.

In this chapter, three methods used to measure fibers’ core parameters will be described. After that, some commercial systems used to measure fiber core parameters will be presented.

3.1 Techniques to measure core characteristics and position

Since this work is dedicated to the development and characterization of a method for measuring a fiber core position, three already known techniques designed for this purpose, and their accuracy specifications will be presented here. The first one, only measures the light losses introduced by fiber-optic connectors; the remaining two provide information about the fiber core position.

3.1.1 Simple comparative testing

Simple testing techniques use reference cables and connectors with known parameters to characterize the components under test by comparison between the introduced light losses (NECA, 2016).

The reference connectors, in turn, require their own procedures for selection and quality control, which includes precise measurement of the connector, of the geometrical and optical characteristics. The geometrical characteristics can be measured by a CCD camera and a translation stage to obtain the fiber cores position. Light losses are measured separately for each fiber. The work by Kato (Kato et al., 2010) presents the procedure for the production and characterization of the reference multi-fiber push-on (MPO) connector with eccentricity below 0.45 µm.

Simple tests are mainly for quality control, and do not provide information about the core positions.

3.1.2 System with circularly moving reference fiber array

This system uses light coming out of a reference fiber array. Instead of measuring light losses, for quality control, this method that also uses a reference fiber array that provides information about the position of every core in the sample fiber array.

The reference fiber array with known parameters (standard array) is placed at the distance of 50 µm in front of the array under test (sample array). The sample array is fixed, and the standard array is mounted on a high-speed actuator, as shown in Figure 6 (Ozawa K. et al., 1995).

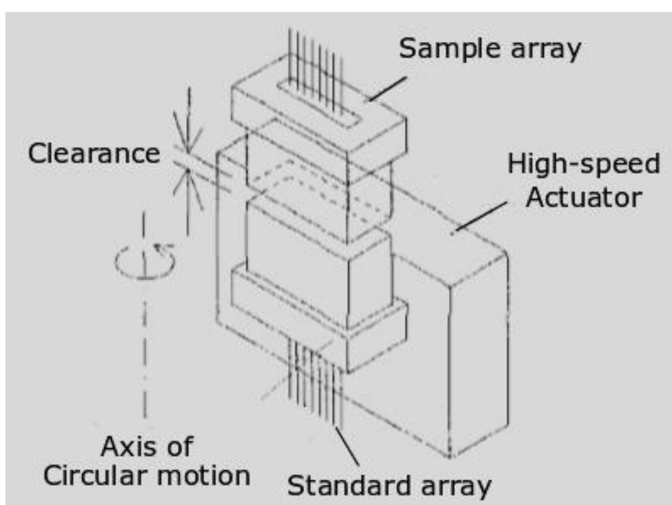

Figure 6. System used to find the core position by using a standard array of fibers (Ozawa K. et al, 1995)

The high-speed actuator moves the fibers in a circular motion at a frequency of 1 kHz around the points where the centers of the tested fibers must be, see Figure 7.

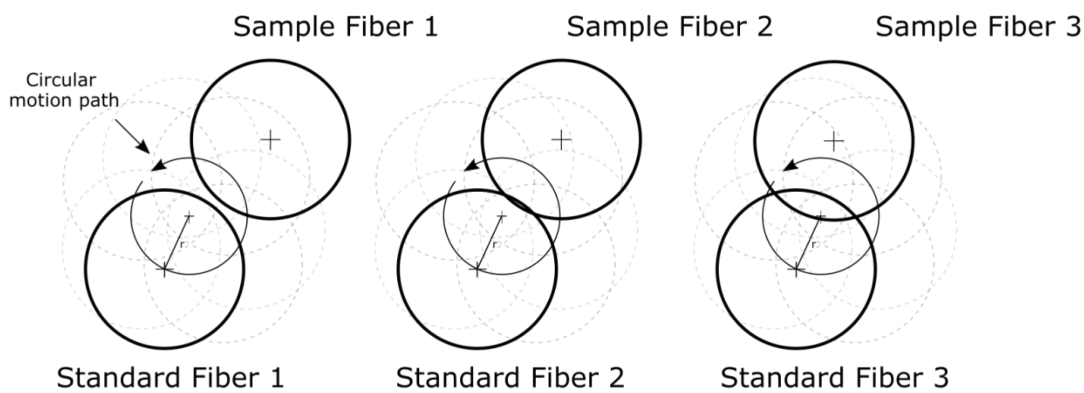

Figure 7. Circular motion.

If all the cores of the sample fiber array are perfectly positioned relative to each other, the centers of the reference array would circularly move around the centers of the sample fibers at the same distance. This distance is equal to the radius of the circular movement, and the signal from each fiber would not change. However if any fiber of the sample array has an offset from its required position, then the signal from that fiber will be periodically modulated, as shown in Figure 8.

The modulation depth of the signal from the particular fiber of the sample array depends on the radial offset of the core of this fiber. The offset is with respect to the center of the circular motion of the corresponding fiber in the standard array. In addition to this, the signal will show a phase shift, which is dependent on the angular offset of this fiber.

The standard deviation of the position measurement errors when using this method was reported to be within 0.05 µm (Ozawa K. et al., 1995).

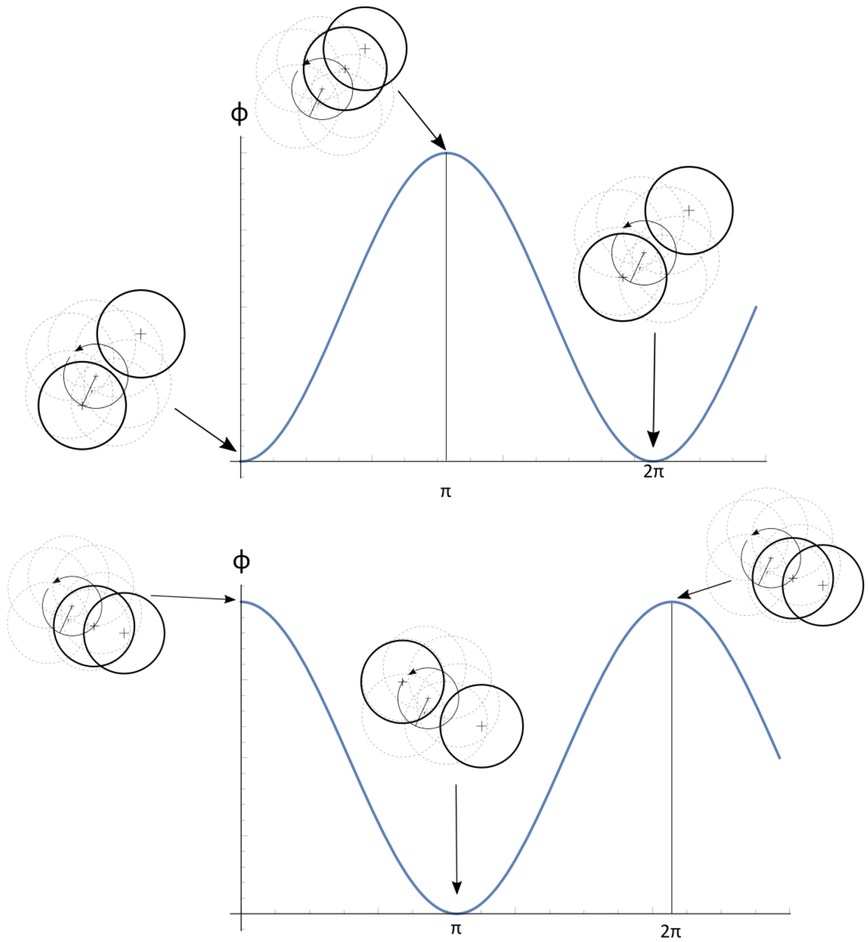

Figure 8. Periodic variation of transmitted light.

3.1.3 Calibrated mask method

This method of the core position measurement uses a CCD and a calibrated mask as a coordinate reference (Hsu S. W. et al., 2005). The setup is shown in Figure 9.

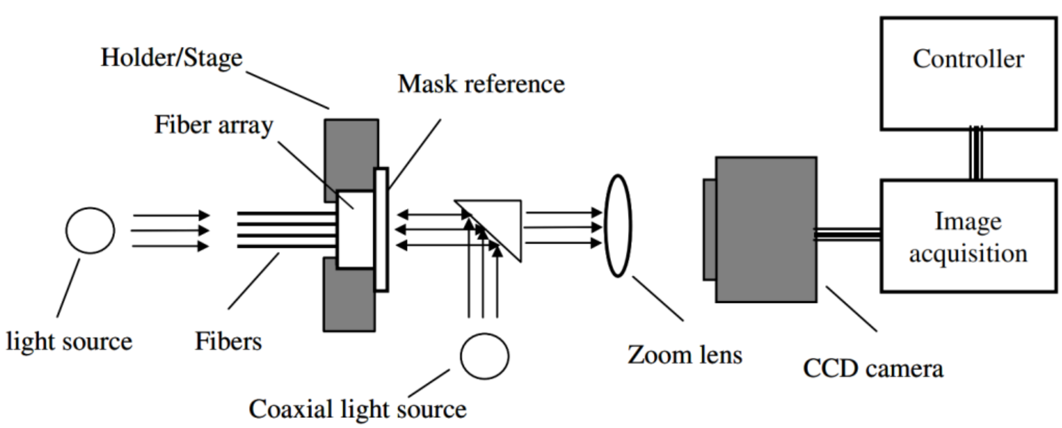

Figure 9. Schematic diagram for the calibrated mask method (Hsu S. W. et al., 2005)

One of the most important components of the system is the mask. The mask is created with a laser by writing a reflective coating with square holes on a glass substrate. Then it is calibrated with a precise optical system to obtain the exact position of the square holes etched in the mask. Once it is calibrated, the mask is placed in a holder that can be moved with a stage. Finally, the array that will have their cores positions measured is mounted in the same holder adjacent to the mask.

To get a measurement of the fiber core position, the light coming from the fiber array and the light from the coaxial source reflected from the mask pass through a zoom lens to the CCD camera. The CCD is reading the composite image of both the fiber array and reference mask that is subsequently processed by a computer. Since the mask reference points positions (square holes corners) are precisely known, the offset of the cores are measured with respect to the holes in the mask.

The method showed a standard deviation of 0.3 μm and a measuring time of 0.1 seconds. Partially the errors of this measurement are due to the limited resolution of the CCD. Additionally, because of low sensitivity of CCD for the wavelengths above 1000 nm, this technique cannot be applied for telecommunication fiber-optic components operating within the 1300-1550 nm range.

3.2 Commercial systems

At present, there are already commercial measuring systems that measure the Fiber core position. Some examples are:

V-groove board, fiber array inspection machine (YGN-590-FAVG):

This system uses a CCD camera and a laser to do the measurements. The system takes images of a fiber array front face and of the v-groove boards. The images get processed and finally give a measurement of the angle and height of the V-grooves, the pitch between grooves and the fiber core X and Y offsets. According to Yagishitagiken the system has a repeat measuring precision of 0.1 μm, but it does not specify for which fiber this repeatability was measured (Yagishitagiken, 2020).

Figure 10. V-groove board, fiber array inspection machine YGN-590-FAVG (Yagishitagiken, 2020).

FGC-GA Geometry System:

This system uses darkfield illumination to capture an image of the fiber array front face with a CCD. This system can do measurements of the geometry of the widest range of optical fibers, V-groove arrays, and ribbon connectors. With one unit, it is possible to characterize V-grooves, core to core pitch, and X and Y offset of multi-fiber arrays (Arden Photonics, 2020). The system has a repeat measuring precision of 0.25 µm with a single and 3-fiber array of 540/600 µm.

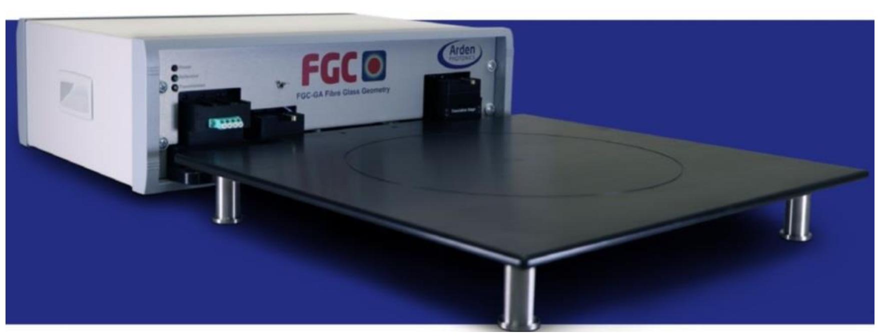

Figure 11. FGC-GA Geometry system (Arden Photonics, 2020).

Chapter 4. Theoretical analysis

This chapter presents a theoretical research which includes, first, the elaboration of the Equation for the fiber core 3D coordinates from the estimated parameter of the Gaussian intensity distribution measured within planes at two different distances from the fiber. Second, the description of the light power transfer from the fixed emitting fiber to the scanning probe fiber. The third part is dedicated to the evaluation of the best achievable accuracy, in terms of uncertainty, for the estimation of two parameters of the Gaussian intensity distribution: the centroid coordinates for 1D and 2D scans, and the width of the intensity distribution. Finally, this chapter also presents an evaluation of the photodetector signal value from an emitting fiber.

4.1 Calculation of 3D position

The main objective of this work is to obtain a value for the (x, y, z) position of the fiber core. To do this, it is assumed that the light coming from the fiber can be described by a Gaussian field and there are two known positions $P_1(x_1, y_1, z_1)$ and $P_2(x_2, y_2, z_2)$, which are the centroids of the Gaussians, that were obtained with the measuring system. Their corresponding Gaussian widths w_1 and w_2 are also known, since the measurement gives all the Gaussian parameters. With this information and following the diagram shown in Figure 12 it is possible to calculate the position of the fiber core $P_0(x_0, y_0, z_0)$.

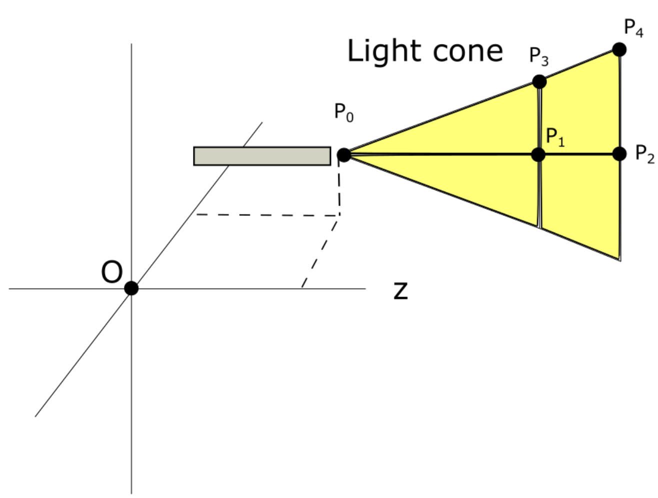

Figure 12. Optical fiber with a light cone embedded in 3D space.

As it can be seen in Figure 12, a triangle can be obtained from the light cone and by using the known positions and widths; two similar triangles are obtained $\Delta P_0P_2P_4$ and $\Delta P_0P_1P_3$. By using the similar triangle property, with vectors, the following Equations are obtained:

$$\frac{x_0 - x_1}{w_1} = \frac{x_0 - x_2}{w_2}, \tag{22}$$

$$\frac{y_0 - y_1}{w_1} = \frac{y_0 - y_2}{w_2}, \tag{23}$$

$$\frac{z_0 - z_1}{w_1} = \frac{z_0 - z_2}{w_2}. \tag{24}$$

With these expressions three Equations for the fiber core position coordinates are obtained:

$$\begin{cases} x_0 = f(x_1, x_2, w_1, w_2) = \frac{x_1 w_2 - x_2 w_1}{w_2 - w_1}, \\ y_0 = g(x_1, x_2, w_1, w_2) = \frac{y_1 w_2 - y_2 w_1}{w_2 - w_1}, \\ z_0 = h(x_1, x_2, w_1, w_2) = \frac{z_1 w_2 - z_2 w_1}{w_2 - w_1}. \end{cases} \tag{25}$$

Having obtained the expressions for the 3D coordinates of the fiber core, the next step will be to analyze the effects of the incidence angle of emitted light and position on the amount of acquired light. This will be done by considering that a fiber is used to capture light from an emitting fiber that also has an angle and position.

4.1.1 Light Transfer between the fibers

The analysis of the signal detected by scanning the light intensity distribution from the emitting fiber by another, receiving or probe fiber, must be performed in order to understand the dependence of the signal on the position of the scanning fiber, and on possible misalignment of these two fibers. Here, this analysis will be performed using approximation of the intensity distribution by Gaussian function (Li and Guo, 2010; Nicolaisen and Danielsen, 1983; Andrew et al., 2006), as was described in Chapter 2.

4.1.1.1 Distribution of light intensity

One of the most important characteristics of the fiber is the numerical aperture NA, which, for step-index fibers, is defined by the refractive indices of the core n_{core}, and cladding n_{clad} (Saleh and Teich, 1991)

$$NA = \sqrt{n^2{}_{core} - n^2{}_{clad}}. \tag{26}$$

The numerical aperture and the divergence angle Θ_{max}, of the light emitted by the fiber are linked by the following Equation:

$$NA = \sin\Theta_{max}. \tag{27}$$

The divergence angle defines the angular distribution of the light intensity. Assuming that the optical axis of the emitting fiber is aligned along the *z*-axis, and introducing angles ϕ and ψ, as shown in Figure 13, the angular distribution of intensity, by using Gaussian approximation, can be written as

$$I(\phi,\psi,z) = I_z(z)\mathrm{e}^{-\frac{2(\phi^2+\psi^2)}{\Theta^2{}_{max}}}. \tag{28}$$

Here, the function $I_z(z)$ represents the dependence of the maximum intensity value on

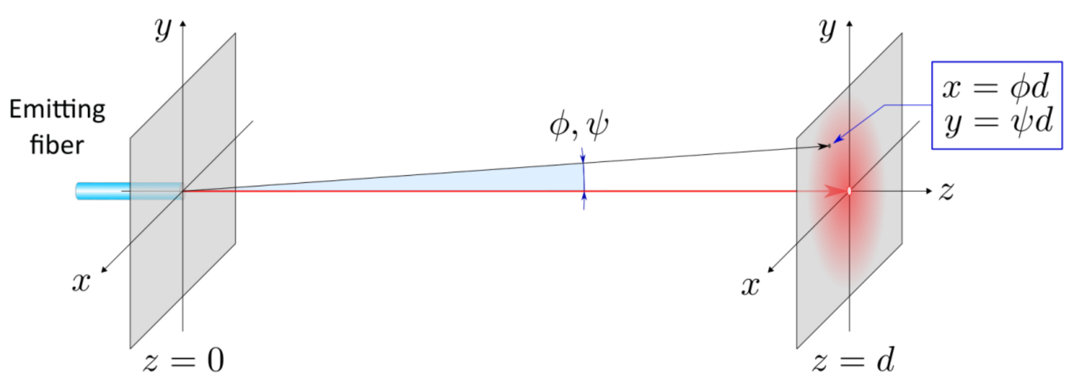

Figure 13. Intensity distribution in far-field of the single-mode fiber. For simplicity, we assume that the angles ϕ and ψ are small.

the distance from the tip of the fiber. When using the Gaussian profile approximation, the half-width of the light cone at the level $1/e^2$ from maximum intensity W, can be calculated at different distances from the tip z, with the following Equation (Saleh and Teich, 1991)

$$W(z) = W_o\sqrt{1 + \left(\frac{z}{z_o}\right)^2}, \tag{29}$$

where z_o is the Rayleigh length,

$$z_o = \frac{\pi W_o{}^2}{\lambda}, \tag{30}$$

where λ is the light wavelength in the vacuum, and W_o is the waist half-width. The value $2W_o$ is also considered as the mode field diameter of the fiber.

At large distance from the fiber tip, when $z >> z_o$, that corresponds to far field conditions, and when the numerical aperture is small,

$$W \approx \frac{W_o}{z_o} z = \Theta_{max} z, \tag{31}$$

and the intensity distribution can be written as

$$I(x, y, z) = I_z(z) e^{-\frac{2(x^2+y^2)}{W^2}}. \tag{32}$$

This Equation will be used to evaluate the signal value during the scanning of the light intensity distribution with another, receiving fiber, at different distances.

4.1.1.2 Acceptance function

It is known that optical fibers are characterized by acceptance angle, Θ_A, which is related to the numerical aperture, NA, in the same way as the divergence angle (27):

$$NA = \sin \Theta_A. \quad (33)$$

In the multi-mode fibers, most of the captured light comes within the acceptance cone, defined by this angle. Single-mode fibers do not cut off the light with the incident angle above the acceptance angle absolutely, but an amount of the captured light is greatly reduced, In fact, the light power will be slightly reduced even at much smaller incident angles. This behavior is well described as a tilt loss in fiber-optic connectors and fiber splices (Gloge, 1976; Sutherland et al., 1995).

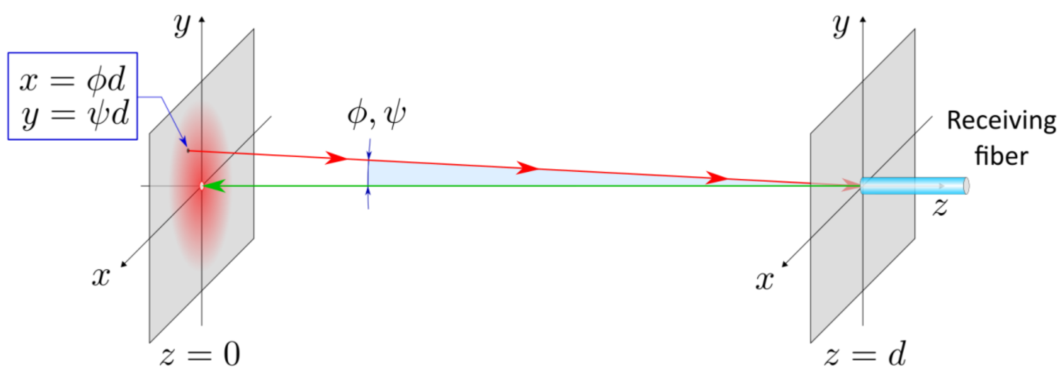

Figure 14. Acceptance function describes the dependence of the amount of light captured by the single-mode fiber on the incident angle. For simplicity, we assume that the angles ϕ and ψ are small.

Here, the dependence of the amount of captured light on the incident angle will be characterized by an acceptance function, $\kappa(\phi, \psi)$. Similar to antennas for transmission or reception of the electromagnetic waves, which show the property of reciprocity. This means that their directional diagrams for transmission and reception are the same. The acceptance function also determines the function describing the angular distribution of the intensity of the light entering the fiber (4.7):

$$\kappa(\phi, \psi) = \mathrm{e}^{-\frac{2(\phi^2+\psi^2)}{\Theta^2{}_{max}}}. \quad (34)$$

If the point light source has the (x, y, $z = 0$), as shown in Figure 14, the power of the light captured by the receiving fiber must be multiplied by a factor of

$$\kappa(x, y) = \mathrm{e}^{-\frac{2(x^2+y^2)}{W^2}}, \quad (35)$$

where $W = d\Theta^2{}_{max}$.

4.1.1.3 Light power transfer function

Knowing the intensity distribution and acceptance function, it is possible to evaluate the amount of light transfer between the emitting and receiving fiber, as shown in Figure 15.

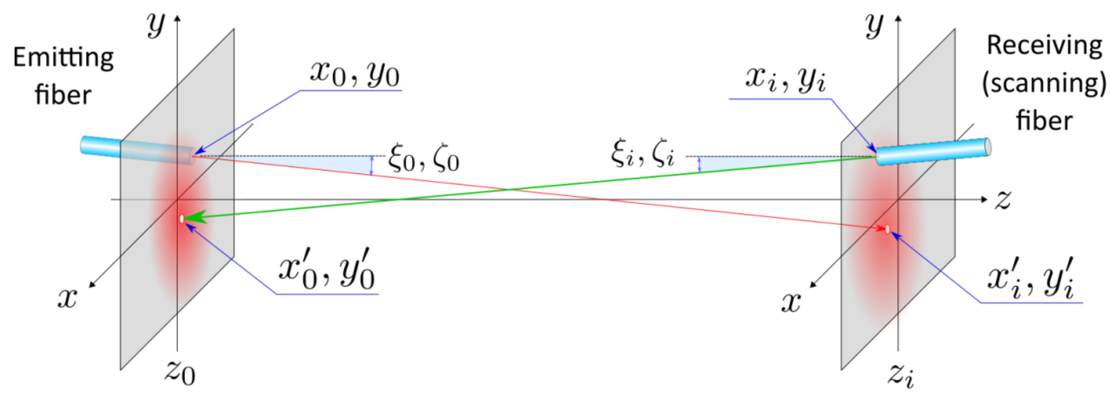

$$x'_0 = x_i + (z_i - z_0)\,\xi_i \qquad x'_i = x_0 + (z_i - z_0)\,\xi_0$$
$$y'_0 = y_i + (z_i - z_0)\,\zeta_i \qquad y'_i = y_0 + (z_i - z_0)\,\zeta_0$$

Figure 15. Optical power transfer from emitting to receiving fiber. For simplicity, we assume that the angles ϕ and ψ are small.

Indeed, on the one hand, the light intensity (28) at the tip of the receiving fiber located at the point with coordinates (x_i, y_i, z_i) can be written as

$$I(x,y) \sim \mathrm{e}^{-\frac{2\left[(x_i - x'_i)^2 + (y_i - y'_i)^2\right]}{w^2}} = \mathrm{e}^{-\frac{2\left[\{x_i - [x_0 + (z_i - z_0)\xi_0]\}^2 + \{y_i - [y_0 + (z_i - z_0)\zeta_0]\}^2\right]}{w^2}}, \tag{36}$$

where ξ_0 and ζ_0 are the components of the tilt angle of the emitting fiber. On the other hand, the acceptance factor (35) for the light coming from the position of the emitting fiber (x_0, y_0, z_0),

$$\kappa(\phi,\psi) = \mathrm{e}^{-\frac{2\left[(x_0 - x'_0)^2 + (y_i - y'_0)^2\right]}{w^2}} = \mathrm{e}^{-\frac{2\left[\{x_0 - [x_i + (z_i - z_0)\xi_i]\}^2 + \{y_0 - [y_i + (z_i - z_0)\zeta_i]\}^2\right]}{w^2}}, \tag{37}$$

where ξ_i and ζ_i are tilt components of the receiving fiber. The product of $I(x_i, y_i, z_i)\kappa(x_0, y_0)$ from (36) and (37) can be easily calculated by summation of the exponents arguments. To simplify the elaboration, the difference of z-coordinates can be substituted by the distance between the fibers, $d = z_i - z_0$, also, x- and y-related terms can be separated. For example, summation of x-related terms yields

$$\{x_i - [x_0 + (z_i - z_0)\xi_0]\}^2 + \{x_0 - [x_i + (z_i - z_0)\xi_i]\}^2 = \frac{d^2(\xi_0+\xi_i)^2}{2} + 2\left(x_{i,max} - x_i\right)^2, \quad (38)$$

where $x_{i,max}$ is the position of the receiving fiber along the x_i-axis, where the light transfer reaches its maximum:

$$x_{i,max} = \frac{d(\xi_0-\xi_i)}{2} + x_0. \quad (39)$$

After obtaining similar Equations for *y*-coordinates with

$$y_{i,max} = \frac{d(\zeta_0-\zeta_i)}{2} + y_0. \quad (40)$$

And using the relation between the distance *d* and the width of the intensity distribution $W = \Theta_{max}d$, the light transfer function can be written as

$$T(x_0, y_0, z_0; x_i, y_i, z_i) = \mathrm{e}^{-\frac{(\xi_0+\xi_i)^2+(\zeta_0+\zeta_i)^2}{\Theta^2 max}} \mathrm{e}^{-\frac{2\left[(x_{i,max}-x_i)^2+(y_{i,max}-y_i)^2\right]}{W^2}}. \quad (41)$$

As can be seen from the Equations (39), (40) and (41), the fibers misalignment leads to the shift of the position of the signal maximum and reduces the signal amplitude, and, therefore, should be minimized. However, if the tilt angles are fixed, then this offset can be calculated and taken into account in final estimation of the position of the emitting fiber.

From the Equation (41) it also follows that the transfer function in the receiving plane (x_i, y_i,) keeps the Gaussian profile but half-width at $1/e^2$ -level is $\sqrt{2}$ times less than that of the intensity distribution in this plane. Further, to characterize the width of the signal, ω, it will be defined at the level of 1/*e* form its maximum, so that

$$w = \frac{W}{2} \approx \frac{NA\, d}{2}. \quad (42)$$

Here, it is assumed that divergence angle is small, and, therefore Θ_{max} = *NA*.

4.2 Cramer-Rao bounds

In the proceeding sections, theoretical models that will give information about the variations of each coordinate are proposed. First in section 4.2 a model that can be used for the variation of the *x* and *y* coordinates of positions P_1 and P_2 in 1D and 2D will be presented, and finally in section 4.3 a model for the variation of the P_0 coordinate will be addressed.

Typically, the noise appears during the light detection with the photodetector and its further amplification. One way to evaluate the variations of an estimated parameter, caused by noise, is the calculation of Cramer-Rao bound, as it was described in Chapter 2.

In this section three different theoretical models, for the evaluation of variations, will be addressed. First a model for the 1D line scanning is presented, then a model for the 2D mesh-like scanning, and finally an expression for the variance that depends on the distance between fibers will be obtained.

4.2.1 1D scans

For the 1D scan model it is first assumed that the light emitted by the fiber at some distance forms a light intensity distribution which can be described by a Gaussian function

$$f(x,\tilde{x}) = A_0 e^{-\frac{(x-\tilde{x})^2}{w^2}}, \tag{43}$$

where A_0 is the amplitude, $\tilde{x}$ is the center of the Gaussian distribution, and *w* is its width.

When another fiber's tip scans the intensity distribution, the recorded signal will contain noise. Supposing the noise has thermal nature; therefore, it is normally distributed. The probability distribution of a signal value ξ can be described as

$$p(\xi,\tilde{x}) = \frac{1}{\sigma\sqrt{2\pi}} e^{-\frac{|\xi - f(x,\tilde{x})|^2}{2\sigma^2}}, \tag{44}$$

where σ is the standard deviation. If the noise in different samples (measurements of the light intensity at different coordinates x_n) is independent, the Fisher information can be written as in Equation (18). Substituting (43) in (18) leads to

$$I(\tilde{x}) = \frac{4A^2}{w^4\sigma^2}\sum_{n=1}^{N}(x_n - \tilde{x})^2\, e^{-\frac{2(x_n-\tilde{x})^2}{w^2}}. \tag{45}$$

When the intensity distribution is equally sampled within the interval *x* ϵ [θ-αω … θ+αω] along the *x*-coordinate, for a large number of samples,

$$\sum_{n=1}^{N}(x_n - \tilde{x})^2\, e^{-\frac{2(x_n-\tilde{x})^2}{w^2}} \approx N\frac{1}{2aw}\int_{-aw}^{+aw} x^2 e^{-\frac{2x^2}{w^2}}dx, \tag{46}$$

and therefore, after the evaluation of the integral (46) the expression (45) can be represented approximately as

$$I(\tilde{x}) \approx \frac{NA^2}{w^2\sigma^2}\frac{\left[\frac{1}{4}\sqrt{2\pi}\,\mathrm{erf}\left(\sqrt{2}a\right) - ae^{-2a^2}\right]}{a}. \tag{47}$$

Finally the noise-limited accuracy of the evaluation of the centroid position can be calculated from the following Equation

$$\sigma_{\tilde{x}}{}^2 \geq \frac{1}{I(\tilde{x})} \approx \frac{w^2\sigma^2}{NA^2}\frac{1}{\psi(a)}, \tag{48}$$

where the function

$$\psi(a) = \frac{\frac{1}{4}\sqrt{2\pi}\,\mathrm{erf}\left(\sqrt{2}a\right) - ae^{-2a^2}}{a}, \tag{49}$$

can be evaluated to find the best sampling interval from the parameter *a*. This function is shown in Figure 16.

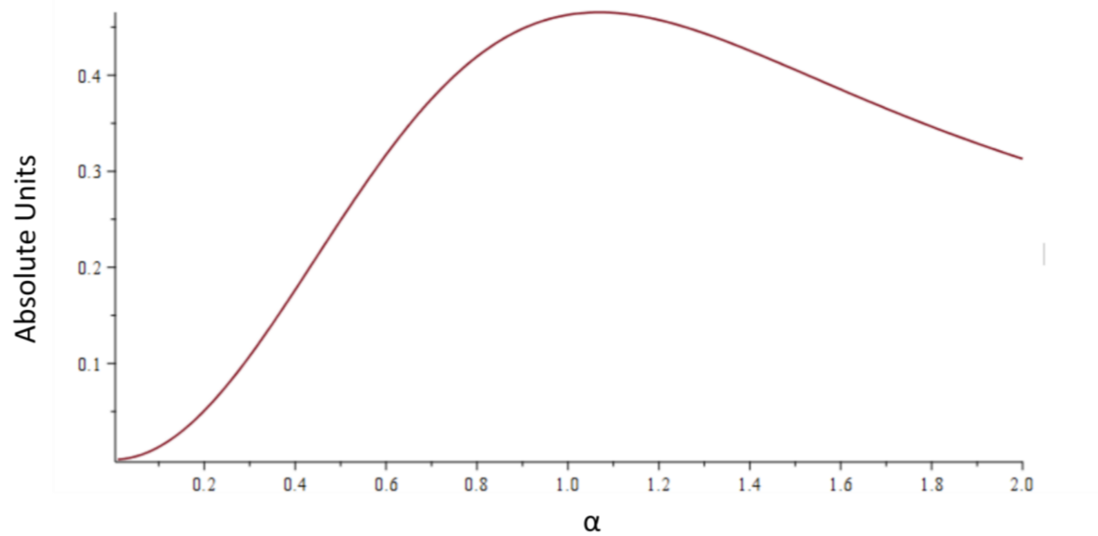

Figure 16. Function ψ(α).

As shown, ψ(α) reaches its maximum max{ψ(α)}= 0.47 at α=1.07, which means that if *N* samples are equally separated along *x*-coordinate within the interval [$\tilde{x}$-1.07*w* … $\tilde{x}$+1.07*w*] the best accuracy of fiber position estimation that can be reached is

$$\sigma_{\tilde{x}}^2 \geq 2.15\frac{w^2}{N\,{A_0}^2}, \tag{50}$$

where σ_{noise} is the standard deviation of the noise, N is the number of samples taken by intensity distribution measurement, A_0 is the amplitude, and *w* is the width of the Gaussian intensity distribution. When measuring time is not limited, the number of samples *N* can be huge. The signal-to-noise ratio SNR = $(A_0/\sigma)^2$ can be increased, in theory, almost infinitely by averaging. Assuming SNR = 10^4 that corresponds to 40 dB of signal-to-noise ratio, and the intensity distribution width is *w* = 150 µm (about 1 mm from the tip of SMF-28 fiber), the number of samples required to achieve the position uncertainty of σ = 100 nm is

$$N \geq 2.15\frac{w^2}{{\sigma_{\tilde{x}}}^2 SNR} = \frac{2.15 \cdot 150^2}{0.1^2 \cdot 10^4} \approx 484. \tag{51}$$

This result shows that it does not seem too hard to design a system for evaluating the fiber position from the series of measurements of the intensity distribution of the light emitted by the fiber.

4.2.2 2D Scans

Equation (51) is only valid for 1D scans, but in some cases, it can also be used for the evaluation of noise-limited accuracy for 2D scans, for example, a cross like scan where the *x*-axis is scanned first and then the *y*-axis. The cross-like scan might not be optimal, which is why analysis for an equidistant scan within a square should be made.

As was shown in Chapter 2, the circular symmetrical light intensity distribution can be represented as:

$$f(x, y, \tilde{x}, \tilde{y}) = A_o e^{-\frac{(x-\tilde{x})^2+(y-\tilde{y})^2}{w^2}}, \tag{52}$$

where $\tilde{x}$ and $\tilde{y}$ are coordinates of the center of the intensity distribution. Due to the assumed circular symmetry, the evaluation of the noise-limited accuracy for estimating both $\tilde{x}$ and $\tilde{y}$ are equivalent. Therefore only the lower bound for $\tilde{x}$ will be evaluated.

Similar to the Equation (45), the Fisher information for 2D scanning can be written as:

$$I(\tilde{x}) = \frac{4{A_o}^2}{\omega^4\sigma^2}\sum_{k=1}^{N}(x_k - \tilde{x})^2\, e^{-\frac{2[(x_k-\tilde{x})^2+(y_k-\tilde{y})^2]}{w^2}}, \tag{53}$$

where x_k and y_k are 2D coordinates of the samples taken during the scan. For scanned area within a square with a size of $2bw \times 2bw$, and centered at the center of the distribution,

$$\sum_{k=1}^{N}(x_k - \theta)^2\, e^{-\frac{2[(x_k-\tilde{x})^2+(y_k-\tilde{y})^2]}{w^2}} \approx \frac{N}{4b^2w^2}\int_{-bw}^{+bw}\int_{-bw}^{+bw} x^2 e^{-\frac{2(x^2+y^2)}{w^2}}\, dxdy, \tag{54}$$

and, since

$$\frac{1}{4b^2w^2}\int_{-bw}^{+bw}\int_{-bw}^{+bw} x^2 e^{-\frac{2(x^2+y^2)}{w^2}}\, dxdy = \frac{w^2\mathrm{erf}(\sqrt{2}b)\left[\pi\,\mathrm{erf}(\sqrt{2}b) - 2\sqrt{2\pi}be^{-2b^2}\right]}{32b^2}, \tag{55}$$

Fisher information $I(\tilde{x})$ and noise-limited accuracy ${\sigma_{\tilde{x}}}^2$ can be calculated as

$$I(\tilde{x}) = \frac{N{A_o}^2}{w^2\sigma^2}\varphi(\mathrm{b}), \tag{56}$$

and

$$\sigma_{\tilde{x}}{}^2 \geq \frac{w^2\sigma^2}{NA_o{}^2}\frac{1}{\varphi(b)}, \tag{57}$$

where the function

$$\varphi(b) = \frac{\mathrm{erf}\left(\sqrt{2}b\right)\left[\pi\,\mathrm{erf}\left(\sqrt{2}b\right) - 2\sqrt{2\pi}be^{-2b^2}\right]}{8b^2}, \tag{58}$$

reaches its maximum value max{φ(b)} ≈ 0.293 at b ≈ 0.826, so that lower bound for variance of the position estimation for mesh-like scans within a square area of size 2bw is

$$\sigma_{\tilde{x}}{}^2 \geq 3.413\frac{w^2\sigma^2}{NA_o{}^2}. \tag{59}$$

Function φ(b) is shown in Figure 17.

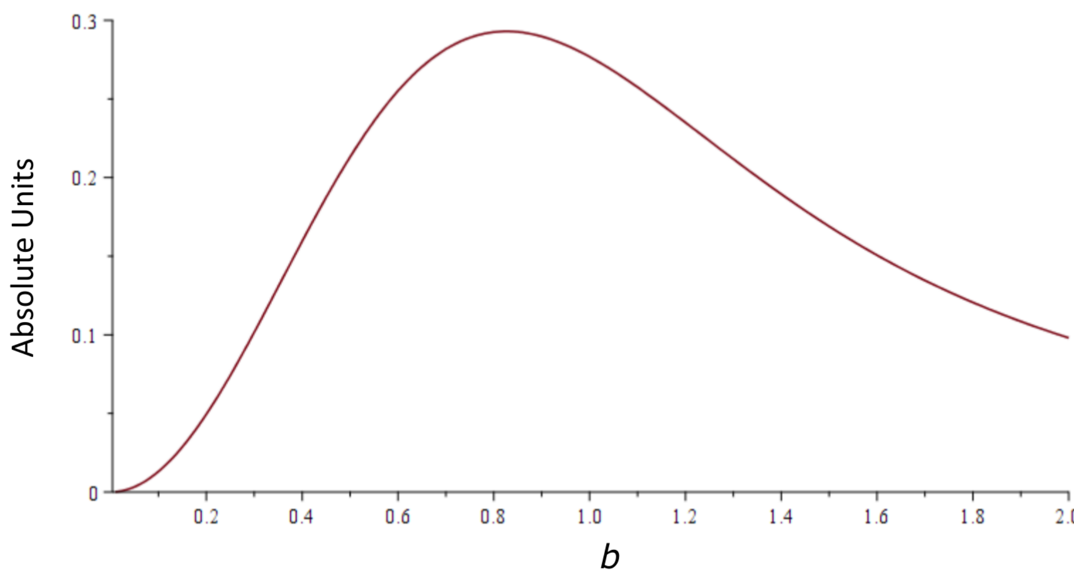

Figure 17. Function φ(b).

It is straightforward to see that the Equations (50) and (59) are very similar, and the values have the same order of magnitude. Therefore, these can be replaced by the general Equation

$$\sigma_{\tilde{x}}{}^2 \geq \alpha \frac{w^2\sigma^2}{NA_o{}^2} \,. \tag{60}$$

The coefficient α depends on the scan geometry but typically within the range of 2-4.

Now that there is an expression to evaluate the center position of the Gaussian distribution taking noise into account, it is important to derive an Equation that gives information on how the accuracy is affected by the distance between fibers.

4.2.3 Width estimation

To calculate the 3D position of the fiber tip, the width of the light distribution also must be found. The noise-limited lower bound for the accuracy of estimation of this parameter can be evaluated using the same method as in the subsections above for 2D mesh-like scan. Introducing the estimated value of the distribution width, w, the Fisher information from the collected data samples for this estimation can be written, similar to (45) and (53), as

$$I(\widetilde{\omega}) = \frac{4A_o{}^2}{w^6\sigma^2} \sum_{n=1}^{N} (x_n{}^2 + y_n{}^2)^2 \, e^{-\frac{2[x_k{}^2 + y_k{}^2]}{w^2}} . \tag{61}$$

For scanned area within a square with size of $2b\omega \times 2b\omega$, and centered at the center of the distribution, assuming a large number of samples,

$$\sum_{n=1}^{N} (x_n{}^2 + y_n{}^2)^2 \, e^{-\frac{2[x_n{}^2 + y_n{}^2]}{w^2}} \approx \frac{N}{4b^2w^2} \int_{-bw}^{+bw} \int_{-bw}^{+bw} (x^2 + y^2)^2 e^{-\frac{2(x^2+y^2)}{w^2}} \, dxdy. \tag{62}$$

And the value of the Fisher information (61) can be approximately calculated as

$$I(\widetilde{\omega}) \approx \frac{NA_o{}^2}{w^2\sigma^2} \chi(\mathrm{b}), \tag{63}$$

where the function χ(b) is defined as

$$\chi(\mathrm{b}) = \frac{1}{2b^2}\left[b^2 e^{-4b^2} + \frac{\pi \mathrm{erf}^2(b\sqrt{2})}{2} - \sqrt{2\pi} b\left(b^2 + \frac{5}{4}\right) e^{-2b^2} \mathrm{erf}(b\sqrt{2})\right]. \quad (64)$$

Both functions, φ(*b*) and χ(*b*) are shown in Figure 18.

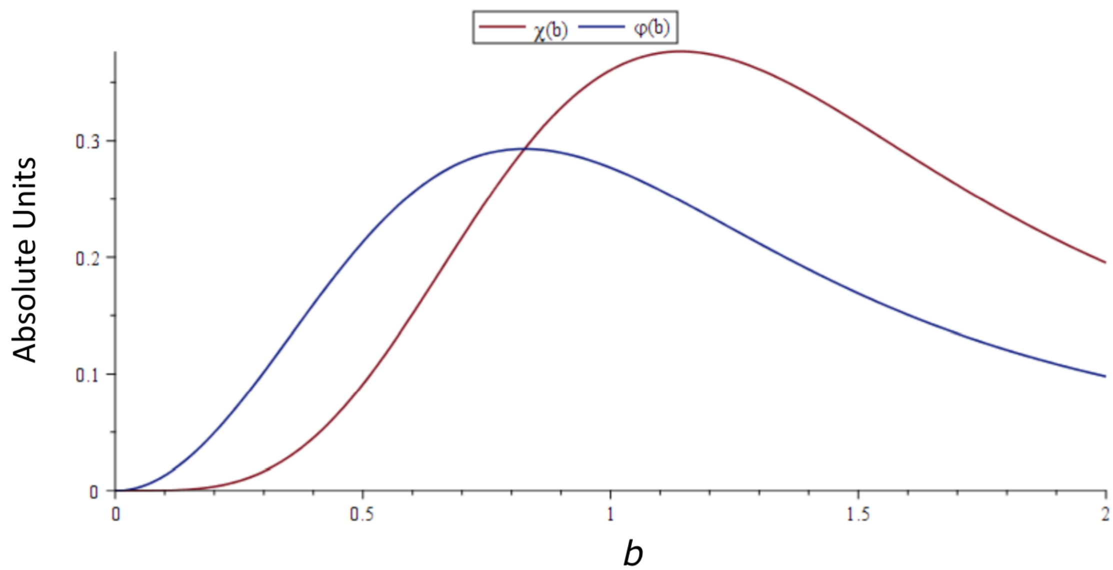

Figure 18. Comparison between function ϕ(α) and χ(b).

A remarkable property of these functions is that when b = 0.826, which corresponds to the maximum of φ(*b*), both functions are equal, χ(*b*) = φ(*b*) = φ_{max}. It means that if one chooses the mesh-like scanning area with equidistant sampling, according to the best accuracy of the estimation, the noise-limited lower bound for the width estimation will be the same as for the position estimation (59):

$$\sigma_{\widetilde{\omega}}{}^2 \geq 3.413 \frac{w^2 \sigma^2}{N\, A_0{}^2}\,. \quad (65)$$

It is clear from Figure 18, that the scanning area can be slightly enlarged up to 1.14 *w* to improve the accuracy. However, the achievable gain is not very significant. Therefore, in further discussion where numerical values of the distribution parameters and their uncertainties are required for the characterization of the system under development, we will use the Equations (59) and (65).

4.2.4 Accuracy at different distances between the fibers

The Equation (50) and (59) estimate the accuracy limits when both the peak amplitude A_0 and the noise variance σ^2 are known. If the origin of the noise is the photodetector only, then the noise variance obviously does not depend on the fibers' distance. However, both the amplitude and the width of the intensity distribution change with the variation of the distance. Indeed, the total power of the light emitted by the fiber is

$$P = \int_{-\infty}^{\infty}\int_{-\infty}^{\infty} A_o e^{-\frac{2(x^2+y^2)}{W^2}} dydx = \frac{\pi A_o W^2}{2} = 2\pi A_0 w^2, \tag{66}$$

where x_o and y_o are the coordinates of the center of the Gaussian intensity distribution; and the width ω increases with the distance as

$$w = \frac{zNA}{2}, \tag{67}$$

where NA is the numerical aperture of the fiber. Therefore, the amplitude

$$A_o = \frac{P}{2\pi w^2} = \frac{2P}{\pi z^2 NA^2}\,. \tag{68}$$

Substituting (67) and (68) into (60), one can find the expression of the lower accuracy bound

$$\sigma_\theta{}^2 \geq \alpha \frac{\pi^2 z^6 NA^6 \sigma^2}{16NP^2}. \tag{69}$$

This Equation indicates that when the number of samples is constant, the samples are kept within optimal ranges (providing the maximum of functions ψ(α) and φ(b), see Equations (49) and (58), as well as other system parameters, remain the same the error may rapidly increase with the increment of the distance between the fibers. This is an important behavior that must be taken into account for the system design.

4.3 3D localization errors

Now that expressions for the minimum variance of the *x* and *y* coordinates have been obtained, the next step is to obtain an expression that will give the variance of the core position P_0 coordinates. According to the expressions in (25) the coordinates of P_0 depend on the parameters *x*, *y*, *z* and ω of two different positions, thus, to obtain the variation of each coordinate of P_0, the variation of each parameter is needed. This issue will be addressed by using the error propagation postulate.

4.3.1 Calculation from error propagation theory

According to the error propagation postulate, the error or variance of a function that depends on *k*-variables can be obtained with:

$$\sigma_f{}^2 = \sum_{i=1}^{k} \left(\frac{\partial f}{\partial x_i}\right)^2 \sigma_{x_i}{}^2, \tag{70}$$

where $\sigma_{x_i}{}^2$ is the variance of the *i*th variable.

By using Equation (70) with the expressions of Equation (25) the following Equations are obtained:

$$\sigma_{x_0}{}^2 = \left[\frac{w_2}{w_2-w_1}\right]^2 \sigma_{x_1}{}^2 + \left[\frac{w_1}{w_2-w_1}\right]^2 \sigma_{x_2}{}^2 + \left[\frac{w_2(x_1-x_2)}{(w_2-w_1)^2}\right]^2 \sigma_{w_1}{}^2 + \left[\frac{w_1(x_1+x_2)}{(w_2-w_1)^2}\right]^2 \sigma_{w_2}{}^2, \tag{71}$$

$$\sigma_{y_0}{}^2 = \left[\frac{w_2}{w_2-w_1}\right]^2 \sigma_{y_1}{}^2 + \left[\frac{w_1}{w_2-w_1}\right]^2 \sigma_{y_2}{}^2 + \left[\frac{w_2(y_1-y_2)}{(w_2-w_1)^2}\right]^2 \sigma_{w_1}{}^2 + \left[\frac{w_1(y_1+y_2)}{(w_2-w_1)^2}\right]^2 \sigma_{w_2}{}^2, \tag{72}$$

$$\sigma_{z_0}{}^2 = \left[\frac{w_2}{w_2-w_1}\right]^2 \sigma_{z_1}{}^2 + \left[\frac{w_1}{w_2-w_1}\right]^2 \sigma_{z_2}{}^2 + \left[\frac{w_2(z_1-x_2)}{(w_2-w_1)^2}\right]^2 \sigma_{w_1}{}^2 + \left[\frac{w_1(x_1+x_2)}{(w_2-w_1)^2}\right]^2 \sigma_{w_2}{}^2, \tag{73}$$

which can be used to calculate the variance of each coordinate of P_0 as wanted.

4.4 Light signal model

In addition to the theoretical errors analysis, a model describing the conversion of the captured optical power into the electric signal might be also useful for evaluation of the system capabilities. For this model, it is assumed that the light emitted by the fiber has a Gaussian intensity profile; hence the wave intensity can be described with the following Equation:

$$I(r,z) = I_o\left(\frac{\omega_o}{W(z)}\right)^2 exp\left(\frac{-2r^2}{W(z)^2}\right), \tag{74}$$

where I_o is the initial intensity, ω_o is the waist radius, $W(z)$ is the beam cross-section radius along the z-axis, and r is the curvature radius. The model follows the diagram shown in Figure 19.

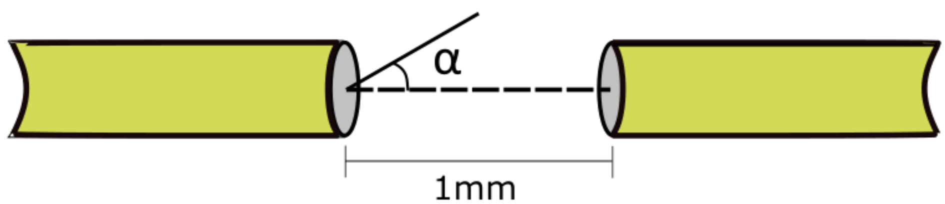

Figure 19. Two fibers with a 1mm distance.

The waist radius ω_o can be known with the next expression.

$$\omega_o = \frac{\lambda}{\pi NA}, \tag{75}$$

where λ is the wavelength, and NA is the numerical aperture. Function $W(z)$ is expressed in the following way:

$$W(z) = \omega_o\sqrt{1+\left(\frac{z}{z_R}\right)^2}, \tag{76}$$

where Z_R is Rayleigh length and is defined as

$$z_R = \frac{\lambda}{\pi NA^2}\,. \tag{77}$$

Substituting Equation (77) in (76) results in:

$$W(z) = \frac{\lambda}{\pi NA}\sqrt{1 + \left(\frac{z\pi NA^2}{\lambda}\right)^2}. \tag{78}$$

The next step is to get an expression for the initial light intensity and another for the power at the second fiber face. The intensity of the light at the first fiber's face is:

$$I(r,0) = I_o exp\left(\frac{-2r^2}{{\omega_o}^2}\right). \tag{79}$$

To obtain the initial power, an integral over the fiber's face must be evaluated. Using polar coordinates makes integration easier:

$$P_o = \int_0^{2\pi}\int_0^{\infty} I_o exp\left(\frac{-2r^2}{{\omega_o}^2}\right) rdrd\theta. \tag{80}$$

Since the Equation does not have angular dependence, the integral can be reduced:

$$P_o = 2\pi I_o \int_0^{\infty} exp\left(\frac{-2r^2}{{\omega_o}^2}\right) rdr. \tag{81}$$

Solving the integral and rearranging terms gives an expression for the initial intensity in terms of the initial power:

$$I_o = \frac{2P_o}{\pi {\omega_o}^2}. \tag{82}$$

To obtain the expression for the power at the second fiber's face the same procedure is followed. The intensity distribution at some distance z can be described by the following expression:

$$I(r,z) = I_o\left(\frac{\omega_o}{W(z)}\right)^2 exp\left(\frac{-2r^2}{W(z)^2}\right). \tag{83}$$

Equation (83) is integrated just like with Equation (79), which results in:

$$P_{in} = \int_0^{2\pi}\int_0^{\infty} I_o\left(\frac{\omega_o}{W(z)}\right)^2 exp\left(\frac{-2r^2}{W(z)^2}\right) rdrd\theta. \tag{84}$$

When the integral in Equation (84) is evaluated, the following expression is obtained:

$$P_{in} = \frac{\pi I_o {\omega_o}^2}{2}\left[1 - exp\left(\frac{-2\rho^2}{W(z)^2}\right)\right]. \tag{85}$$

Substituting Equation (82) into (85) results in:

$$P_{in} = P_o\left[1 - exp\left(\frac{-2\rho^2}{W(z)^2}\right)\right]. \tag{86}$$

Assuming that the nucleus radius is bigger than the waist radius can simplify the Equation by using a Taylor expansion and eliminating non-linear terms:

$$P_{in} \approx \frac{2\rho^2 P_o}{W(z)^2}\,. \tag{87}$$

With the obtained expressions is possible to calculate ω_o, $W(z)$, and P_{in}. By using the characteristics of the photodetectors, the LED, and the fiber it is possible to get a resulting voltage. The laser that is being used has a wavelength of λ = 1.55 µm, the fiber has a numerical aperture of *NA* = 0.14, its radius is of ρ = 8.2 µm, which gives a waist radius of ω_o = 3.52 µm and, for example, at a distance of 1 mm between the fibers $W(z)$ = 144 µm. Having an initial power $P_o = 1$ mW, the power at the second fiber entrance is P_{in} = 7 µW.

With the power entrance, it is possible to calculate the expected signal value by using Equation (82). According to the datasheet for the photodetector PDA400 form Thorlabs, its responsivity is R = 0.95 $\frac{A}{W}$, and the transimpedance for the 20 dB gain setting is $\Omega\ = 1.5 \times 10^5$ V/A. Therefore the expected signal value, calculated from

$$V_{obtained} = R\ \Omega\ P_{in}\ , \tag{88}$$

is of V = 0.997 V that is sufficient for reliable measurements of the light intensity profile.

Chapter 5. Methods and experimental setup

In this chapter, all the details to create the measuring core position system and the methodology for the measurements will be covered. First, an initial system is presented with its components and an explanation of how this system was used. Then the improvements to the system will be addressed, and finally, the measurements methodology will be explained.

5.1 Experimental setup

In this section the main setup will be described in detail together with its components. Furthermore, there will be a description of the light path and how it is captured and processed. The setups used to measure the fiber core position were based on the one showed in Figure 20.

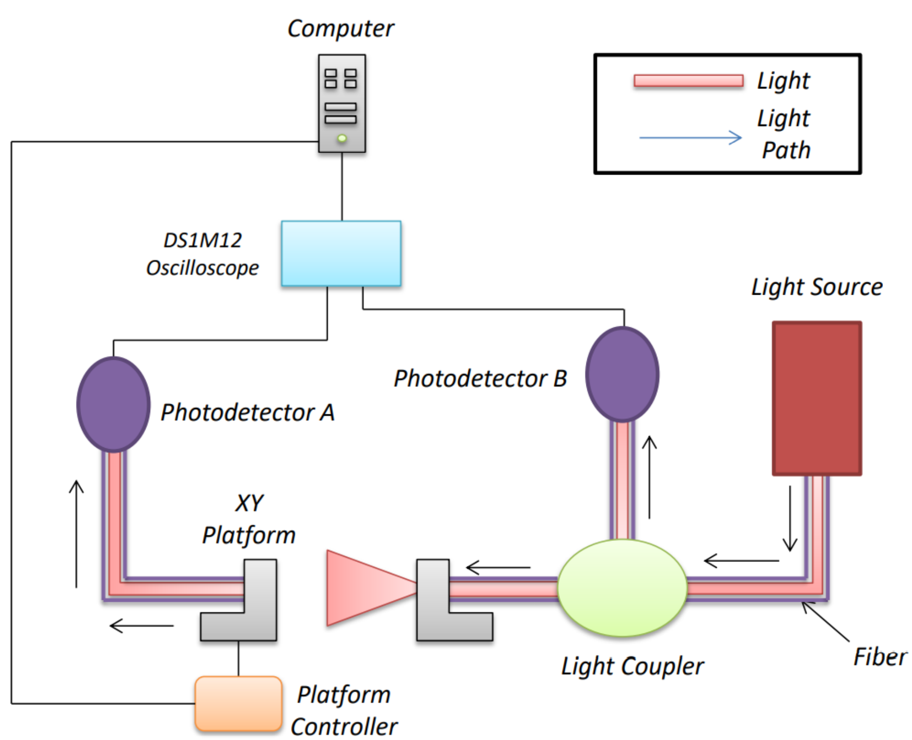

Figure 20. General structure of the experimental setup.

This diagram shows the experimental setup. As it can be seen the system is composed of several components, these will be described in more detail later on. Basically the system uses a light source that sends a modulated signal which is then used to get information of the sample fiber. To do this, the light comes out of the sampling fiber and a probing fiber is then used to capture the coming light, then the light is detected by the photodetectors A and B, where the optical power is converted to an electrical signal. The signal is then sampled and digitalized with the oscilloscope to be processed by the computer. In the course of the data processing the signal coming from the photodetector B is used as a reference in order to eliminate the dark current and reduce the noise influence on the calculated position of the sample fiber.

The light from a source passes through an isolator that prevents the reflected light getting back avoiding the unstable operation of the light source. After this the light passes through the light coupler that divides the optical power into two signals, one with the 40% of the light and the other with the 45% of the light. The signal with the 40% of light goes directly to a photodetector B for reference signal. The signal with the 45% of the light goes to the sample fiber and is then emitted into free space. A small part of the light from the sample fiber is captured with the probe fiber which is connected to another photodetector (photodetector A) which generates an electrical signal that is measured with the oscilloscope channel A. Both photodetectors have integrated amplifiers for better coupling between the photodetectors and the oscilloscope. Finally, the oscilloscope creates digital signal arrays and sends them to the computer. The resulting data is then processed in the computer. Figure 20 shows a diagram that depicts how light travels.

To provide 2D scanning for mapping the light intensity distribution, the ferrule with the probe fiber is installed on a XY-nanopositioner (XY platform) controlled by the computer. The movement along Z-axis for 3D measurements is provided by the translation stage manually controlled by a micrometer head.

5.1.1 Main components

The main components of the system are a light source, an XY nanopositioner, an oscilloscope, two photodetectors, and a light coupler. Down below the characteristics of these components will be described.

5.1.1.1 Light source

In this work two different light sources were used. The first one was an S3FC1550 DFB laser. Its wavelength is 1550 nm, it has a modulation input of 0 to 5 V, and its max power is 2 mW. The light source has an SMF-28e+ fiber connected to its output.

The other light source was an EXS1510₋2111 superluminescent diode (SLED). The SLED light source has a max power of 11.20 mW. It has a spectrum that goes from 1490₋1600 nm approximately and it is centered at 1540.60 nm. The voltage input is of 2.5 V and it is controlled by an EXALOS driver board EBD4000₋0000.

5.1.1.2 Nanopositioner

For 2D scanning with the probe fiber the Attocube ECS3030 nanopositioner was used. The nanopositioner provides travel range of 20 mm with minimum step size of 50 nm, a built-in optical encoder that has a 10 nm resolution with about 20 Hz of sampling rate. The XY platform can be controlled by a computer over an USB connection.

5.1.1.3 Photodetectors

To measure the light signal, two photodetectors were used. Both photodetectors were a PDA400, from ThorLabs. These are InGaAs detectors with the amplifiers providing adjustable transimpedance gain. In this work, the gain was set to 20 dB with a transimpedance of $1.5\text{x}10^5$ V/A.

5.1.1.4 Oscilloscope

To convert the analog signals from the photodetectors to digital format, a DS1M12 “StingRay” oscilloscope form USB Instruments was used. The oscilloscope has two input channels labeled A and B, function generator with single analog signal output and provides USB connection with the computer.

Each input channel has 12 bit ADC resolution and the internal buffer can store up to 8192 samples (8K blocks) per scan in each channel.

5.2 Signal modulation and processing

The modulation of the signal is used to eliminate the contribution of the dark current of the photodetectors and a DC offset which is present at the output of the photodetectors amplifiers even when the light is absent. The known shape of the modulation signals also allows its use as a reference in further signal processing to reduce the influence of the photodetectors and amplifiers noise. As a result, it allows to reduce the uncertainty of the calculated fiber core position.

The oscilloscope built-in function generator was utilized as a source of the modulation signal. Two different type of modulations were used, a saw-tooth and a sinusoidal.

The saw-tooth modulation was used when the light source was the DFB laser. This modulation was needed to decrease interference effects. To modulate the laser optical power, the pump current must change. In semiconductor lasers, this causes that the wavelength of the laser also changes, and in turn, that might reduce the interference effects that may degrade the system accuracy.

The sinusoidal modulation was used for the SLED. The SLED should not have problems with interference, so the reason to use the sinusoidal modulation signal was to obtain a higher RMS in the output signal. The maximum RMS could be reached with a square-wave, however the current controller of the SLED does not support fast signal transitions and to avoid any electrical problem a sinusoidal modulation was used instead.

5.2.1 Signal processing

To understand the processing algorithm it is essential to understand how the data is stored. The program-controlled nanopositioner moves the probing fiber in a range of positions. At each position the signal in every channel was sampled and digitalized by blocks of 8192 samples (8K blocks) at the sampling rate of 500 kHz. The modulation frequency was 488.3 Hz, so that within one 8K block, there were 8 full periods of the modulation signal. This means that for each position the probe is set there will be two 8K blocks.

One important aspect of the modulation is that it eliminates the DC part containing the dark current component and amplifiers offsets; this way, the DC component can be excluded from the signal that simplifies further processing and estimation of the parameters of the Gaussian light intensity distribution. A simple algorithm was used to eliminate the DC component and to demodulate the signal. The demodulation algorithm consists of two steps. First, the AC part of the signal is calculated by subtracting the signal with its mean.

$$s_n(t_k) = S_n(t_k) - \overline{S_n}\ , \tag{89}$$

where $S_n(t_k)$ is the raw signal at time t_k, *n* is a channel index that can be A or B, and $\overline{S_n}$ is the signal mean of a single 8K block of data. Once the DC part of the data is eliminated the following Equation is used to obtain the demodulated signal

$$T_{8KBlock} = \frac{\sum_{k=1}^{N} s_A(t_k) s_B(t_k)}{\sum_{k=1}^{N} s_B(t_k)^2}, \tag{90}$$

where s_A is the signal from channel A without the DC component, and s_B is the B channel signal also without the DC component. Equation (90) provides the estimation of the ratio between the signals in A and B channels according the least squares method (LSM). This expression is used, in fact, to calculate a transmission coefficient for every position of the probe fiber.

5.3 Calculation of the position and width of the Gaussian function

Two types of 2D scans were used in this work. These scans were the cross scan and the equidistant scan within a square, these are represented in Figure 21.

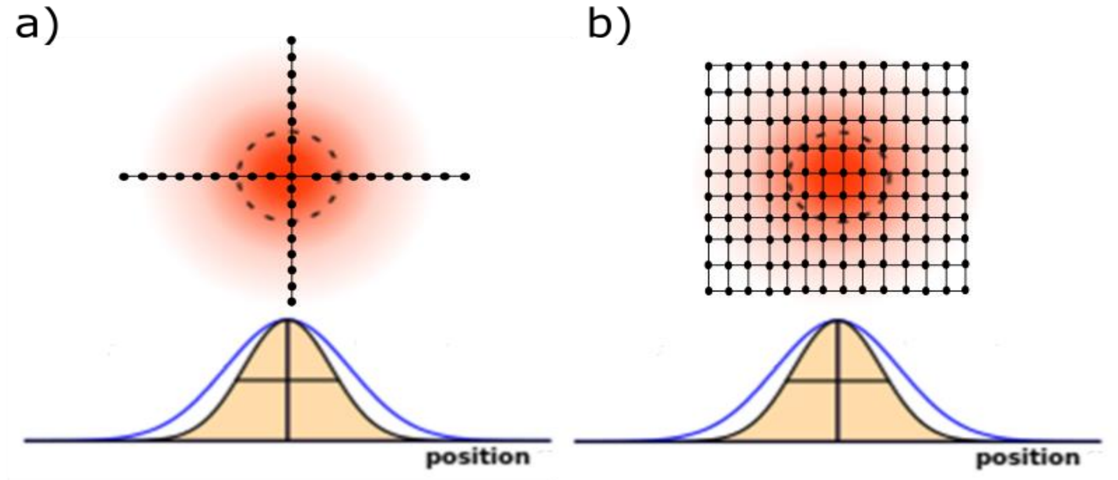

Figure 21. Two different ways of scanning the light intensity (FDominec, 2007), a) represents the cross-like scan and b) the mesh-like scan.

The first experiment with 2D scan that were made with the cross-like scan. This scan consisted in two scans for each measurement: a vertical and a horizontal scan. This kind of scan is equivalent to doing two 1D scans, one for the X axis and another for the Y axis. For this scan a minimum and maximum positions are selected, then the number of positions is set and with this an array of position values is created. The nanopositioner then moves to all the positions in the array along the X axis from the minimum position to the maximum position. The same procedure is repeated for the Y axis and the measured data is then stored in the computer.

For the equidistant scan, first two ranges of values were set, one for the X axis and one for the Y axis. The nanopositioner moves to the minimum value of the X position, for example, if the X axis range is from -200 µm to 200 µm the nanopositioner will start at -200 µm. After the nanopositioner has moved to its respective X position, then it moves the same way along the Y axis. Once the probe is in the desire position the scan starts and moves only in the Y axis. When it finishes scanning the Y axis it comes back to the initial Y position an moves to the next position in the X axis. The process repeats until the nanopositioner reaches the las position, which in this example is (200, 200). Figure 22 shows a diagram of how is this process.

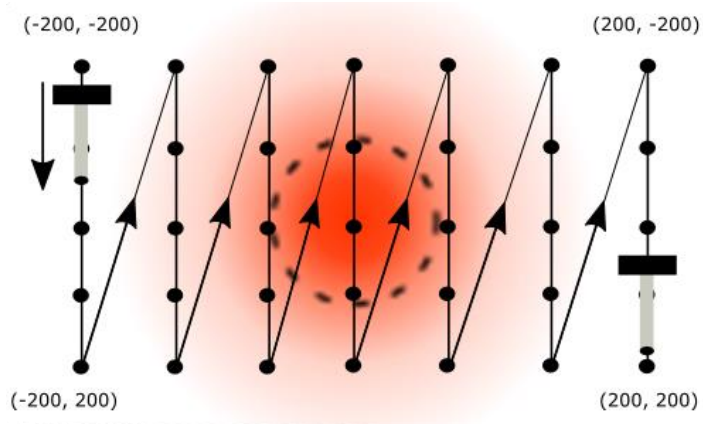

Figure 22. Scanning diagram.

It is important to mention that every time a scan was completed a file was created in the computer and then the system automatically repeated the same scan multiple times until a certain amount of time have passed. The most important results were obtained by doing 3 hrs scans.

The parameters of the Gaussian light intensity distribution were calculated using nonlinear least-square method for every scan, and multiple results have been used to evaluate the statistics for these parameters. These statistical data were used to estimate the repeatability of the measurements and compare the resulting uncertainties with ones predicted by the theoretical analysis.

Chapter 6. Results and discussion

This section will focus on presenting results of the experiments shown in chapter 5. First, this section will start with the cross-like scan. Then some of the results obtained with the Singular Value Decomposition (SVD) will be presented. Next, the equidistant points within a square (mesh-like) scan results will be shown. Finally, the results of the error analysis will be presented.

6.1 Cross-like scans

As mentioned in Chapter 5, this scan is the simplest type of scan that was tested in current experimental configuration. It was performed as a sequence of two 1D scans along *X*- and *Y*- axis. To test the repeatability and stability of the experimental setup, this sequence was repeated multiple times during 1-3 hours. The experimental data for *X*- and *Y*- axis were processed separately, i. e. the parameters of the Gaussian light intensity distribution, amplitude, width and the position of the center, were calculated for every axis. Depending on the distance between the fibers, the scan spans were chosen from ±50 to ±250 µm from the center of the intensity distribution. To test, which direction of the scanning is preferable for every axis, multiple scans forth and back were carried out before choosing the configuration of the cross-like scans.

6.1.1 X-axis scans and parameters estimation

Scans were taken for different periods of time. The chosen periods were 1 and 3 hours, and since the 3 hour scan shows more information only the 3 hour results will be presented. In Chapter 5 it is described how the scanning is made, and during the 3 hours different values for the parameters were obtained. To obtain this parameters a Gaussian function must be fitted; thus for each parameter estimation a Gaussian is obtained, as shown in Figure 23.

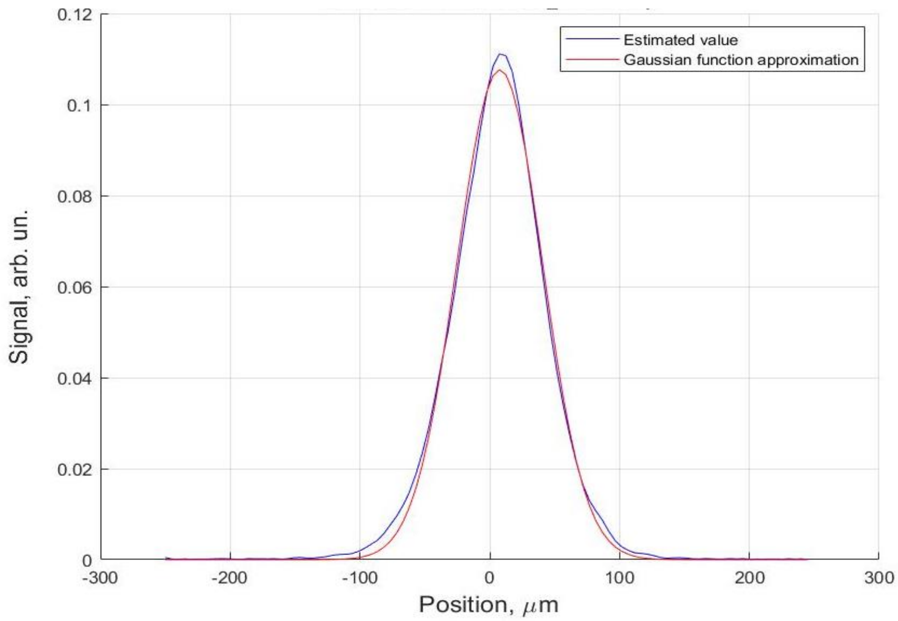

Figure 23. The signal (blue) from a single scan along *X*-axis and its Gaussian fit (red).

The amplitude, position and Gaussian width were estimated for every scan. The variations of these values in time can be seen in Figure 24.

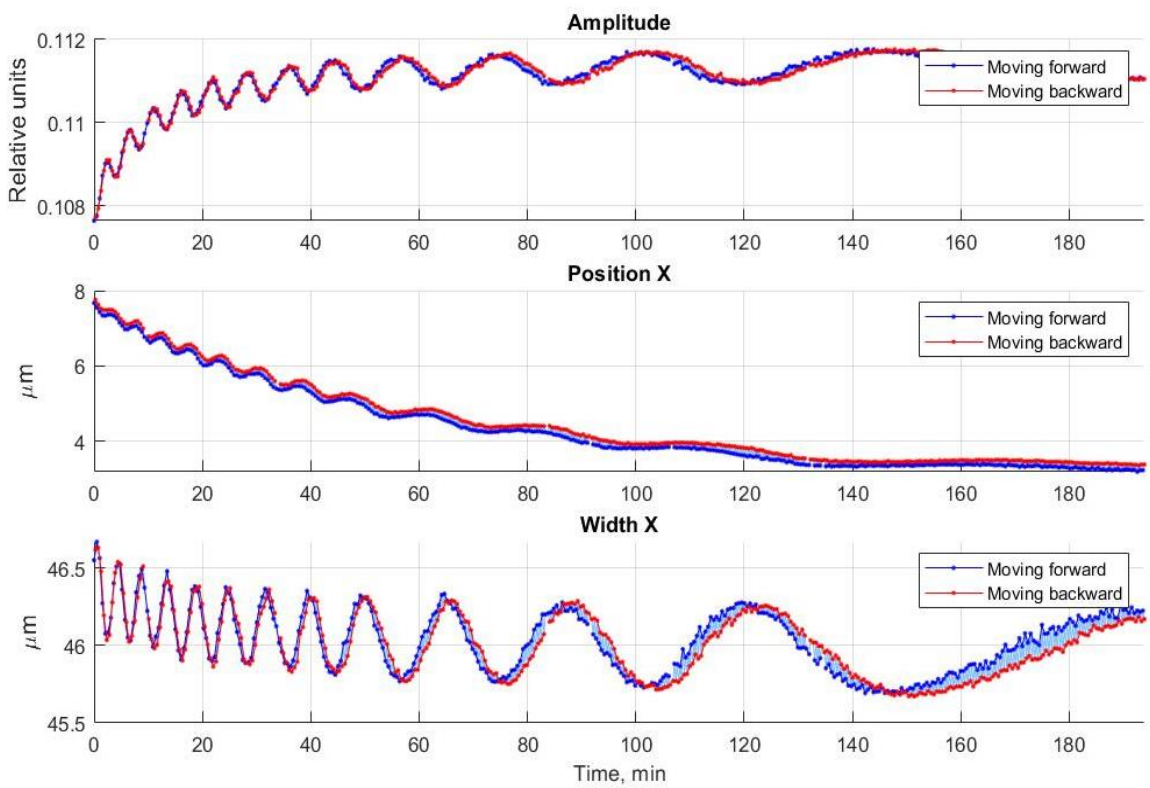

Figure 24. Variations of the estimated parameters of the Gaussian intensity distribution during repeated scans along the X-axis. The parameters were calculated for movements in both directions.

As shown, these variations can be categorized by several easily visible features. First, all parameters demonstrate quasiperiodic oscillations, probably, due to interference effects from coherent laser light. Second feature is a slow, non-periodic drift of the estimated parameters that might be associated with a slow deformation of the mechanical components of the system due to thermal expansion because of change of temperature. Figure 24 shows that the system starts stabilizing after one hour and the oscillations become slower when more time passes.

Third feature is a hysteresis-like effect which appears as a difference in the estimated parameters for scans obtained from forward and backward movements of the probe fiber. This difference can be quite noticeable, for example, as shown in Figure 25, the estimated positions of the center of the Gaussian distribution can differ up to 200 nm.

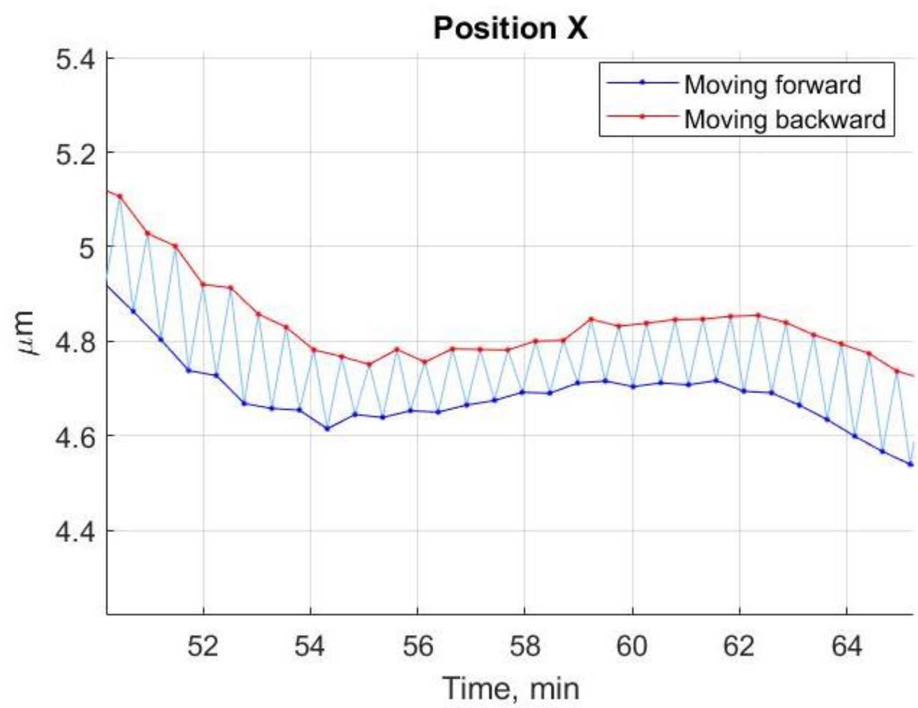

Figure 25. Hysteresis effect in the estimate of the position of the center of the Gaussian light intensity distribution. Blue and red points show the estimated position for scans with forward and backward movements respectively, light cyan lines connect the calculated positions in the same sequence as they were obtained during the experiment, blue, and red lines connect only the position estimates for the same direction of movement.

Finally, fourth feature is the random fluctuations of the parameters estimates calculated for every scanning direction, shown by blue and red lines in Figure 24 and 25. This random variations can be caused by the photodetectors noise, positional errors of the translation stages, and, probably, by some other undefined reasons. These fluctuations can be characterized by commonly known statistical parameters of random variables, like variance or standard deviation, and evaluate to describe the accuracy in terms of uncertainties for this measurement system.

6.1.2 Y axis scan and parameter estimation

Results, obtained during multiple scans along *Y*-axis in both directions are similar to the ones obtained for the *X*-axis. The results of a single scan along the *Y*-axis and its corresponding fit with Gaussian function can be seen in Figure 26.

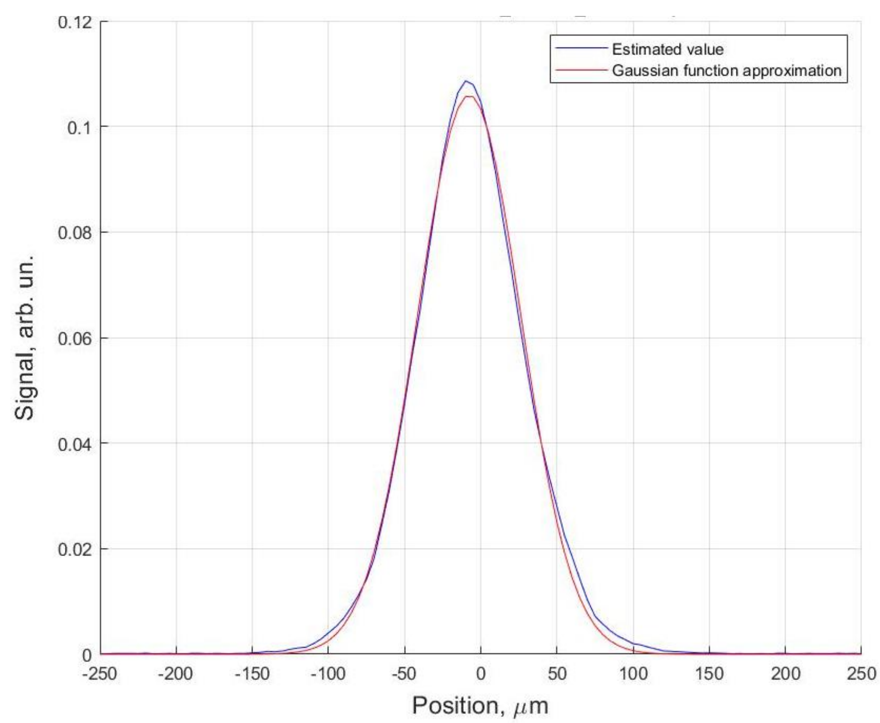

Figure 26. The signal (blue) from a single scan along *Y*-axis and its Gaussian fit (red).

Just as in the scan along the X-axis the amplitude, position and width were estimated for every scan. The variation of these parameters over time can be seen in Figure 27.

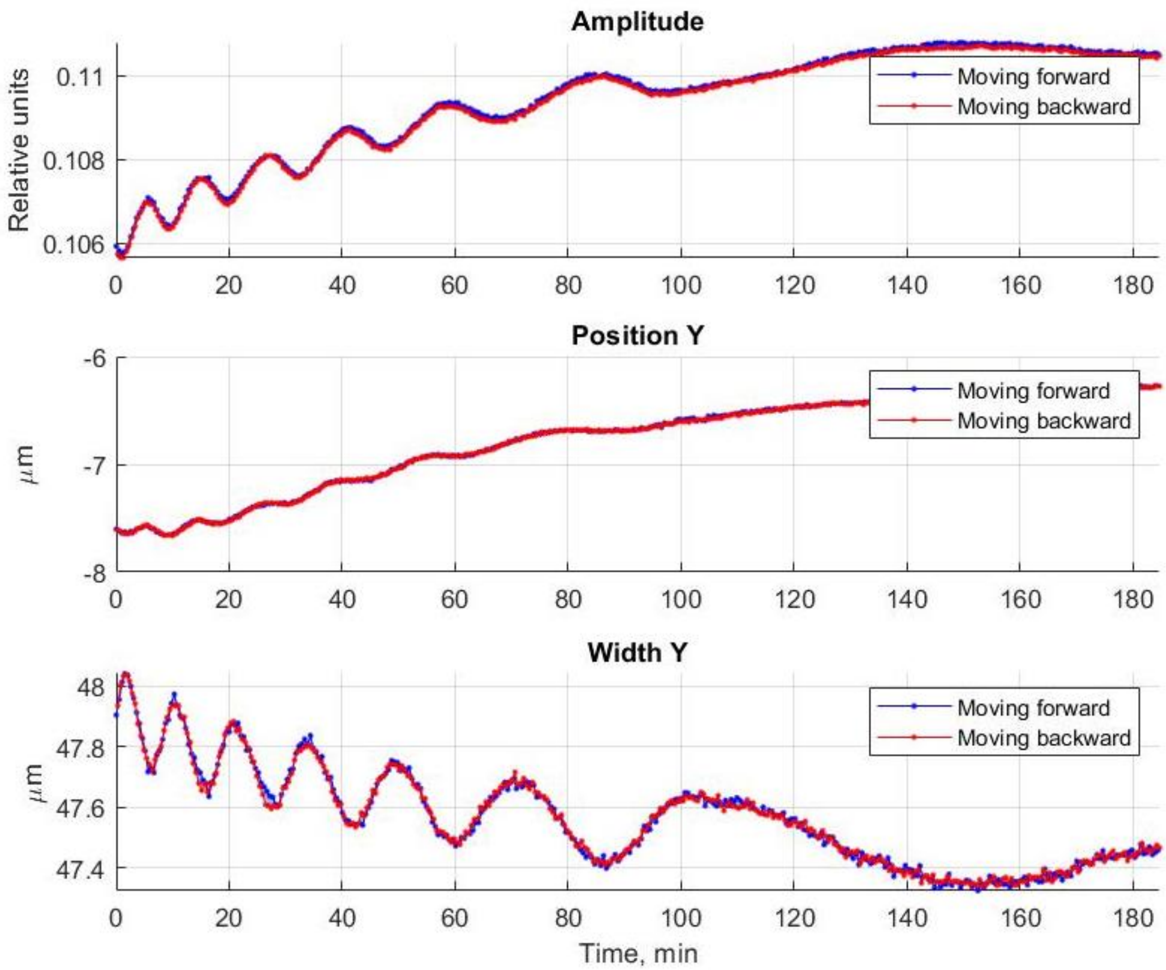

Figure 27. Variations of the estimated parameters of the Gaussian intensity distribution during repeated scans along the *Y*-axis. The parameters were calculated for movements in both directions.

Similar behavior can be seen when comparing the *Y*-axis and the *X*-axis results. Figure 28 show that the *Y*-axis also presents hysteresis. However, its variations are lower than in the case of the scan along the *X*−axis. This difference can be explained by the gravity force that reduces a wobbling in vertical direction.

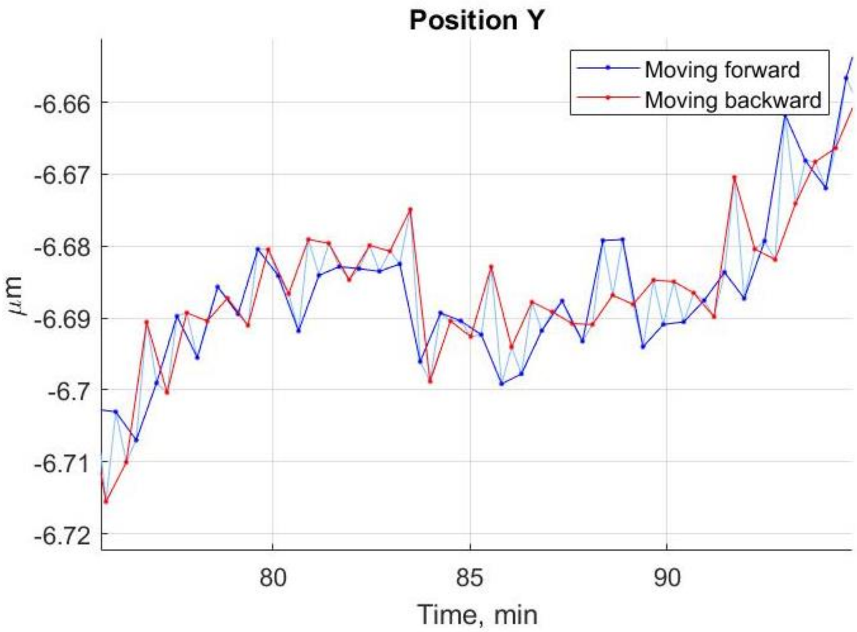

Figure 28. Hysteresis effect in the *Y*-axis. Just as with the X-axis, blue and red points show the estimated position for scans with forward and backward movements respectively, light cyan lines connect the calculated positions in the same sequence as they were obtained during the experiment, blue, and red lines connect only the position estimates for the same direction of movement.

As observed in Figures 27 and 28, the *Y*-axis shares the same features, of the *X*-axis, for the variations. The main difference can be seen directly in the oscillations of Figures 24 and 27. These results show that the *Y*-axis has more stability over time compared to the *X*-axis.

In further experiments with cross- and mesh-like scans, only one direction was chosen for both X- and Y−axis movements: from lower to higher coordinates values. That allowed to avoid the negative impact of the hysteresis effect.

6.1.3 Study of the interference effects using SVD

To investigate the nature of the slow oscillations in the cross-like scans results shown in Figures 24 and 27, the measured signal profiles were represented as matrices and analyzed using Singular Value Decomposition (SVD). This analysis was realized for each axis separately. SVD is a matrix factorization method; Figure 29 shows how it works.

$$\underset{m \times n}{\overset{\hat{X}}{\begin{pmatrix} x_{11} & x_{12} & \cdots & x_{1n} \\ x_{21} & x_{22} & \cdots & \\ \vdots & \vdots & \ddots & \\ x_{m1} & & & x_{mn} \end{pmatrix}}} \approx \underset{m \times r}{\overset{U}{\begin{pmatrix} u_{11} & \cdots & u_{1r} \\ \vdots & \ddots & \\ u_{m1} & & u_{mr} \end{pmatrix}}} \underset{r \times r}{\overset{S}{\begin{pmatrix} s_{11} & 0 & \cdots \\ 0 & \ddots & \\ \vdots & & s_{rr} \end{pmatrix}}} \underset{r \times n}{\overset{V^{\top}}{\begin{pmatrix} v_{11} & \cdots & v_{1n} \\ \vdots & \ddots & \\ v_{r1} & & v_{rn} \end{pmatrix}}}$$

Figure 29. SVD matrix factorization.

SVD establishes that any $m \times n$ matrix can be expressed as three matrices product so that the middle matrix is diagonal. The elements of the diagonal matrix are called singular values.

In this work, the signal values from the measurement are obtained in form of a matrix, like the one shown in Figure 30.

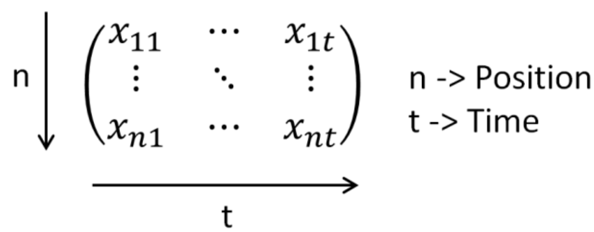

Figure 30. Diagram of how data is stored in a Matrix.

Each column is a scan at a fixed time *t*, so each element of the column is a different position *n*. This matrix is then factorized with SVD into three matrices like in Figure 29, and then their components are studied. To study their components it is convenient to express the initial signal matrix as a function of two variables. Each component of the original matrix can be written as a summation defined by the matrix multiplication between U, S and V. The resulting expression is then

$$x_{n,t} = f(n,t) = \sum_{i=1}^{k} u_i(n) v_i(t), \tag{91}$$

where $u_i(n)$ is a function that gives the corresponding *U* component multiplied by the square root of the corresponding *S* component, in a similar way $v_i(t)$ is a function that gives the corresponding *V* component multiplied by the square root of the same *S* component used in $u_i(n)$. This expression is important to explain the SVD results. Figure 31 show the SVD result for the 3 hrs *X* scan.

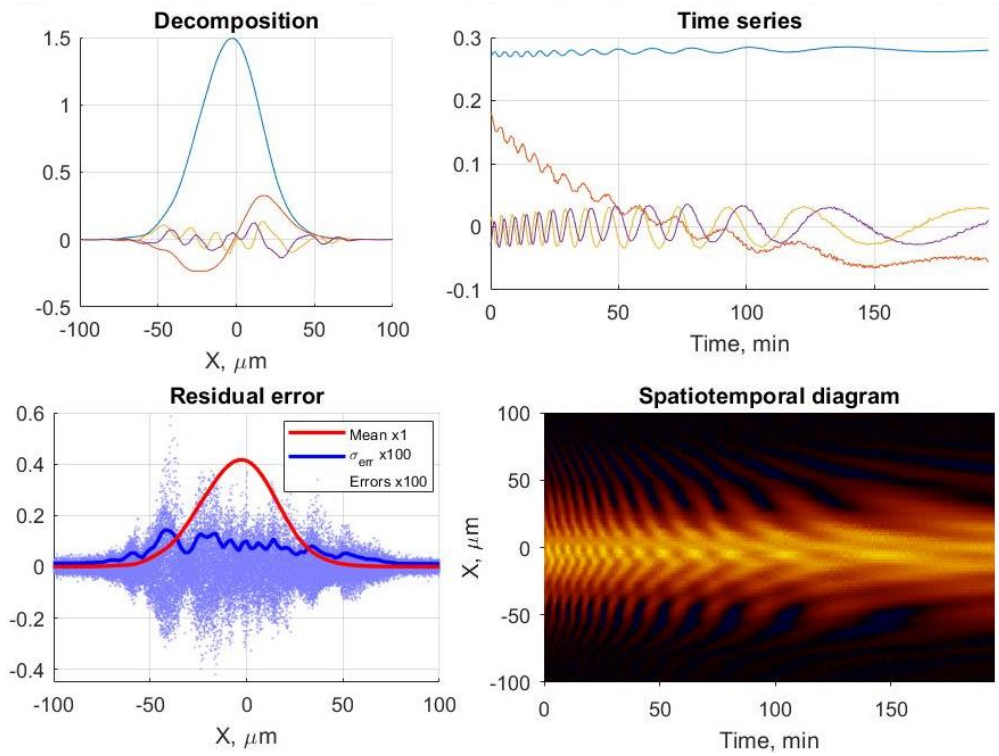

Figure 31. SVD result for the 3hr scan along the X axis. Here there are four different types of plots. The Decomposition plot shows the spatial components $u_i(n)$ and the Times series plot shows the time components $v_i(t)$. The Residual error plot shows the mean value of the signal and the errors which are obtained by subtracting the original signal with a reconstructed signal that is made of the first four components that the SVD provides. The errors are multiplied by x100 to be able to observe them since their contribution is small compared with the signal. The spatiotemporal plot shows the quasi-periodic behavior caused by interference. This is obtained by just using the third and fourth components of the SVD.

As observed there are four plots in Figures 31 and 32 with different curves. The curves in the decomposition plot represent the *i*th's position component of the sum at different positions. In other words, the Gaussian like curve is $u_1(n)$ and the other curves are represented by a different $u_i(n)$ functions. The time series plot is similar to the decomposition plot but instead of using $u_i(n)$, $v_i(t)$ is used. For the residual error a reconstructed signal is created by using the first four of the ith's space and time components. The reconstructed signal is subtracted from the main signal; the result is multiplied by a factor of 100 and then is plotted as the error shown in the plot. The spatiotemporal diagram is obtained by just using the third and fourth components. The important part of this graph is that a pattern is seen. This is typically observed when interference is present.

Figure 32 shows the SVD result for the 3 hrs Y scan.

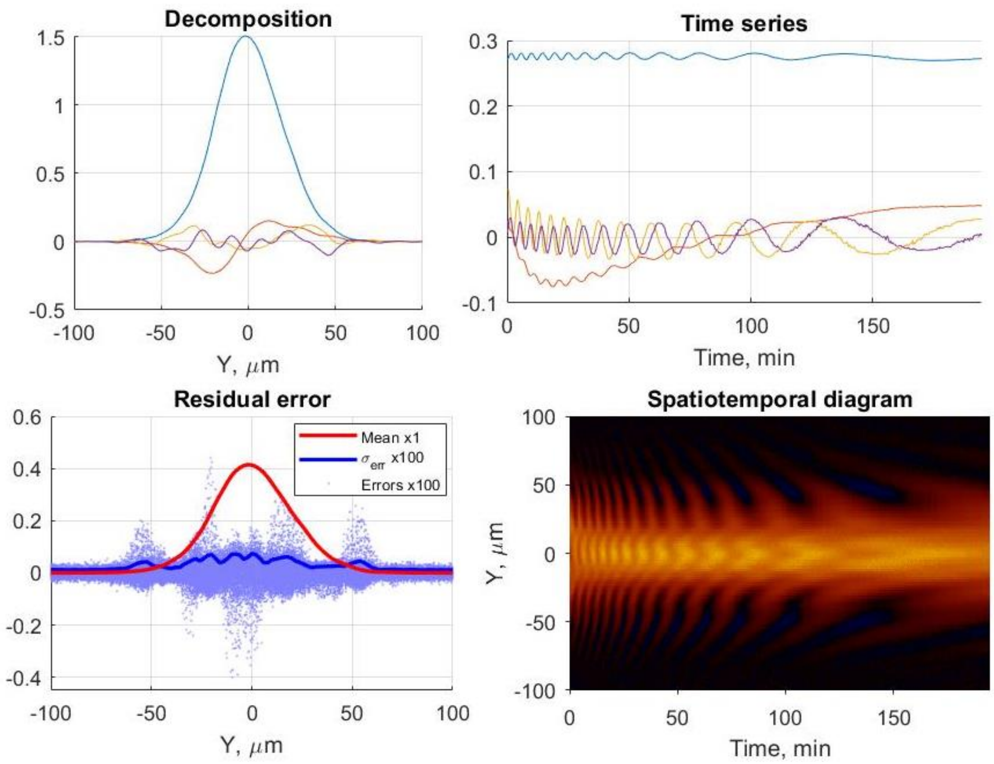

Figure 32. SVD result for the 3hr scan along the Y axis. Here there are four different types of plots. The Decomposition plot shows the spatial components $u_i(n)$ and the Times series plot shows the time components $v_i(t)$. The Residual error plot shows the mean value of the signal and the errors which are obtained by subtracting the original signal with a reconstructed signal that is made of the first four components that the SVD provides. The errors are multiplied by x100 to be able to observe them since their contribution is small compared with the signal. The spatiotemporal plot shows the quasi-periodic behavior caused by interference. This is obtained by just using the third and fourth components of the SVD.

The combination of the SVD, the oscillation behavior of the parameters and the oscillations seen in the mean stability test, is more than enough evidence to show that interference is present. To avoid interference an additional change to the system is made.

6.1.4 Eliminating interference effects using super-luminescent diode (SLED)

In the previous section it is shown that interference is present in the parameter estimation. For this reason an SLED was used instead of a LED laser. The cross-like scan was repeated but with the new light source. The result of a 3 hrs scan for the *x* axis can be seen in Figure 33.

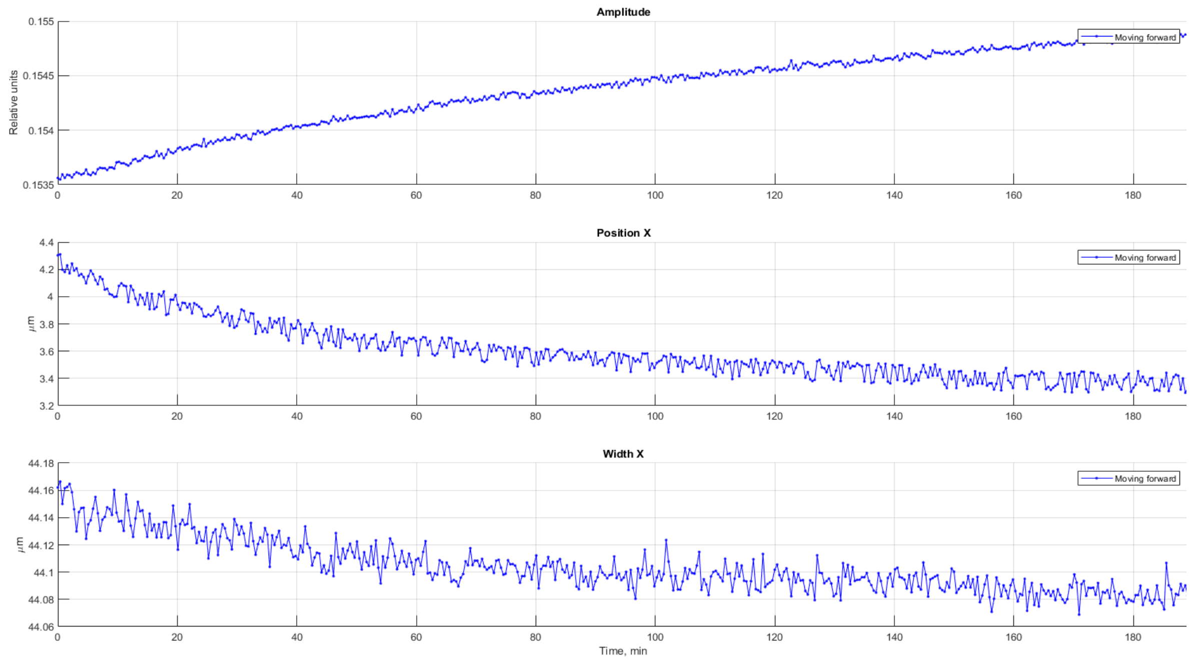

Figure 33. Parameter estimation results from a scan with the SLED for the *X*-axis. The oscillations are no longer present, but there are still random errors and the drift is still present. The estimation of the X-position and the width show a noisy behavior.

Figure 34 shows the result of the *y* axis scan.

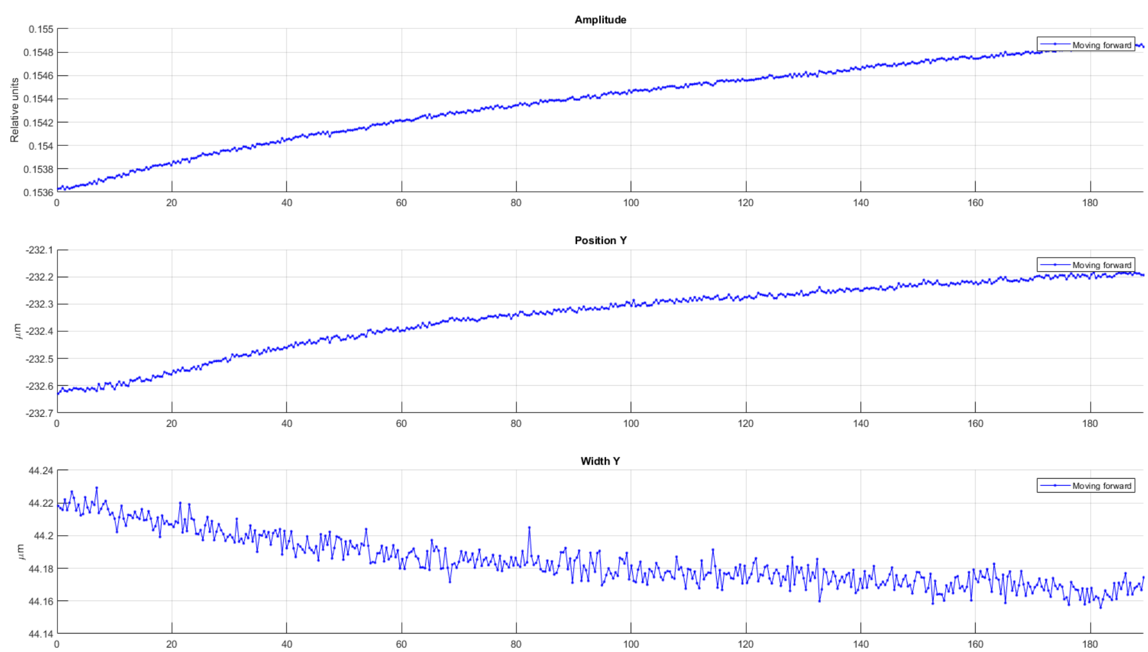

Figure 34. Parameter estimation results from a scan with the SLED for the *Y*-axis. In this case only the width estimation presents a noisy behavior.

Both Figures 33 and 34 shows an improvement in the stability of the parameters since there are no oscillations; however the system still needs a warming time for better results. There is an important difference between the results of the *Y*-axis and the *X*-axis. In the *X*-axis the estimation of the position has more variations than for the *Y*-axis, this could mean that the *Y*-axis present less variations for the estimation of the parameters than the *X*-axis.

The SVD graphs for the *X*-axis can be seen in Figure 35.

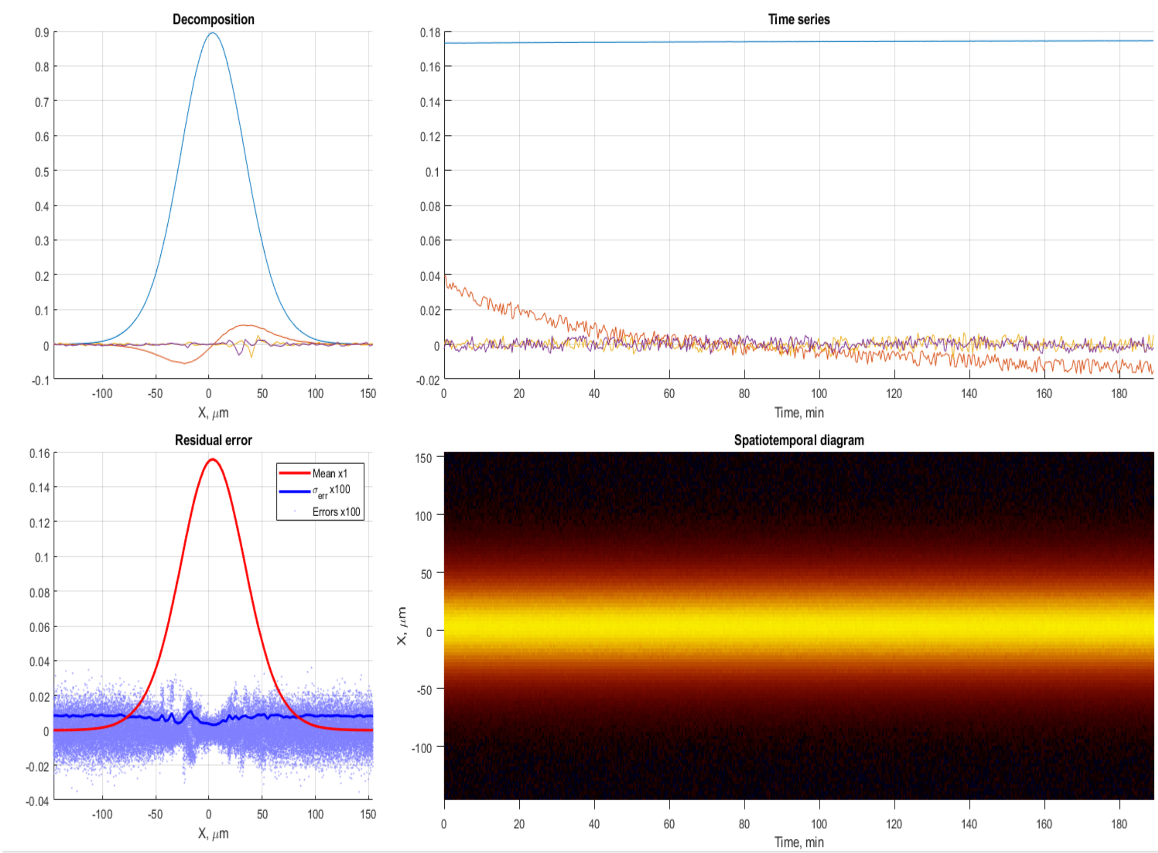

Figure 35. SVD results from a scan with the SLED for the X axis.

The *Y*-axis SVD graphs can be seen in figure 36.

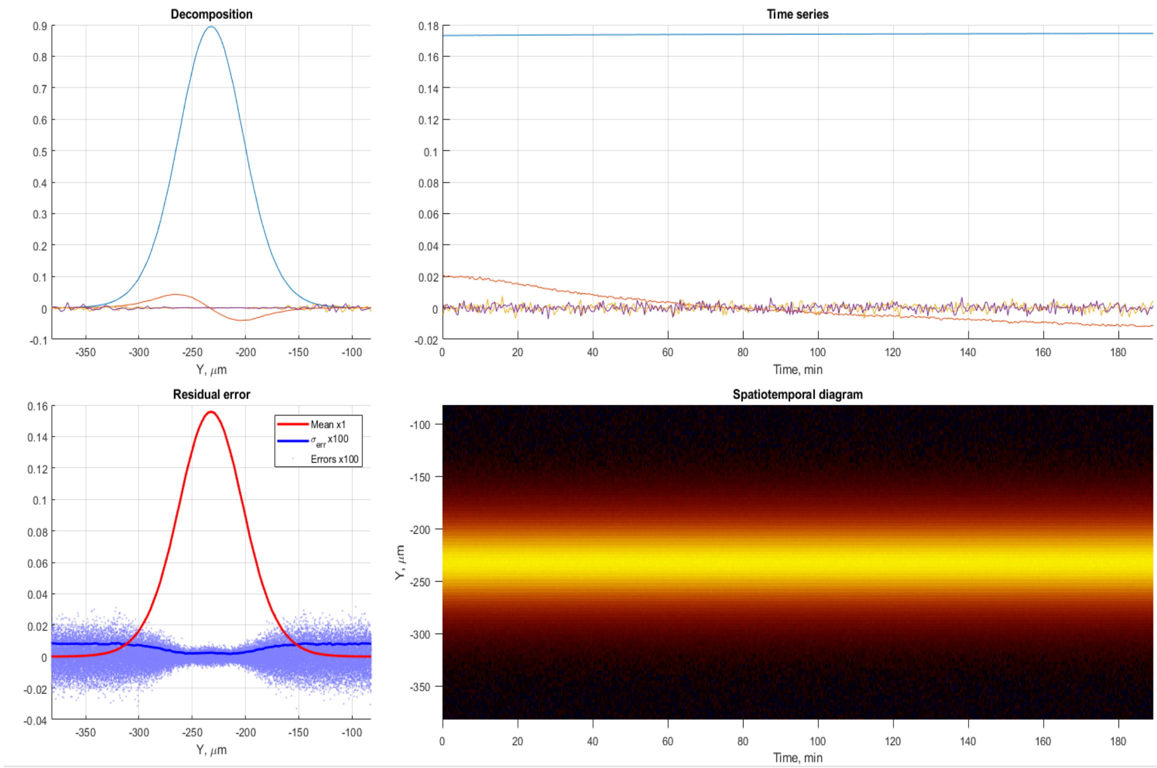

Figure 36. SVD results from a scan with the SLED for the Y axis.

Comparing these results with the laser light results, various differences can be highlighted. First, the Decomposition plot shows that the main component has the highest contribution and the other components are attenuated. In the time series plot, for the SLED, the first component has the greatest contribution to the signal and the others are mostly zero, whereas in the laser case the other components did have a significant contribution. In the residual error, for the SLED, the errors are almost completely attenuated. Finally, the spatiotemporal diagram, in the SLED case, shows a line with a constant intensity through time, something that does not happen in the laser case. Both SVD results, for the SLED, show that interference is not present in the measurements, thus confirming that the signal did have interference for the laser case.

6.2 Equidistant points within a square scan results

Now that the results for the cross-like scan were presented, the results for the equidistant points within a square scan will be shown. The result of the *X* and *Y* coordinates through time obtained with a single scan on a fixed z position can be seen in Figure 37.

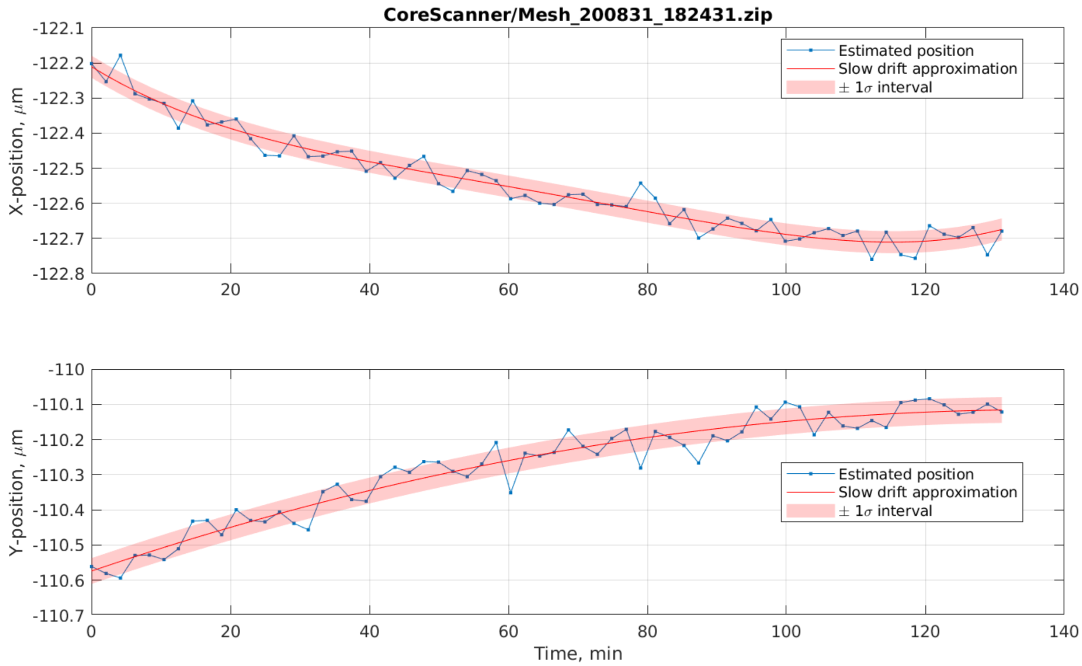

Figure 37. Result of the *X* and *Y* coordinates estimation using the equidistant scan. Here the positions are plotted together with a curve that approximates the slow drift by using a polynomial of degree 4. The interval shown is a 95% confidence interval.

This shows that there is a similar behavior as in the cross-scan. There is a slow drift, thus some time must pass for the system to stabilize. When comparing both the cross-scan and the equidistant points within a square scan, there does not seem to be any difference. However there is indeed a significant difference and this will be more notable when looking at the errors to evaluate the accuracy of the system.

6.3 Systematical and random errors

An analysis of the measurement errors is needed in order to evaluate the system accuracy. The systematic errors for both cross-like and mesh-like scan will be presented and analyzed. Finally, the dependence between the errors and the number of samples will be proven.

6.3.1 Systematic errors for the cross-like scan

Different experiments were made with the cross-like scan. These experiments consisted on doing measurements along the *Z*-axis, and for each *Z*-position the width and the centroid coordinates of the Gaussian were estimated. Figure 38 shows the results for the *x* and *y* coordinates.

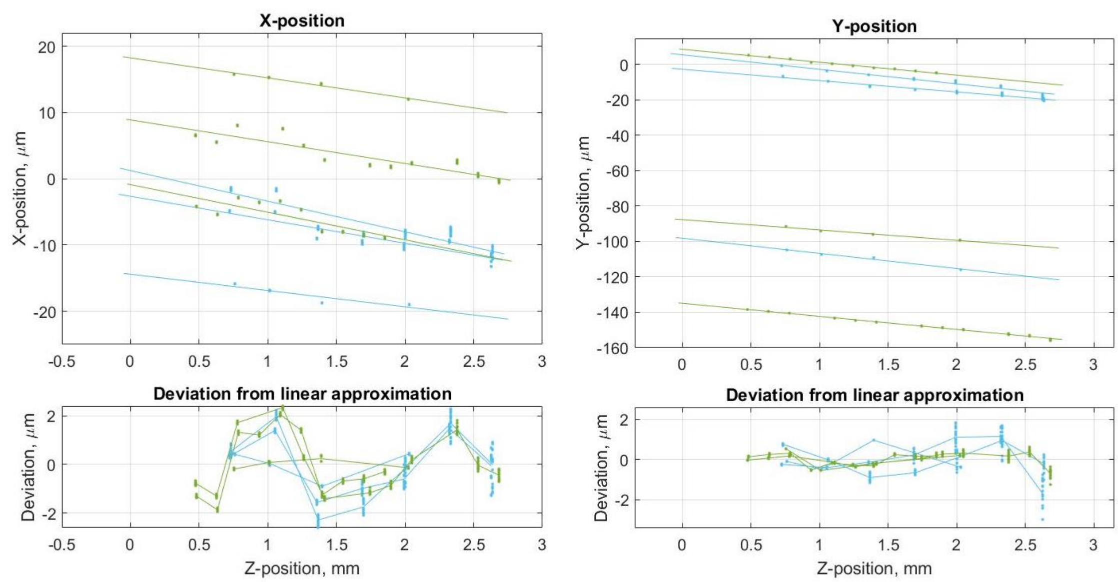

Figure 38. X- and Y- values of the Gaussian centroid on Different *z*-positions and its deviation from a linear fit. Here there are two plots, the first one show points that represent the estimated coordinate at a specific *Z*-position and lines that are linear fits to the estimated coordinates. Each line represents a different experiment. The second plot shows the deviation, from the different experiments, of the estimated coordinate from a line approximation that was made to the estimated parameter.

The results for the width of the Gaussian at different *z*-positions are shown in Figure 39

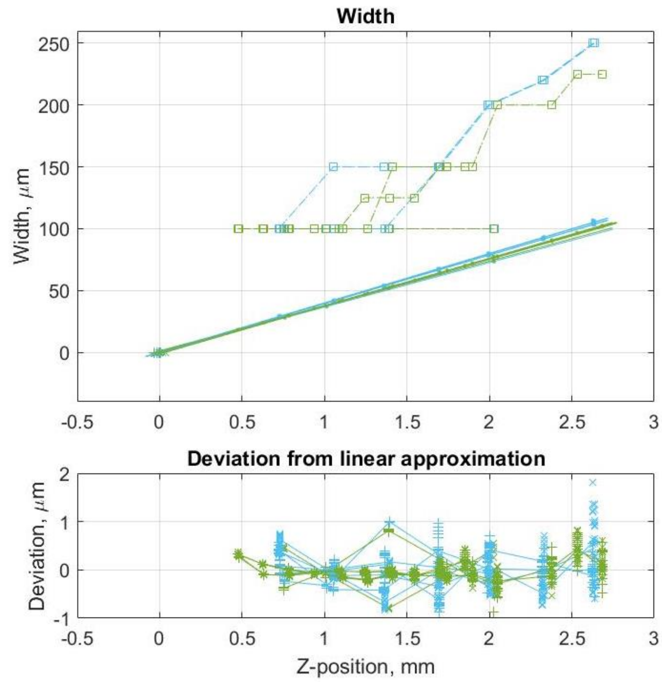

Figure 39. Gaussian width for different z-positions and its deviation from a linear fit. The only difference between this Figure and the previous one is the appearance of dash lines. The dash lines represent the range of the scan.

After evaluating the variations of each parameter it was important to take into account the slow drift that appears in all scans. For this a polynomial fit of degree 4 was used, like in Figure 37, and it was subtracted from the parameters values. Once this was achieved, the standard deviations were evaluated again and a degree 6 polynomial was fitted to the data, like in Figure 40.

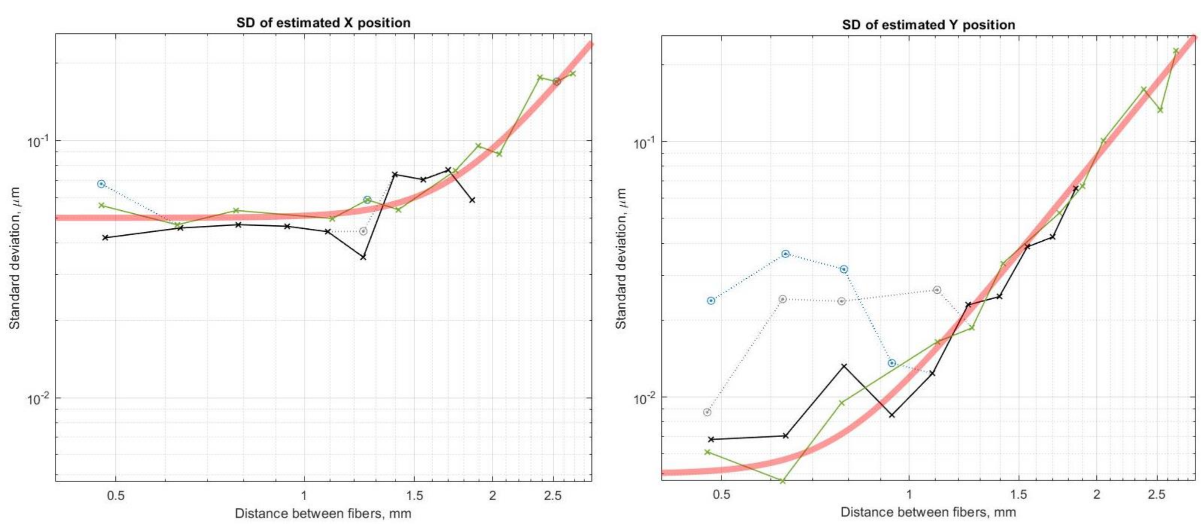

Figure 40. Adjustment of polynomial to deviations of the centroid position for *X* and *Y*-axis. The mechanical variations are 50 nm and 5 nm respectively. The values for the C coefficients are: 9.8 nm^{-4} for the *x*-position, and 10.9 nm^{-4} for the *y*-position.

Figure 40 show the standard deviations at different z-positions for different experiments. The dot lines show the results with the slow drift, the solid lines show the results excluding the slow drift and the transparent thick red line is the fitted curve. Every line represents a different experiment and this results show that different lines are obtained each time. One of the reasons why this happens could be because mechanical components may also change the reference coordinates at different *z*-positions due to imperfections of the translation stage. These types of errors can be compensated by introducing an additional fixed reference fiber.

To understand these results it is important to introduce a term related to the mechanical errors to Equation (60)

$$\sigma_\theta{}^2 \geq \sigma_{MC}{}^2 + \alpha\,\frac{\pi^2 z^6 NA^6 \sigma^2}{NP^2}\,. \tag{92}$$

Here $\sigma_{MC}{}^2$ represents the variation due to the mechanical system used to move the probe fiber. These errors include random errors in the measuring system and the presence of a slow drift that may appear due to effects of thermal expansion or elastic tension and relaxation after any change of the position between consequent scans.

Even though Equation (92) includes the mechanical errors, it might not be enough to represent the errors due to the slow drift. If Equation (92) does not model the error with the slow drift, then it would be convenient to exclude it. As it was mentioned, the drift is eliminated by fitting a polynomial of degree 4 and the result is subtracted from the data. Then Equation (92) is expressed in the following way

$$\sigma_\theta{}^2 \sim B + Cz^6 \tag{93}$$

where $B = \sigma_{MC}{}^2$ and $C = \alpha\frac{\pi^2 NA^6 \sigma^2}{NP^2}$. This expression is useful, because it can be used to model the errors of the estimated parameters. This polynomial is the one used in the fit shown on Figure 40. It can be seen that the fitted curve, for both the *x* and *y* position estimation, models the experimental data very accurately, especially for the results without the drift. The fitting curve gives a mechanical deviation of $\sigma_{MCx} = 50\;nm$ for the *X*-axis and for the *Y*-axis $\sigma_{MCy} = 5\;nm$. It is interesting to see that the *X*-axis has higher mechanical error than the *Y*–axis. This could be due to the way the scan is made and the design of the nanopositioner. When building a translation stage a rail like system must be created, like in Figure 41.

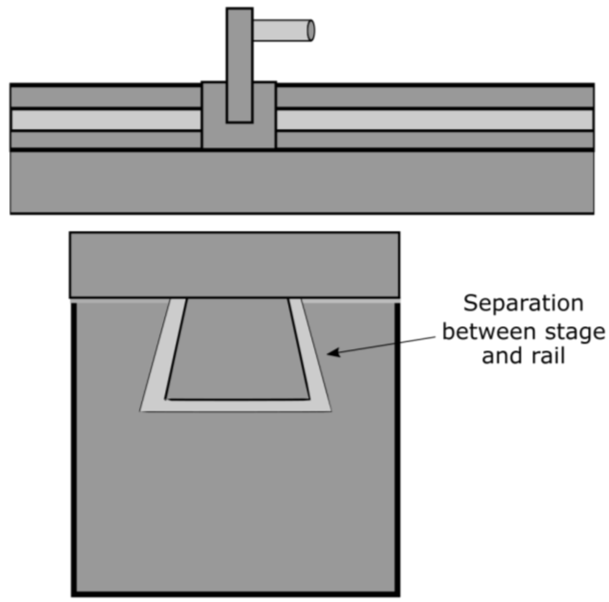

Figure 41. Rail system of a translation stage.

This type of mechanism could be the reason of these differences in variations since the stage could be experiencing an undesired wobbling movement as shown in Figure 42, because of the separation between the stage and the rail.

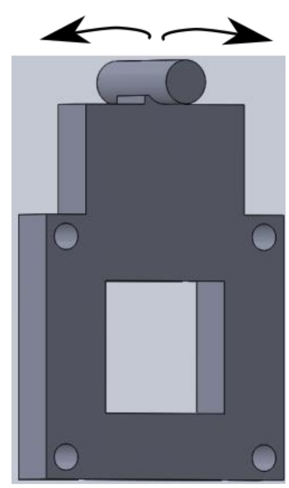

Figure 42. Diagram of the fiber supporter. This is fixed in the stage.

Further analysis for the mechanical error is made but for the mesh-like scan.

6.3.2 Systematic errors for the mesh-like scan

The results for the *X*- and Y-positions for different *Z*-positions for the mesh-like scan are shown in Figure 43.

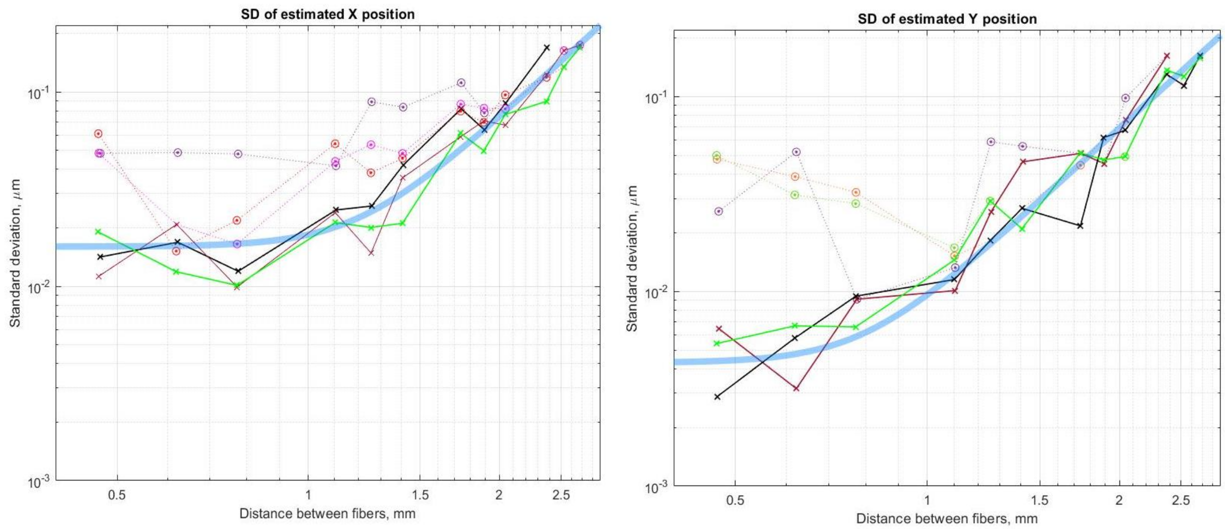

Figure 43. Standard deviations of the coordinate estimates results for the mesh-like scan for the *X*- and *Y*-axis. The mechanical deviations are 16 nm and 4.3 nm respectively. The values for the C coefficients are: 9.2 nm^{-4} for the *x*-position, and 8.6 nm^{-4} for the *y*-position.

Just as with the cross-like scan, the dotted lines represent the standard deviation with the drift, the solid lines represent standard deviation without the drift and the thick blue curve is the fitted polynomial. Comparing Figures 43 and 40 it can be seen that for the *Y*-axis there is a slight improvement in the error, and for the *X* axis there is a considerable improvement. It is more obvious when looking at the mechanical deviations. For the *X*-axis the deviation is $\sigma_{MCx} = 16\ nm$ and $\sigma_{MCy} = 4.3\ nm$ for the *Y*-axis. These results show that the mesh-like scan is a better option than the cross-like scan.

6.3.3 Error dependence with the number of samples

Equation (60) states that the error for the estimation of a parameter is dependent on the number of samples. On the other hand Equation (92) says that the error has an initial value for *z* = 0, but for bigger *z* the constant term is negligible and Equation (60) gives a good approximation. To check these statements, two experiments were realized. The first experiment consisted in estimating the coordinates of the centroid with a distance of ≈2 mm from the sample fiber. In this case the number of samples was changed instead of varying the *Z*-position. The result of the standard deviation can be seen in Figure 44.

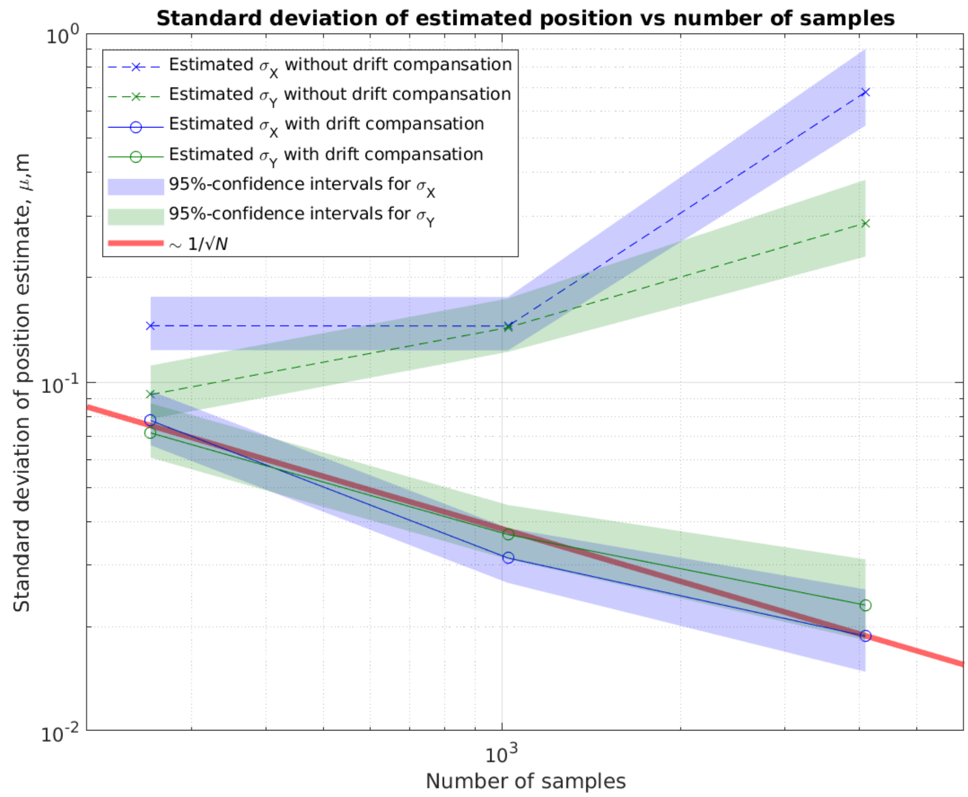

Figure 44. Plot showing the relation between the number of samples and the standard deviation for a distance of 2 mm.

As it can be seen there are two types of results, the pointed lines show the result for the X and Y coordinate deviations considering the drift and the solid line shows the result without the drift. It is clear that the deviation without the drift is proportional to $\frac{1}{\sqrt{N}}$ which agrees with Equation (60), which is valid for large *z*.

The next step is to try a smaller value of z in order to check the validity of Equation (92). The second experiment consisted on evaluating the coordinates for different samples but at a distance of ≈1 mm. The results of such measurement can be seen in Figure 45.

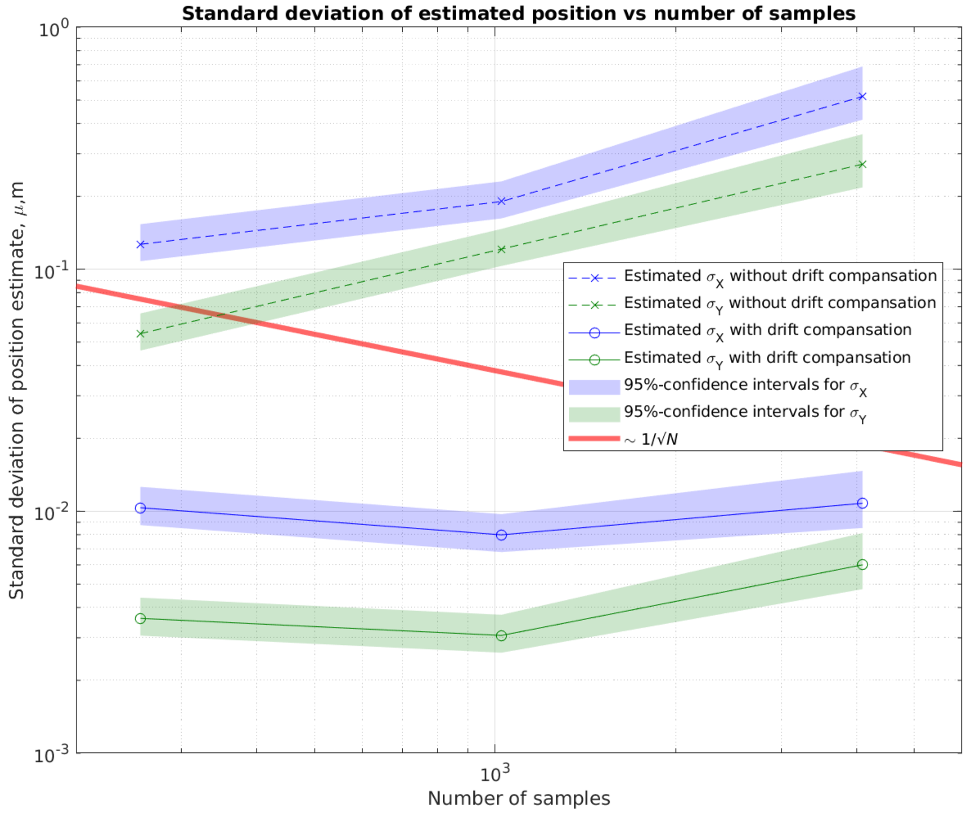

Figure 45. Relation between the number of samples and the standard deviation for a distance of 1 mm.

Figure 45 shows that there is no visible relation between the number of samples and the standard deviation. This is logical since, according to Equation (92), at shorter distances the deviation due to the mechanical components dominates over the distance variation.

These two results prove what Equations (60) and (92) state and also demonstrate the dependence between the error and the number of samples for large z-positions.

Chapter 7. Conclusions and recommendations

In this work, a system capable of measuring the position of a fiber core was built. The system has accuracy between 50 and 100 nm, with the possibility of enhancing it. The system was analyzed theoretically and studied experimentally.

As follows from the theoretical analysis, the coordinates of the fiber core in 3D space can be found by measuring the centers and widths of that light distribution within at least two separate planes nearly perpendicular to the fiber optical axis.

The accuracy of the coordinates estimation was also analyzed theoretically using Cramer-Rao lower bounds evaluation, assuming that the main source of errors is the photodetector noise. As was found, the noise-limited uncertainty of the estimation of the center of the light intensity distribution, as well as of its width, rapidly grows with the increase of the distance between the sample and probe fibers.

The equations elaborated in this analysis can be used, on the one hand, for the evaluation of the accuracy of future systems for similar measurements, and, on the other hand, for the determination of the requirements for the system components, like the optical power of the light source, photodetector noise and responsivity, the required amount of samples to measure the light intensity distribution, etc. The validity of these equations was successfully verified in the experimental study by varying the distance between the fibers, and the number of samples for mapping the intensity distribution.

Both the theoretical and experimental study show that in order to calculate the central position of the 100-microns-wide light intensity distribution with the uncertainty less than 100 nm, it is sufficient to scan and sample this light distribution in a grid of just 16x16 points separated by 10-20 microns. To achieve this accuracy, the signal-to-noise ratio during such sampling must be 40-50 dB or higher.

The experiments were conducted with both coherent and incoherent light sources. The light from coherent source, DFB laser, produced too high level of noise in the recorded intensity distribution due to the interference effects. That led to large errors in the estimation of the distribution parameters: width and center position. To avoid this kind of inaccuracy, the laser was replaced by super-luminescent diode (SLED) with wide radiation bandwidth. This allowed to suppress the interference noise and greatly improve the measurement accuracy.

In general, the study has demonstrated the feasibility of the system for accurate measurement of the fiber core position of by mapping the intensity distribution of light from the sample fiber by scanning this distribution with a probe fiber mounted on the computerized translation stage. Nevertheless, it is necessary to note that while the optoelectronic components provide the required signal-to-noise ratio, and the developed algorithms for signal processing and coordinate calculations yield the needed accuracy, to keep the required precision, the mechanical elements of the system, like optical mounts, translation stages and nanopositioners must be carefully selected from those available on the market that are specially designed for high precision applications.

Experimental results obtained during this work reveal an uncontrollable slow drift in the calculated intensity distribution parameters that might be a sign of the slow thermal expansion of the mechanical components of the system due to a change of the environmental temperature. During the experimental data processing, in order to evaluate the noise-limited uncertainty from random fluctuations in the estimated parameters, this slow drift was compensated by subtracting smooth polynomial approximation of this drift. However, in real application such compensation is not possible. Therefore, to avoid thermal expansion effects in such measurements, the mechanical part of the system must be located in temperature stabilized enclosure.

Both the algorithm and the theoretical results can be used in different setups, for example one that uses a CCD instead of the probing fiber.

For the system presented in this work, the recommendations to obtain the best accuracy are using a mesh-like scan, an incoherent light source, and a temperature stabilized environment that eliminates the slow drift in the estimated parameters.

Bibliography

Andrew M Kowalevicz Jr and Frank Bucholtz. 2006. Beam divergence from an SMF-28 optical fiber. Technical report, naval research lab Washington DC.

Arden photonics. 2020. FGC-GA Geometry system. Consulted https://www.ardenphotonics.com/products/fgc-ga-array-geometry-system/

Attocube. 2011. User manual attocube systems EcoSmart drives (Version 1.0）. 2.

Betham, D. 2020. Precision versus accuracy. Accurate measurements fall in the bulls eye. Precise measurements are tightly clustered. Accurate and precise measurements are tightly clustered in the bulls eye! Consulted April 29, 2021. Consulted http://www.antarcticglaciers.org/glacial-geology/dating-glacial-sediments-2/precision-and-accuracy-glacial-geology/

Casas, J. R., Cruz, P. J. S. 2003. Fiber optic sensors for bridge monitoring. Journal of bridge engineering, 8(6), 362–373. doi:10.1061/(asce)1084-0702(2003)8:6(362)

Culshaw, B. 2000. Fiber optics in sensing and measurement. IEEE Journal on Selected Topics in Quantum Electronics, 6(6), 1014–1021. doi:10.1109/2944.902150

FDominec. 2007. Intensity and E-amplitude profile of a Gaussian laser beam. Consulted April 29, 2021. Consulted https://commons.wikimedia.org/wiki/File:Laser_gaussian_profile.svg

Fehlberg, E. 1970. Introduction. In some experimental results concerning the error propagation in Runge-Kutta type integration formulas. NASA. pp. 1–5.

Gloge, D. Offset and tilt loss in optical fiber splices. 1976. The Bell system technical journal, 55(7):905–916.

Cramér, H. 1946. Mathematical methods of statistics. Princeton University Press, Princeton, N. J.

Hansen, P. C., Pereyra, V., Scherer, G. 2013. Non linear least squares problems. In least squares data fitting with applications. The Johns Hopkins University press. pp. 147–190.

Harstead, E., Sharpe, R. 2012. Future fiber-to-the-home bandwidth demands favor time division multiplexing passive optical networks. IEEE communications magazine, 50(11), 218–223. doi:10.1109/MCOM.2012.6353704

He, L., Zhang, M., Shams-Ansari, A., Zhu, R., Wang, C., Loncar, M. 2019. Low-loss fiber-to-chip interface for lithium niobate photonic integrated circuits. ArXiv, 44(9), 2314–2317. doi:10.1364/ol.44.002314

Hsu, S. W., Jiaan, Y. D., Huang, M. S. 2005. Measurement of core position of fiber array by a calibrated mask method. Key engineering materials, 295–296, 227–232. doi:10.4028/www.scientific.net/kem.295-296.227

Idachaba, F., Ike, D. U., Hope, O. 2014. Future trends in fiber optics communication. Lecture Notes in Engineering and Computer Science, 1(August), 438–442. doi:10.33564/ijeast.2020.v04i10.038

Kato, S., Fujiwara, K., Ohta, T., Tanaka, T. 2010. Reference MPO connectors with pre-angled MT ferrules and measurements of fiber core position. Optics infobase conference papers, 10–12. doi:10.1364/nfoec.2010.jtha62

Li, L., Guo, F. 2010. Analysis on the Gaussian approximation for the far-field of optical fiber. Optoelectronic devices and integration III, 7847(1), 78471W. doi:10.1117/12.868764

Mathematica. 2021. Friction models. Consulted April 29, 2021. Consulted https://www.wolfram.com/mathematica/new-in-9/advanced-hybrid-and-differential-algebraic-equations/friction-models.html

Montgomery, J. D., DeCusatis, C. 2002. History of fiber optics. In fiber optic data communication: technology advances and futures. Academic Press. pp. 9–22.

National electrical contractors association. 2016. Standard for install and testing fiber optics. National electrical contractors association.

Nicolaisen, E. and Danielsen, P. 1983. Calculated and measured spot size of equivalent Gaussian field in singlemode optical fibres. Electronics Letters, 19(1):27–29.

Ozawa, K., Ogawa, S., Ishida, H., Hattori, Y. 1995. High-speed measuring equipment of fiber core position of optical fiber array using piezo actuator. Proceedings - IEEE international conference on robotics and automation, 1, 672–678. doi:10.1109/robot.1995.525361

Qing, X., Li, W., Wang, Y., Sun, H. 2019. Piezoelectric transducer-based structural health monitoring for aircraft applications. Sensors (Switzerland), 19(3), 1–27. doi:10.3390/s19030545

Salehh, B. E. A., Teich, M. C. 1991. Beam optics. Fundamentals of photonics. doi: 10.1002/0471213748.ch3

Salehh, B. E. A., Teich, M. C. 1991. Fiber optics. Fundamentals of photonics. doi: 10.1002/0471213748.ch8

Salehh, B. E. A., Teich, M. C. 1991. Photon optics. Fundamentals of photonics. doi: 10.1002/0471213748.ch11

Sataloff, R. T., Johns, M. M., Kost, K. M. 2013. Detection, estimation, modulation theory (Part 1 - Detection, estimation and filtering theory) (2nd ed.). Wiley. pp. 1-16

Suhir, Ephraim. 2000. Microelectronics and Photonics-the Future. 22nd International conference on microelectronics, Vol 1.

Sutherland, J., George, G., and Krusius, J. P. 1995. Optical coupling and alignment tolerances in optoelectronic array interface assemblies. In 1995 Proceedings. 45th Electronic components and technology conference, pages 577–583.

Yagishitagiken. 2020. V-groove board, fiber array inspection machine (YGN-590-FAVG). Consulted http://www.imageprocessing-yagishita.com/en/24/

Appendix

This section will deal with extra details about the measuring system and some preliminary experiments with their corresponding results. This information is not necessary to understand the manuscript, but it is helpful for a better understanding of the measuring system.

Initial setup

In chapter 5 there is a diagram (Figure 20) showing the general structure of the experimental setup. It is also mention that two light sources were used: an S3FC1550 DFB laser and a SLED. The first light source was included in the initial setup, which is presented in the Figure below.

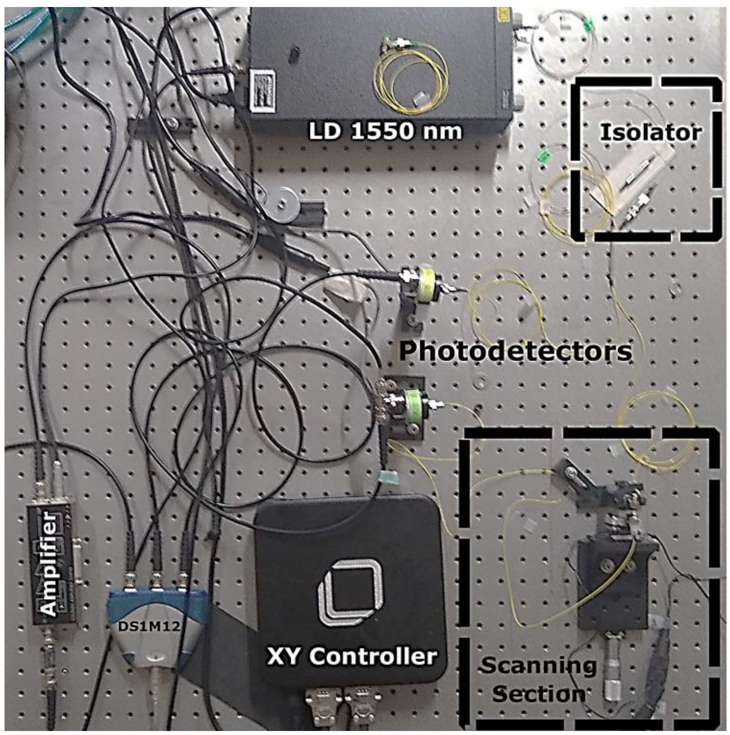

Figure 46. Initial setup.

Compared to the diagram in Figure 20, in this case there is an isolator and an amplifier; the amplifier has an attenuator included. In this particular setup these additional components were needed. The isolator was necessary to avoid laser reflections which could provoke a malfunction in the light source. The amplifier with the attenuator was necessary to avoid overexposure from the modulation, for this;

first the single is attenuated and then amplified. It is important to mention that the modulated input of the light source came from the oscilloscope function generator.

SLED setup

The other setup used the SLED as the light source. The driver with the SLED can be seen in Figure 47.

Figure 47. SLED in its driver.

The resulting setup can be seen in Figure 48.

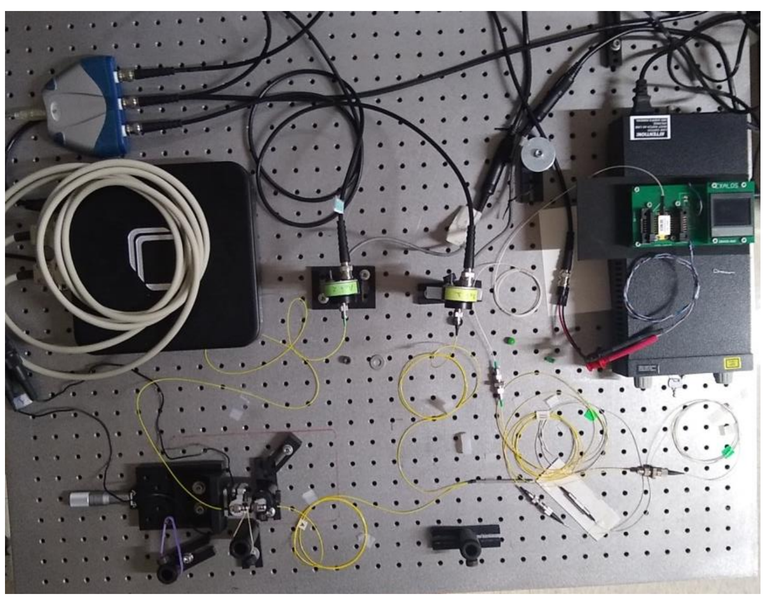

Figure 48. Second setup.

In this case an amplifier was not necessary, since the intensity of the modulated signal was suitable. There are not many differences between the two setups, but as seen in Chapter 5 and 6 these changes were necessary for a better measurement.

Now that the used setups were described, it is important to talk in more detail about the nanopositioner.

Nanopositioner

One of the most important components of the measuring system is the nanopositioner. Knowing the dynamics is important because it gives information about its limitations. Before the construction of the measuring system, some experiments were realized to characterize the nanopositioner.

The characterization of the nanopositioner consisted in varying parameters to see the motion of the stage. This is important because this way it is possible to see if the movement follows a linear or non−linear relation, among other important information about the apparatus. Figure 49 shows a plot of position vs. time.

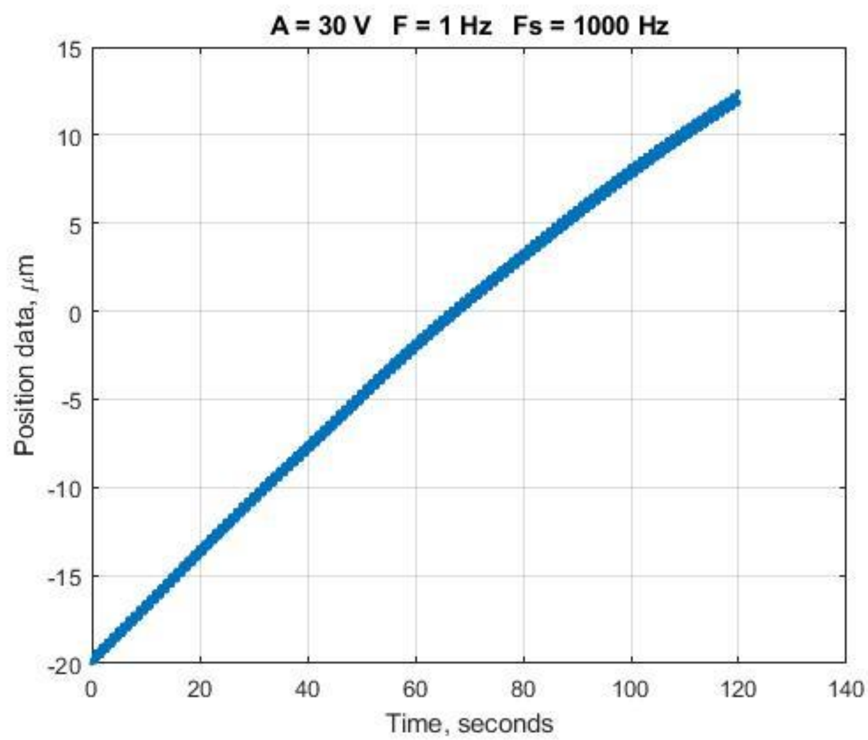

Figure 49. Position vs. time at 30 V.

As can be seen, the positioner's motion for this case is clearly not linear, but if a voltage of 45 V is set, the result is the following.

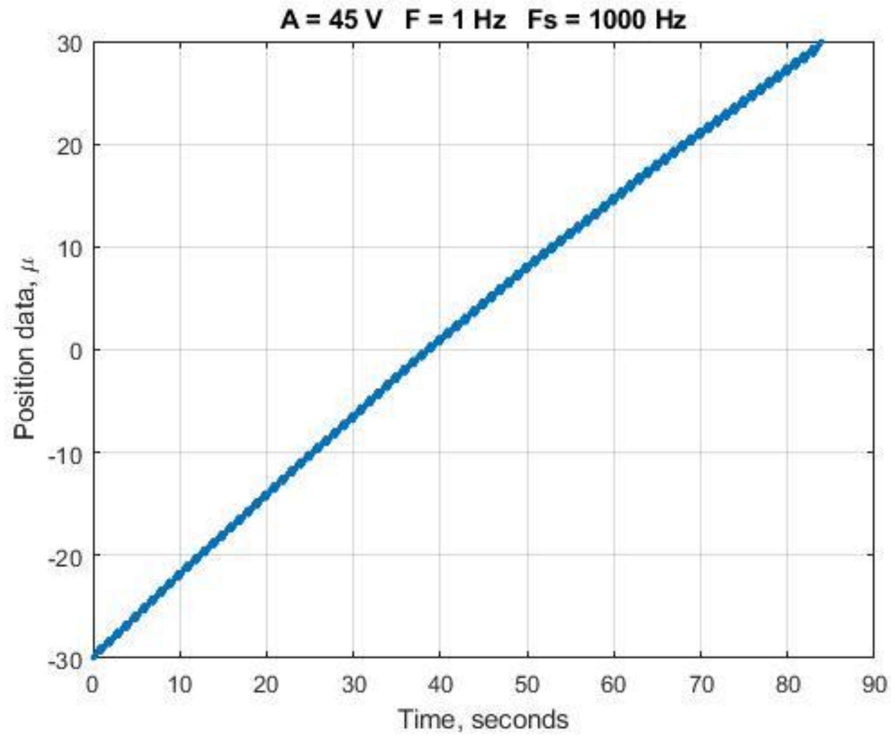

Figure 50. Position vs. time at 45 V.

It is still not linear, but qualitatively it looks less curved compared to the 30V case. Aside from the non−linearity, the plot gives two important observations. First is the stick-slip phenomenon, this can be appreciated in Figure 6 which shows a zoom in on Figure 4.

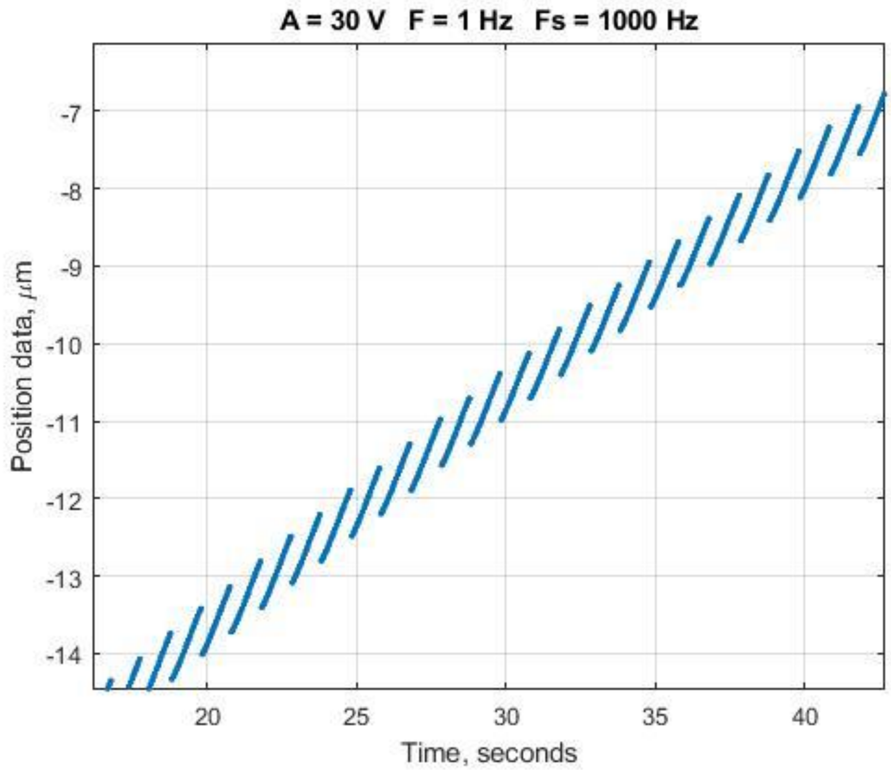

Figure 51. First zoom in over the position vs. time plot.

To understand what is happening it is important to explain how the nanopositioner works. The nanopositioner is based on stick-slip phenomena. Stick-slip is a friction phenomenon where an object and a surface interact. Friction is stronger when the object is static and weaker when it is moving. This is exploitable in an oscillating system, for example, with a spring, just like in Figure 52.

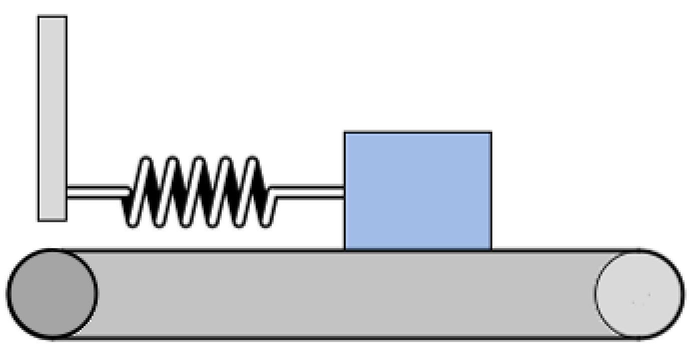

Figure 52. Stick-slip system (Mathematica, 2021).

The moving surface moves the object thanks to the frictional force. Once the object gets to a certain position, the force due to the spring pulls it back to the initial position. The nanopositioner functions similarly by using a piezoelectric. Figure 8 shows a diagram of the nanopositioner stick-slip system.

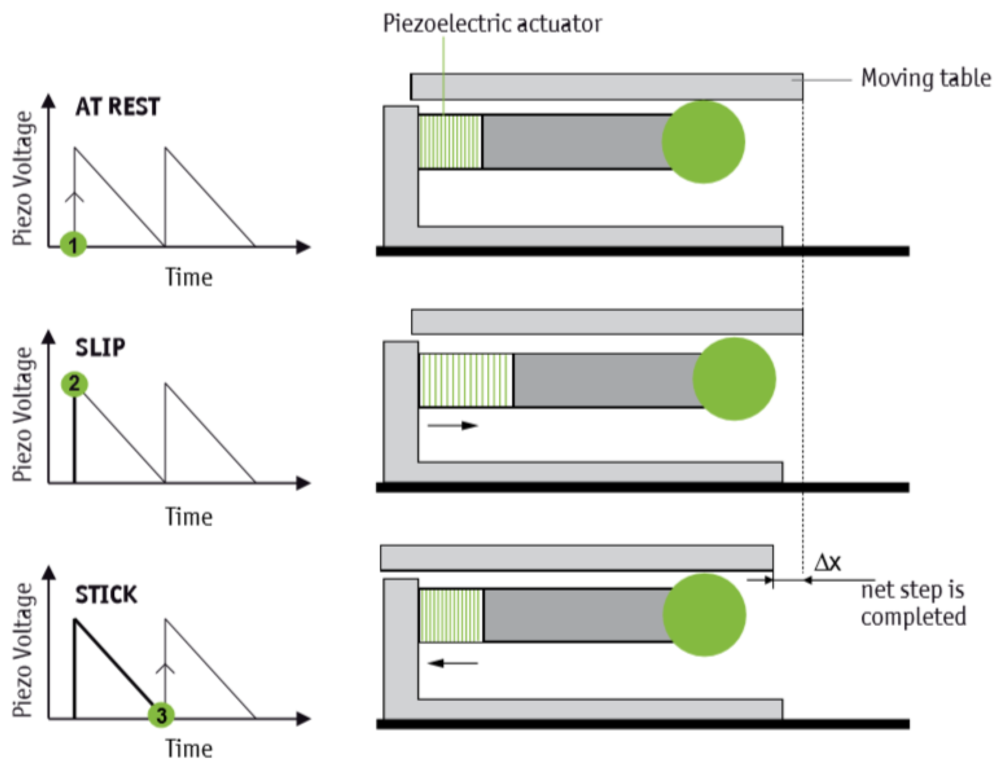

Figure 53. Stick-slip inside the nanopositioner (Attocube, 2021).

The piezoelectric starts expanding due to a voltage and moves the stage thanks to the frictional force. Once it gets to the maximum displacement, the voltage gets back to zero, but since frictional force is weaker when the object moves and thanks to the stage inertia, the piezoelectric piece gets back to its original position without changing the stage position. Figure 53 shows the voltage that is used with the piezoelectric.

The result on Figure 51 appears since the positioner uses a sawtooth function and because of the stick−slip effect. When the voltage cycle ends, and the piezoelectric contracts, part of the stage moves back, this is why in Figure 51 there is not a one to one relation.

Another important observation can be made if another zoom in is made; the result can be seen in Figure 54.

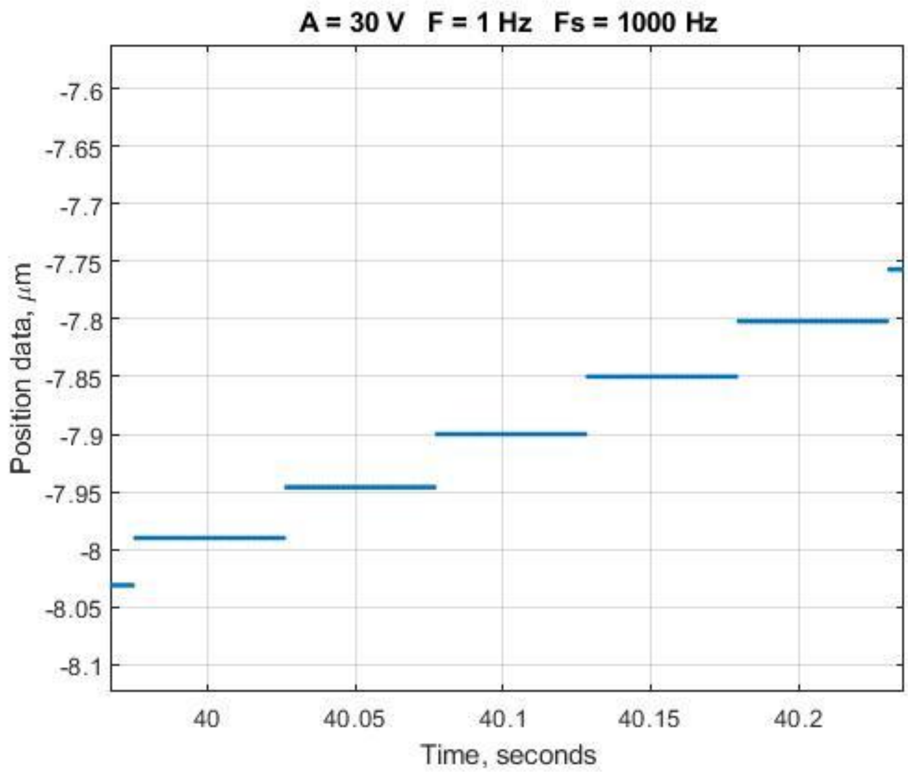

Figure 54. Second zoom in over the position vs. time plot.

Plotted data shows that for a range of time, the position stays constant. Since the stage moves continuously until it gets to the set position, there are constant values because of a delay with the position update. Every time the position command is called, the nanopositioner takes about 50 ms to update for the new position.

Preliminary measurements

The previous sections were important to understand in more detail the measuring system. In the following sections the preliminary measurements to characterize the measuring system will be explained.

Before doing a 2D scanning, it was necessary to do test measurements. These test consisted in using different experimental setups. These setups can be classified into three types: setup 1, setup 2, and modulation setup. The first two setups were primarily for testing, and the last one was used for testing and as the main setup for scanning. A sketch of setup 1 can be seen in Figure 55.

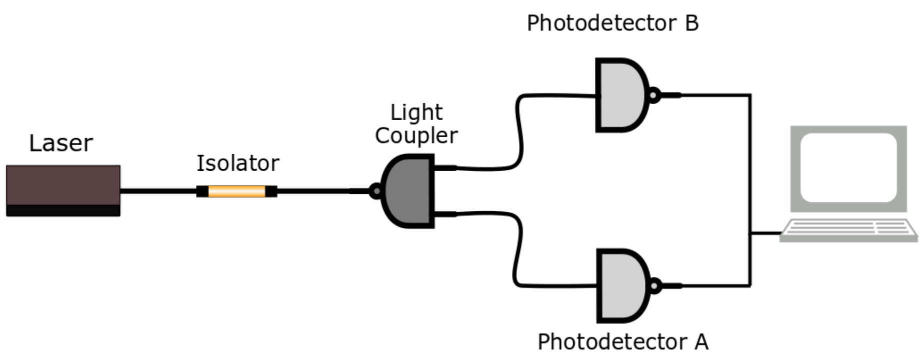

Figure 55. Setup 1.

This system was primarily to check that all the components worked correctly and check the light percentage that came out of the two outputs of the light coupler. This measurement was obtained by first measuring, with the oscilloscope, the voltage by connecting one of the photodetectors directly to the laser, then measuring the light that came out of each output of the light coupler and divided both values by the obtained voltage when connected directly. See Equation (94).

$$T = \frac{I_{out}}{I_{in}}. \tag{94}$$

The next one was setup 2; Figure 56 shows a diagram of the arrangement.

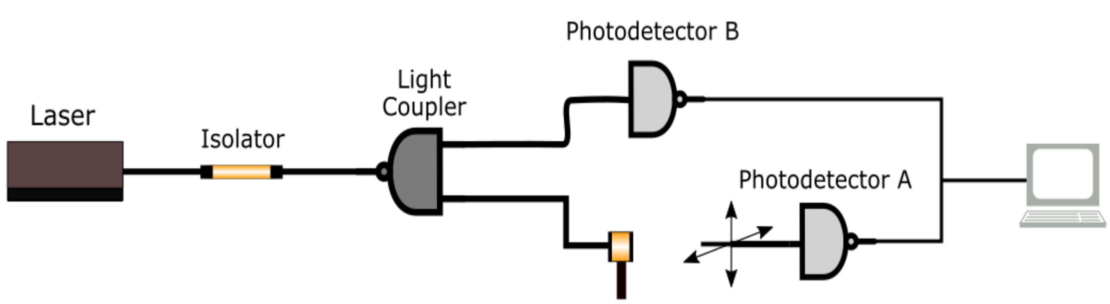

Figure 56. Setup 2.

Setup two was mainly for checking the light signal stability for a short and long term. This was done by doing measurements for a period of time in a fixed position. For this task, the measuring fiber was fixed where the maximum voltage appeared. This was done with different parameters for the oscilloscope and laser and with different *z* positions. Figure 57 shows the three different *z*-positions that were chosen.

Figure 57. Handle set in three different *Z* positions.

Since the distances in the handle were in inches, the position will be mention in inches. For clarity and to reduce the probability of human error, Z-distance will be represented in Matlab as an array of three components, just like in Equation (95).

$$[v_1, v_2, v_3]. \tag{95}$$

First is the number v_1 on the scale along Z-axis, which corresponds to 1/10 inch; second, number v_2 is written for clarity as a fraction of 1/10 inch as it represents fractional minor divisions under the numbers mentioned above; third and last value v_3 corresponds to the divisions on the rotating handle, in units of 0.001 inch. Using this notation, the Z-coordinate can be easily calculated in inches with Matlab. Equation (96) shows an example:

$$Dinch = sum([v_1, v_2, v_3] .* [0.1, 0.1, 0.001], 2); \tag{96}$$

or in millimeters as:

$$Dinch = sum([v_1, v_2, v_3] .* [0.1, 0.1, 0.001], 2) * 25.4; \quad (97)$$

Once the system was capable of measuring the light that came out of the sample fiber, the short-term stability was evaluated. This evaluation was made by calculating the mean value of each 8K signal block individually, in a fixed position, for both channels A and B. Figure 58 shows the results with the variability of each 8K signal block.

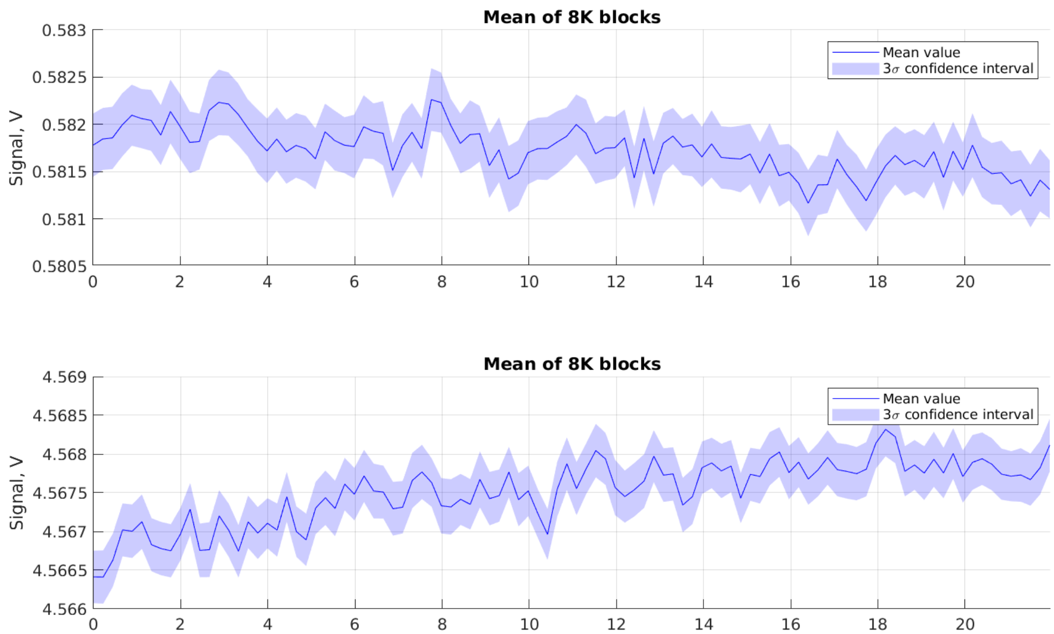

Figure 58. First is for channel A and the second for channel B.

Qualitatively these results show that the variation is approximately 7 mV. For a more detailed analysis the next experiment consisted in a long term stability test.

The long term stability evaluation was made by calculating the relative variation of the 8K block mean values over ~3hrs. The relative variation can be calculated as follows:

$$Mean\ relative\ variation = \frac{S_n - \overline{S_n}}{\overline{S_n}}, \quad (98)$$

where S_n is the raw signal and $\overline{S_n}$ is the mean of the signal. This test generated the following result.

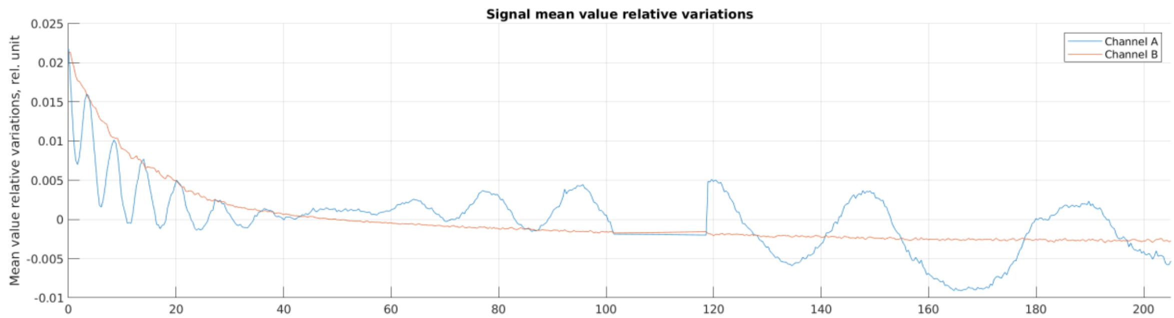

Figure 59. Long term stability for a non-modulated signal.

Figure 59 shows that the signal mean from channel B decays and starts converging to a value and channel A also decays but it shows an oscillating behavior which can be related to interference.

After these experiments the next setup was built. The third one was modulation setup, which is similar to setup 2, but the laser was connected to a function generator to modulate the signal, as shown in Figure 60.

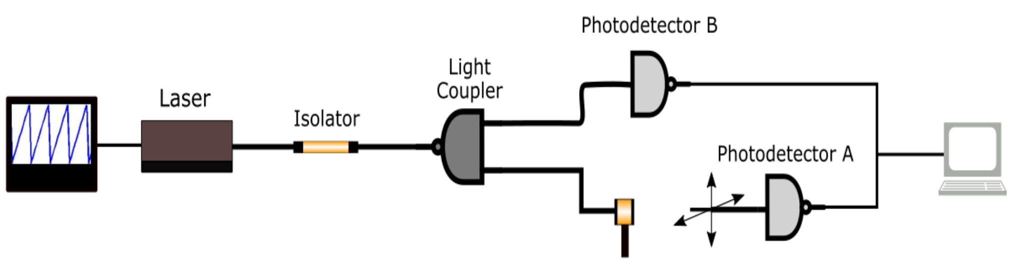

Figure 60. Modulation setup.

This setup was used for the 1D and 2D scans. With this system, the accuracy and stability were tested for the long and short term.

With this setup the stability evaluation was made with the RMS of the AC part of the signal and the transmission. The short-term stability evaluation of a modulated signal in a fixed point can be seen in Figure 61.

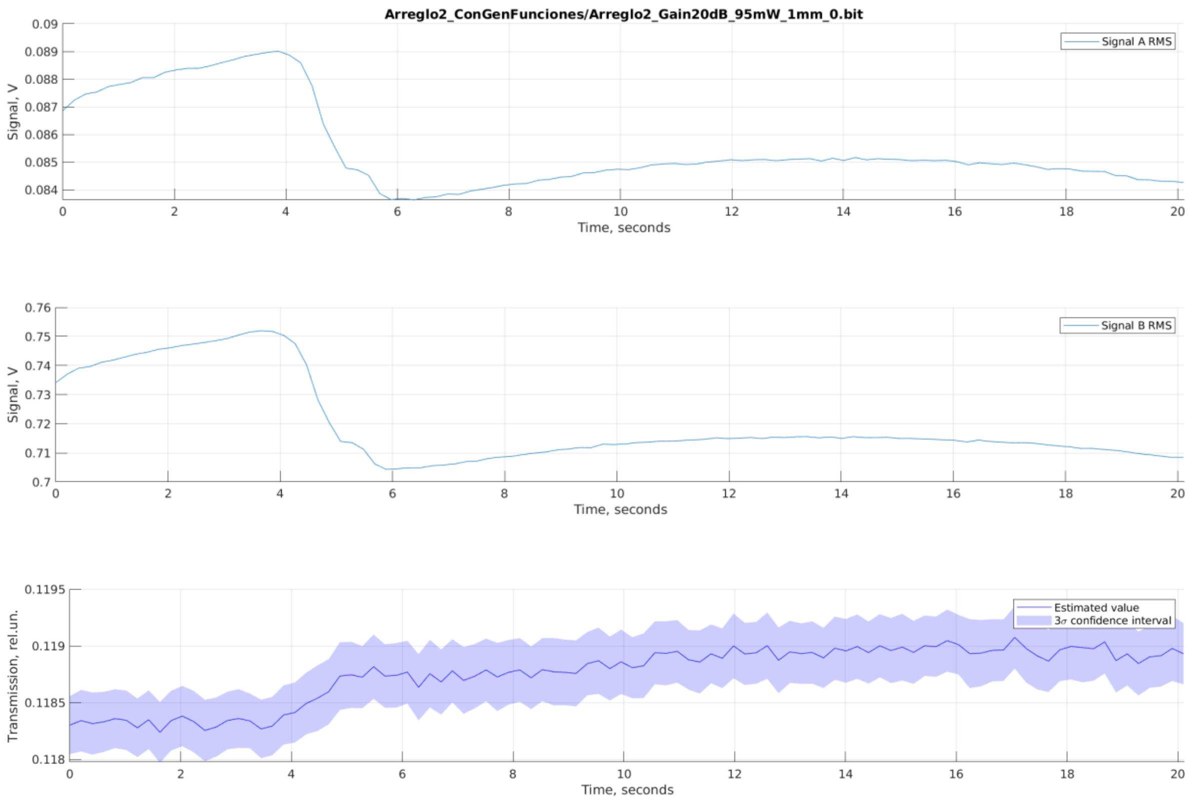

Figure 61. The first image is the RMS of channel A, the second is of channel B and the third is the transmission of the signal.

Figure 61 shows that for both channels A and B at the beginning a sharp change appears but then the signal starts stabilizing. The transmission shows a small change compared to the RMS. After this test a long term stability evaluation was made.

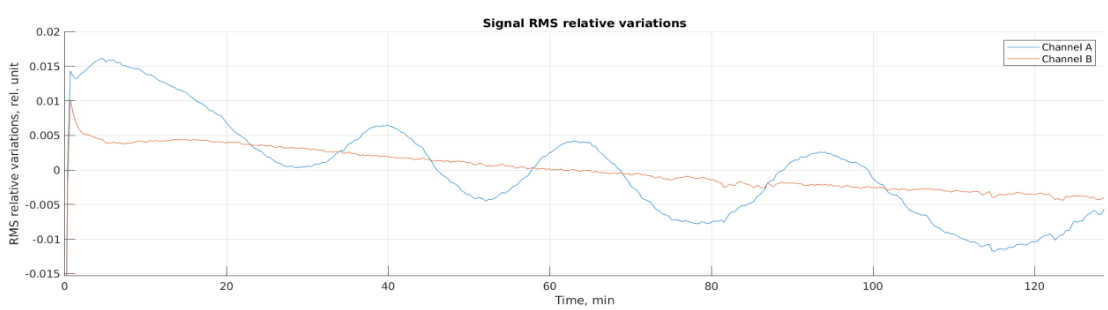

Figure 62. Modulated signal mean variation.

Comparing Figure 62 with the non-modulated result shows that the modulation of the signal does not affect the stability of the measurement and the oscillating behavior is still present.

Software

This last section will talk briefly about the software that was created. To control the whole system, it was necessary to create programs, this way it is possible to automate the whole measuring system. Two languages were used for programming: C++ and Matlab. The program made with C++ consisted in controlling the oscilloscope and the nanopositioner. Figure 63 shows a diagram of the behavior of the program.

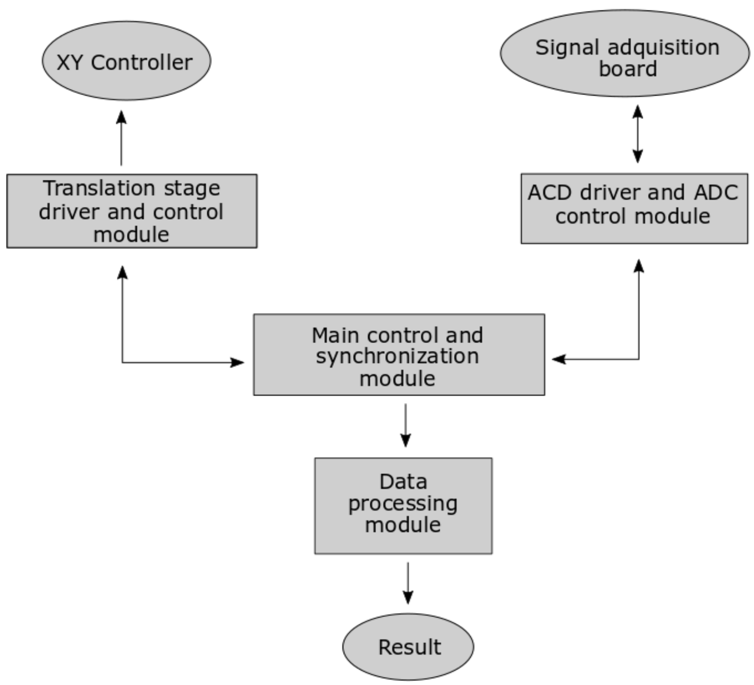

Figure 63. Diagram of the modules for the nanopositioner control and data acquisition.

The Matlab program was used to process the files that the C++ program generates. Matlab is used since it is a friendly language for calculations. These programs were constantly enhanced and adapted every time a problem appeared.